Studies of the proton-antiproton and $K^0_S K^0_S$ pair production from two-photon collisions at TRISTAN

1998年3月

浜崎　実

Studies of the proton-antiproton and $K^0_S K^0_S$ pair production 3

Studies of the proton-antiproton and $K^0_S K^0_S$ pair production from two-photon collisions at TRISTAN

1998年3月

浜崎 央

Studies of the proton-antiproton and $K^0_S K^0_S$ pair production from two-photon collisions at TRISTAN

Hiroshi Hamasaki

Institute of Applied Physics,
University of Tsukuba
Tsukuba, Ibaraki 305, Japan

March 1998

Abstract

The cross sections of the $\gamma\gamma \to p\bar{p}$ and $\gamma\gamma \to K^0_S K^0_S$ reactions were measured using two-photon processes at an $e^+ e^-$ collider, TRISTAN. The data used in this analysis were collected by the VENUS detector from 1991 to 1995 corresponding to an integrated luminosity of 331 pb^{-1}. Our study was limited to anti-tag events in two-photon processes, where scattered electrons and positrons were undetected, escaping with the beam pipe in small angle scattering.

The cross section for $\gamma\gamma \to p\bar{p}$ was measured in the two-photon center-of-mass energy ($W_{\gamma\gamma}$) range between 2.2 and 3.3 GeV. These events were selected by choosing events with two-prong final states and by identifying protons and antiprotons by time-of-flight counters. In total 311 events were selected as candidates of this reaction. The $W_{\gamma\gamma}$ dependence of the cross section obtained in a c.m. angular region of $|\cos\theta^*| < 0.6$ is in good agreement with the previous measurements and also with the theoretical prediction based on diquark model in the high $W_{\gamma\gamma}$ region.

The cross section for $\gamma\gamma \to K^0_S K^0_S$ was measured in the $W_{\gamma\gamma}$ range between 1.5 and 2.5 GeV. In total 11 events were observed as candidates of this reaction. The $W_{\gamma\gamma}$ dependence of the cross section was obtained in a c.m. angular region of $|\cos\theta^*| < 0.5$. No excess of events was observed in the $W_{\gamma\gamma} > 1.6$ GeV region, where new resonances and glueball candidate states are expected to be observed. Upper limits have been obtained for the $\gamma\gamma$-widths of the new resonance X(1800) and the glueball states $f_J(1710)$ and $f_J(2220)$.

Acknowledgements

This thesis is based upon the careful and detailed work of many people. I wish to thank all the members, past and present, of the VENUS collaboration and the TRISTAN accelerator group for their successful construction and operation of the experiment.

I would like to thank Prof. Y. Asano and Prof. S. Mori for their continuous encouragement and kind advice. And I would especially like to thank Dr. S. Uehara for his useful suggestions and discussions at KEK.

Finally I would like to thank my parents and brothers for their support and love. Without their help, my thesis could not have been completed.

Contents

List of Figures

List of Tables

Chapter 1

Introduction

A so-called "two-photon process" which is the photon-photon collision process is a very interesting process to test various theories and to search new particles. The great advantage of doing two-photon physics is that the initial state of the reaction is very clean. The analysis of a very short-lived particle is only possible by means of a reaction, in which the quanta which produce the state are identical to those which probe it. Such an analysis can be made with virtual photons in a photon-photon experiment. Therefore, in two-photon physics we can measure properties of arbitrarily short-lived particles.

Experimentally, a high energy photon-photon scattering reaction with large luminosities can be achieved by high energy electron-positron storage rings. That is, the two incoming beams (electron and positron) radiate (virtual) photons and these two photons react and produce the final state particles,

$$e^+e^- \rightarrow e^+e^-X \tag{1.1}$$

as shown in Fig 1.1. The TRISTAN, a high energy e^+e^- collider at the National Laboratory for High Energy Physics (KEK) in Japan, provides a very powerful source of (virtual) photons. The higher beam energy, $\sqrt{s} \sim 58$ GeV, enables studies for two-photon collisions at the high energy region.

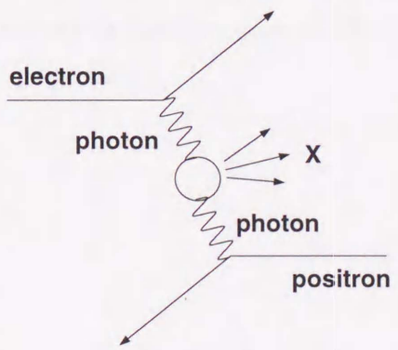

Figure 1.1: The two-photon process at e^+e^- colliders.

In this thesis, we have studied exclusive production of hadronic final states (proton antiproton pair and K^0_S pair) in two-photon processes. A great advantage of exclusive final state measurements is that in most cases, the exclusive reactions can be fully described by a small number of parameters in contrast to measurements of inclusive reactions.

In this chapter, we summarize the outline of the two-photon physics and describe the organization of this thesis.

1.1 Two-photon physics

1.1.1 Hadron production from two-photon collision

The investigation of two-photon production of hadronic final states provides the possibility of probing hadron dynamics with a simple, calculable initial state. Our main interest lies in the study of the coupling of the photon to hadrons, which in the framework of the quark model means the coupling to quarks as the constituents of hadrons. In the resonance region the quark model of bound quark-antiquark systems can be tested by measuring the two-photon resonance coupling. Enough information is now available to allow meaningful test of SU(3) symmetry and of models with multiquark or gluonium states. The investigation of the production of particles with high transverse momenta, jet production and scattering of highly virtual photons (deep-inelastic scattering), allows tests of quantum chromodynamics (QCD), the widely accepted theory of strong interactions.

In Maxwell's classical theory electromagnetic waves do not scatter off one another because of the linear superposition principle. However, quantum electrodynamics allows that interactions occur between the field quanta, the photons, by way of the quantum fluctuation of the vacuum, *i.e.* the creation and absorption of hadrons. It is known that there are three mechanisms which contribute to the hadron production in two-photon collisions as shown in Fig. 1.2. The direct (QPM) process (a) [1], where photons interact with quarks via point-like interactions, contributes to high-p_t production of quarks. At a low-p_t region, the VDM (vector meson dominance model) process (b) [2] is dominant where a hadronic component in a photon contributes interactions. At a medium-p_t region, the resolved-photon processes (c,d) [3] play an important role where partons inside photons interact point-like.

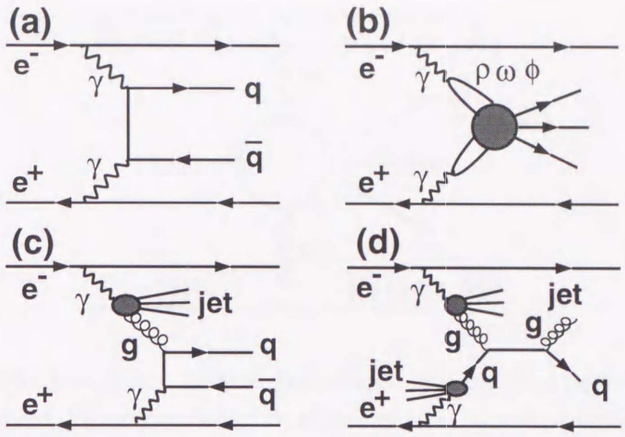

Figure 1.2: Feynman diagrams which contribute to the hadron production in two-photon processes: (a) direct (QPM) process, (b) VDM process, (c) one-resolved-photon process, (d) two-resolved-photon process.

1.1.2 Cross section

The cross section for two-photon production at an e^+e^- storage ring is written in such a form as to extract explicitly the contribution of the $\gamma\gamma \to X$ process and those of the $e^\pm \to e^\pm + \gamma$ vertices [4].

In terms of the $M^{\mu\nu}$ amplitude for the $\gamma\gamma \to X$ transition, the cross section for two-photon production can be expressed as follows (see notations in Fig 1.3):

$$\mathrm{d}\sigma_{ee\to eeX} = \frac{(4\pi\alpha)^2}{q_1^2 q_2^2} \rho_1^{\mu\mu'} \rho_2^{\nu\nu'} M^{*\mu'\nu'} M^{\mu\nu} \frac{(2\pi)^4 \delta(q_1+q_2-k)\mathrm{d}\Gamma}{4\{(p_1p_2)^2 - m_1^2 m_2^2\}^{1/2}} \frac{\mathrm{d}^3p_1' \mathrm{d}^3p_2'}{2E_1 2E_2 (2\pi)^6}. \tag{1.2}$$

Here $p_{1,2}$ are the momenta of the colliding electron and positron, $q_i = p_i - p_i'$ is the momentum of the virtual photon, $k = \sum_i k_i = q_1 + q_2$ is the total momentum of the produced system X with a mass $W_{\gamma\gamma} = \sqrt{k^2} = \sqrt{(q_1+q_2)^2}$ and the phase-space volume is $\mathrm{d}\Gamma = \prod_j \mathrm{d}^3k_j / 2\epsilon_j (2\pi)^3$. The matrix ρ_i has the meaning of an unnormalized density matrix for the virtual photon generated by the ith particle. For electron beams we have

$$\begin{aligned} \rho_i^{\mu\nu} &= -\frac{1}{q_i^2} \sum_{\text{spins}} \bar{u}(p_i')\gamma^\mu u(p_i) \bar{u}(p_i)\gamma^\nu u(p_i') \\ &= -\frac{1}{2q_i^2} \mathrm{Tr}[\gamma^\mu (\not{p}_i + m_e)\gamma^\nu (\not{p}_i' + m_e)] \\ &= q_i^2 g_i^{\mu\nu} - 2(p_i^\mu p_i'^\nu + p_i'^\mu p_i^\nu), \end{aligned} \tag{1.3}$$

where u is the Dirac spinors for the electron, $g^{\mu\nu}$ is the metric tensor defined according to the convention of Bjorken and Drell, and m_e is the electron mass.

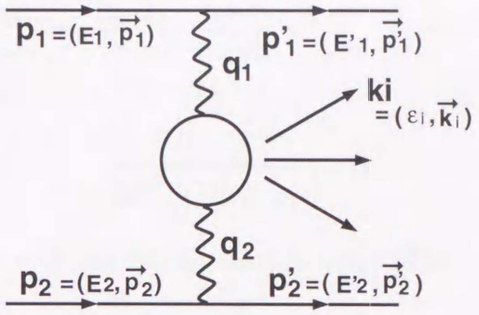

Figure 1.3: The two-photon particle production. The colliding particles with momenta p_1 and p_2 change these momenta to p_1' and p_2' while interacting, and emit virtual photons with momenta $q_i = p_i - p_i'$. These colliding photons produce the finite particle system X, whose momentum is $k = \sum_j k_j = q_1 + q_2$ and effective mass is $W_{\gamma\gamma} = \sqrt{k^2}$.

1.1.3 Helicity structure of the two-photon cross section

The photons radiated from the incoming leptons are well expressed by states of transverse (T) or longitudinal polarization (L). The cross section therefore is expressed by the cross section of $\gamma\gamma \to X$ ($\sigma_{\mathrm{TT}}, \sigma_{\mathrm{TL}}, \sigma_{\mathrm{LT}}, \sigma_{\mathrm{LL}}$) and interference terms (τ_{TT}, τ_{TL}). The polarization indices refer to the first and second photons, respectively. Disentangling the leptonic part ($e \to e'\gamma$) from $\gamma\gamma \to X$ and summing over μ, ν, μ', ν', the equation (1.2) becomes

$$\begin{aligned} \mathrm{d}\sigma_{ee\to eeX} &= \frac{\alpha^2}{16\pi^4 q_1^2 q_2^2}\left[\frac{(q_1q_2)^2 - q_1^2q_2^2}{(p_1p_2)^2 - m_1^2m_2^2}\right]^{1/2} \\ &\quad [4\rho_1^{++}\rho_2^{++}\sigma_{\mathrm{TT}} + 2\rho_1^{++}\rho_2^{00}\sigma_{\mathrm{TL}} + 2\rho_1^{00}\rho_2^{++}\sigma_{\mathrm{LT}} + \rho_1^{00}\rho_2^{00}\sigma_{\mathrm{LL}} \\ &\quad +2|\rho_1^{+-}\rho_2^{+-}|\tau_{\mathrm{TT}}\cos 2\tilde{\phi} - 8|\rho_1^{+0}\rho_2^{+0}|\tau_{\mathrm{TL}}\cos\tilde{\phi}] \\ &\quad \frac{\mathrm{d}^3p_1'\mathrm{d}^3p_2'}{E_1E_2} \end{aligned} \tag{1.4}$$

for the unpolarized beam. Hear $\tilde{\phi}$ is the angle between the scattering planes of the colliding particles in the photon center-of-momentum system. All these quantities are expressed in terms of the measurable momenta p_i and p_i' only and to that extent are completely known.

The quantities ρ_i^{ab} are defined using the density matrices of virtual photons in the $\gamma\gamma$ helicity basis by the relation

$$\rho_i^{ab} = (-1)^{a+b} e_i^{\mu}(a)\rho_i^{\mu\nu}e_i^{*\nu}(b), \tag{1.5}$$

where $e^{\mu}(a)$ is the polarization four vector of a photon with helicity a ($a = 0$ refers to the scalar polarization and $a = \pm 1$ refers to the transverse polarization). For e^+e^- collisions we obtain:

$$2\rho_1^{++} = 2\rho_1^{--} = \frac{(2p_1q_2 - q_1q_2)^2}{(q_1q_2)^2 - q_1^2q_2^2} + 1 + \frac{4m_e^2}{q_1^2}, \tag{1.6}$$

$$\rho_2^{++} = \rho_1^{++}(1 \leftrightarrow 2), \tag{1.7}$$

$$\rho_1^{00} = \frac{(2p_1q_2 - q_1q_2)^2}{(q_1q_2)^2 - q_1^2q_2^2} - 1, \tag{1.8}$$

$$\rho_2^{00} = \rho_1^{00}(1 \leftrightarrow 2), \tag{1.9}$$

$$|\rho_i^{+-}| = \rho_i^{++} - 1, \tag{1.10}$$

$$|\rho_i^{+0}| = \sqrt{(\rho_i^{00} + 1)|\rho_i^{+-}|}. \tag{1.11}$$

The cross section for $\gamma\gamma \to X$ can be expressed in terms of helicity tensors $W_{a'b',ab}$ as

$$\sigma_{\rm TT}(W_{\gamma\gamma}, q_1^2, q_2^2) = \frac{1}{4\sqrt{(q_1q_2)^2 - q_1^2q_2^2}}(W_{++,++} + W_{+-,+-}), \tag{1.12}$$

$$\sigma_{\rm LL}(W_{\gamma\gamma}, q_1^2, q_2^2) = \frac{1}{2\sqrt{(q_1q_2)^2 - q_1^2q_2^2}}(W_{00,00}), \tag{1.13}$$

$$\sigma_{\rm TL}(W_{\gamma\gamma}, q_1^2, q_2^2) = \frac{1}{2\sqrt{(q_1q_2)^2 - q_1^2q_2^2}}(W_{+0,+0}), \tag{1.14}$$

$$\sigma_{\rm LT}(W_{\gamma\gamma}, q_1^2, q_2^2) = \frac{1}{2\sqrt{(q_1q_2)^2 - q_1^2q_2^2}}(W_{0+,0+}), \tag{1.15}$$

$$\tau_{\rm TT}(W_{\gamma\gamma}, q_1^2, q_2^2) = \frac{1}{2\sqrt{(q_1q_2)^2 - q_1^2q_2^2}}(W_{++,--}), \tag{1.16}$$

$$\tau_{\rm TL}(W_{\gamma\gamma}, q_1^2, q_2^2) = \frac{1}{4\sqrt{(q_1q_2)^2 - q_1^2q_2^2}}(W_{++,00} + W_{0+,-0}). \tag{1.17}$$

All these quantities depend on the two-photon invariant mass, $W_{\gamma\gamma}$, and the squared virtual photon momenta, q_1^2 and q_2^2, only.

The helicity tensors are essentially cross sections with all flux terms taken out

$$W_{a'b',ab} = \frac{1}{2}\int M^*_{a'b'}M_{ab} \cdot (2\pi)^4\delta(q_1 + q_2 - \sum_i k_i)\prod_i \frac{{\rm d}^3k_i}{(2\pi)^3 2\epsilon_i}. \tag{1.18}$$

The $\gamma\gamma \to X$ helicity amplitudes M_{ab} are defined by the relation

$$M_{ab} = F(q_1^2, q_2^2)M^{\mu\nu}e_1^\mu(a)e_2^\nu(b), \tag{1.19}$$

where the form factor $F(q_1^2, q_2^2)$ describes how the interaction of virtual photons differs from that of real photons, and must be determined experimentally. For events with large Q^2, the cross section is usually suppressed, *i.e.* $F < 1$, and in the limit $q_1^2, q_2^2 \to 0$, $F \to 1$.

Approximation

In case both photons are nearly on the mass shell, $q_i^2 \to 0$, the cross section of scalar photon scattering vanishes and $\sigma_{\rm TT}$ and $\tau_{\rm TT}$ are transformed into the corresponding quantities for real photoprocesses. In particular, at $q_i^2 = 0$, $\sigma_{\rm TT}$ coincides with the cross section for real non-polarized two-photon collision, $\sigma_{\gamma\gamma\to X}$. As a result, at $q_i^2 \to 0$, we have

$$\sigma_{\rm TT}(W_{\gamma\gamma}, q_1^2, q_2^2) \to \sigma_{\gamma\gamma\to X}(W_{\gamma\gamma}), \tag{1.20}$$

$$\tau_{\rm TT}(W_{\gamma\gamma}, q_1^2, q_2^2) \to \tau_{\gamma\gamma\to X}(W_{\gamma\gamma}). \tag{1.21}$$

Thus the cross section has a simple form:

$$\mathrm{d}\sigma_{ee\to eeX} = \left(\frac{\alpha}{4\pi^2}\right)^2 \frac{W_{\gamma\gamma}}{sq_1^2q_2^2}[4\rho_1^{++}\rho_2^{++}\sigma_{\gamma\gamma\to X} + 2|\rho_1^{+-}\rho_2^{+-}|\tau_{\gamma\gamma\to X}\cos\tilde{\phi}]\frac{\mathrm{d}^3p_1'\mathrm{d}^3p_2'}{E_1E_2}. \tag{1.22}$$

If we introduce the photon spectrum radiated by the lepton beams, $f_{\gamma/e}(z_i = E_{\gamma i}/E_{\mathrm{beam}}, Q_i^2 = -q_i^2)$, and their polarizations, $\xi_i = |\rho^{+-}|/\rho_i^{++}$, then the cross section is rewritten in the form

$$\mathrm{d}\sigma_{ee\to eeX} = (\sigma_{\gamma\gamma\to X} + \frac{1}{2}\xi_1\xi_2\tau_{\gamma\gamma\to X}\cos 2\phi)f_{\gamma/e}(z_1,Q_1^2)f_{\gamma/e}(z_2,Q_2^2)\mathrm{d}z_1\mathrm{d}z_2\frac{\mathrm{d}\phi}{2\pi}, \tag{1.23}$$

where the photon spectrum (or the number of equivalent photons) $f_{\gamma/e}$ is

$$f_{\gamma/e}(z_i,Q_i^2) = \frac{\alpha}{2\pi}\rho_i^{++}z_i\frac{\mathrm{d}Q_i^2}{Q_i^2}. \tag{1.24}$$

After proper integration the interference term $\tau_{\gamma\gamma}$ vanishes and we obtain

$$\mathrm{d}\sigma_{ee\to eeX} = \sigma_{\gamma\gamma\to X}(W_{\gamma\gamma})f_{\gamma/e}(z_1,Q_1^2)f_{\gamma/e}(z_2,Q_2^2)\mathrm{d}z_1\mathrm{d}z_2. \tag{1.25}$$

1.1.4 Conservation laws in $\gamma\gamma \to X$

The two-photon vertex is subject to a number of conservation laws, in particular "charge conjugation invariance", "gauge invariance", "Lorenz invariance (which includes conservation of angular momentum)", "Bose statistics" and "conservation of parity".

From the consequence of charge conjugation invariance, only states with positive charge conjugation ($C = +1$) can be produced in two-photon processes since two photons have even C parity. The helicity matrix element M_{ab} for a state of a specific spin parity J^P particle produced in collisions of photons is restricted by the consequence of these conservation laws. A detailed analysis is given in a review by Poppe [5]; these conservation laws are known as Yang's theorem [6]. In the case of real photons ($q_1^2 = q_2^2 = 0$), only a small number of amplitudes remain nonzero

$$M_{\pm\pm}(J^P = 0^\pm, 2^\pm, 4^\pm, ...) \neq 0 \tag{1.26}$$

$$M_{\pm\mp}(J^P = 2^+, 3^+, 4^+, ...) \neq 0, \tag{1.27}$$

and all others vanish.

1.2 Proton-antiproton pair production in two-photon collisions

Since baryons are known to be composites of partons, *i.e.*, quarks and gluons, their production from the vacuum cannot be straightforward. The mechanism of the production is not well understood, despite that they are the fundamental elements forming the matter of the universe.

The pair production of a proton and an antiproton in two photon collisions,

$$\gamma\gamma \to p\bar{p}, \tag{1.28}$$

is one of the simplest processes suitable for investigating this problem. This reaction has been measured by many experiments at high-energy e^+e^- colliders [7–11], utilizing the two-photon process, *i.e.*, $e^+e^- \to e^+e^-p\bar{p}$, where the $p\bar{p}$ pair is produced from the collision of two nearly real photons emitted from incoming e^+ and e^-. The obtained experimental results, such as the production cross section, are consistent with each other among the experiments as shown in Fig. 1.4. However, we still have large ambiguity due to limited statistics, especially in a high $\gamma\gamma$ center-of-mass energy region.

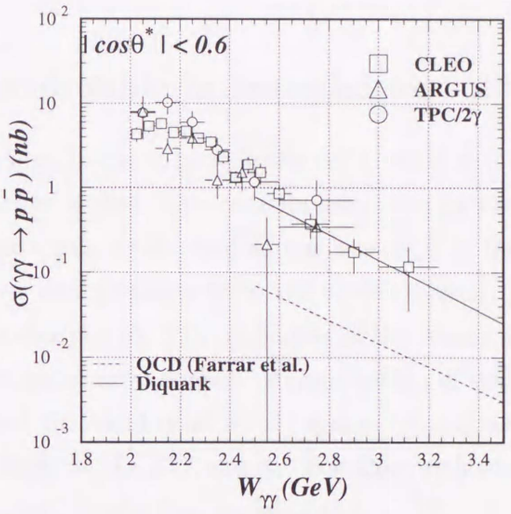

Figure 1.4: Measurements of the cross section for $\gamma\gamma \to p\bar{p}$ as a function of $W_{\gamma\gamma}$ by CLEO [11], ARGUS [10] and TPC/2γ [9] collaborations. The curves are the predictions of QCD (dashed) and the diquark model (solid). All results are restricted to the range of $|\cos\theta^*| < 0.6$.

At low energies near threshold, reaction (1.28) must be complicated due to strong hadronic final-state interactions. The reaction is expected to show up its fundamental mechanism as the two-photon center-of-mass energy ($W_{\gamma\gamma}$) becomes larger, where a certain perturbative picture becomes applicable with helps from some customary phenomenology.

The cross section of reaction (1.28) has been estimated theoretically [12–14] on the basis of QCD, in the theoretical framework developed by Brodsky and Lepage [15]. The estimation depends on the model of the proton wave function. Among various ways of modeling, one of the most successful is the approach by Chernyak and Zhitnitsky [16] based on the QCD sum rule. Calculations based on their wave functions give reasonable estimates for some physical processes, such as $J/\psi \to p\bar{p}$ and magnetic form factors of the nucleons. However, the calculation for reaction (1.28) incorporating the same wave function [12] gives cross sections remarkably smaller than the experimental results, by one order of magnitude even at high energies around $W_{\gamma\gamma} = 3.0$ GeV.

Recently, a new calculation based on a diquark model has been proposed [17]. The model was found to reasonably reproduce the recent result from the CLEO group [11] in the high $W_{\gamma\gamma}$ region. Although the preference of the diquark model is apparent from the CLEO result, repeated measurements are necessary since the statistics of the experimental data is quite limited at high energies.

In this thesis, we present experimental results concerning the $\gamma\gamma \to p\bar{p}$ reaction in a $W_{\gamma\gamma}$ range between 2.2 and 3.3 GeV. Although the integrated luminosity is about one forth of that of the CLEO measurement [11], the larger e^+e^- c.m. energies enable us to obtain comparable statistics in the high $W_{\gamma\gamma}$ region.

1.3 $K^0_S K^0_S$ pair production in two-photon collisions

The hadron resonance production in two-photon collisions is well suited to explore the structure of hadrons and properties of their basic constituents, since photons are not directly involved in strong interactions. Kaon pair production at low masses (1-2 GeV) in two-photon interactions is expected to contain contributions from the tensor mesons ($(J)^{PC} = (2^{++})$: $f_2(1270)$, $a_2(1320)$ and $f_2'(1525)$ and continuum. The properties of the tensor mesons have been gradually determined due to many experimental studies. Measurements of tensor meson radiative widths ($\Gamma_{\gamma\gamma}$) are important to test the validity of SU(3) symmetry and are often used to determine the octet singlet mixing angle in the 2^{++} nonet. Together with measurements of the helicity structure they can test explicit production models (see e.g. [5]).

Two-photon decay widths of a resonance can be directly measured by observing its formation in two-photon collision reactions using the Breit-Wigner function:

$$\sigma_{\rm TT} = \sigma_{\gamma\gamma\to R} = 8\pi(2J+1)\frac{\Gamma_{\gamma\gamma}(R)\Gamma_{\rm tot}}{(M_R^2 - W^2)^2 + M_R^2\Gamma_{\rm tot}^2} \tag{1.29}$$

where J denotes the spin of the resonance, M_R its resonance mass, and $\Gamma_{\rm tot}$ and $\Gamma_{\gamma\gamma}(R)$ its total and two-photon decay widths, respectively. Measurements of two-photon decay widths for the tensor mesons are summarized in Table 1.1.

According to requirements of the assumptions of approximate SU(3) symmetry and OZI suppression [23], $f_2(1270)$ and $a_2(1320)$ are expected to interfere constructively in the charged kaon final state (K^+K^-) but destructively in the neutral kaon final state ($K^0\bar{K^0}$). Therefore, among the states of the tensor meson nonet, only $f_2'(1525)$ is observable in the $K^0_S K^0_S$ final state as has been verified experimentally.

L3 collaboration reported an enhancement in $K^0_S K^0_S$ production from two-photon collisions around 1800 MeV [27] as shown in Fig. 1.5. Such a signature has neither been so far observed in $K^0_S K^0_S$ [24–26] nor in K^+K^- [28,29] channels in other experiments. Cross sections for these reactions measured by several groups are shown in Fig. 1.6 and Fig. 1.7. The resonances of the tensor mesons are clearly shown but no significant enhancement in the high-$W_{\gamma\gamma}$ region (> 1.6

Resonance	$\Gamma_{\gamma\gamma}$ (KeV)	Observed mode	Experiment (year)
$f_2(1270)$	2.8±0.4		World Average [18]
	2.92±0.05±0.31	$e^+e^- \to e^+e^-\pi^+\pi^-$	VENUS (1995) [19]
	$2.58\pm0.13^{+0.36}_{-0.27}$	$e^+e^- \to e^+e^-\pi^+\pi^-$	CELLO (1992) [20]
$a_2(1320)$	1.01± 0.08		World Average
	0.96±0.03±0.13	$e^+e^- \to e^+e^-\pi^+\pi^-\pi^0$	ARGUS (1997) [21]
	1.26±0.26±0.18	$e^+e^- \to e^+e^-\pi^+\pi^-\pi^0$	MD1 (1990) [22]
Resonance	$\Gamma_{\gamma\gamma} \times \mathrm{Br}(R \to K\bar{K})$ (KeV)	Observed mode	Experiment
$f_2'(1525)$	0.086±0.012		World Average
	0.093±0.018±0.022	$e^+e^- \to e^+e^- K^0_S K^0_S$	L3 (1995) [27]
	0.067±0.008±0.015	$e^+e^- \to e^+e^- K^+K^-$	ARGUS (1990) [29]

Table 1.1: World average and measurements of $\Gamma_{\gamma\gamma}$ of the tensor mesons.

GeV) is observed in these figures. Therefore, it is a purpose of this study to confirm the existence of this resonance.

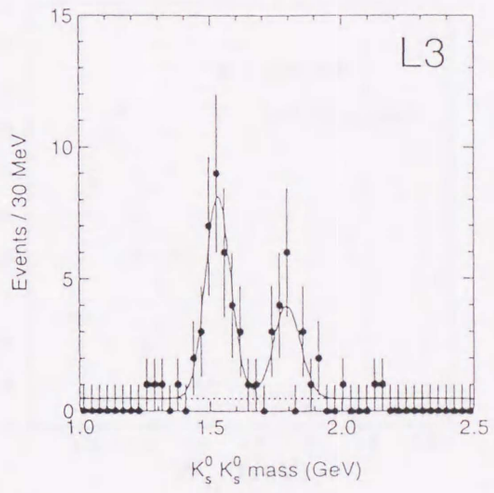

Figure 1.5: The $K^0_S K^0_S$ invariant mass spectrum measured by L3 collaboration [27]. The solid line corresponds to the maximum likelihood fit. The background is fitted by a constant (dashed line) and the two peaks by Gaussian curves.

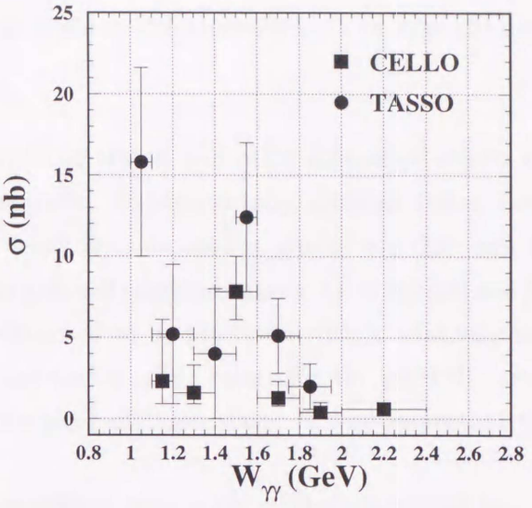

Figure 1.6: Measurements of the cross section for $\gamma\gamma \to K^0\bar{K}^0$ as a function of $W_{\gamma\gamma}$ by TASSO [24] and CELLO [26] collaborations.

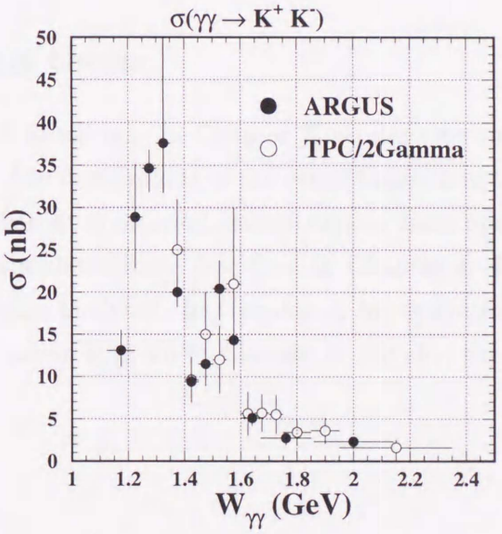

Figure 1.7: Measurements of the cross section for $\gamma\gamma \to K^+K^-$ by ARGUS [29] and TPC/2γ [28] collaborations.

The measured two-photon widths are also used to search for exotic (non-$q\bar{q}$) states. The existence of gluon self coupling in QCD suggests that gluonia (or glueballs), which are bound states consisting only of gluons (two or more), might exist [30]. Some signatures naively expected for glueballs are

1. no place in $q\bar{q}$ nonets,

2. flavor-singlet couplings,

3. enhanced production in gluon-rich channels such as $J/\psi(1S)$ decay, and

4. reduced $\gamma\gamma$ coupling.

However, mixing effects with $q\bar{q}$ states, and other dynamical effects such as form factors, may obscure these simple signatures. Experimentally, glueball states have been searched through reactions, radiative J/ψ decay [31], pp central production [32], and diffractive hadron-hadron scattering [33]. Among the glueball candidate states $f_J(1710)$ [34] and $f_J(2220)$ [35] are currently under investigation and expected to be produced with a relatively large $K\bar{K}$ branching ratio. The calculations of the expected $\Gamma_{\gamma\gamma}(R)$ values for the glueball candidates are made [36]. A measurement of the $\gamma\gamma$ coupling of these states is very important for an assessment of their gluonic nature.

In this thesis we present the experimental results concerning the $e^+e^- \to e^+e^- K^0_S K^0_S$ reaction, where the invariant mass range for $K^0_S K^0_S$ is between 1.5 and 2.5 GeV. Due to a very small detection efficiency it is very difficult to detect the tensor meson resonances in the small-$W_{\gamma\gamma}$ region (< 1.6 GeV), but the reasonably high efficiency in the high-$W_{\gamma\gamma}$ region provides us with the possibility to observe new evidences of resonances which are not well established.

1.4 Outline of this thesis

This thesis is organized as follows: In Chapter 2, we describe the e^+e^- collider TRISTAN and the VENUS detector. The descriptions of the event trigger and the data acquisition system are also contained. The procedure of event reconstruction from obtained data is described in Chapter 3. Monte Carlo simulations are described in Chapter 4. In Chapters 5, 6 and 7 we explain our procedure of data analyses. In Chapter 8, we derive results of the measurements of the cross sections. Discussion is given in Chapter 9. Finally, the conclusion is presented in Chapter 10.

Chapter 2

Experimental Apparatus

The data used in the present analysis were collected by a general purpose magnetic spectrometer VENUS [1] at an electron-positron collider, TRISTAN [2], which was located at National Laboratory for High Energy Physics (KEK) [3] in Tsukuba, Japan. Figure 2.1 shows a layout of TRISTAN. It consists of three parts; injectors into a linear accelerator (LINAC), an accumulation ring (AR) and a main ring (MR). The VENUS detector is located at one of the four interaction points, FUJI experimental hall on MR. A brief introduction to TRISTAN and the VENUS detector is given below.

2.1 TRISTAN

TRISTAN started operation in November 1986. Then great efforts had been put in raising the beam energy of TRISTAN as much as possible. To achieve this goal, more than thirty cavities including those of superconducting type were added in the TRISTAN ring until the summer of 1989. Finally, the maximum center-of-mass energy of 64 GeV was achieved in December 1989. This first period was called TRISTAN phase-I.

In February 1990, TRISTAN phase-II operation was started. In the second period, the emphasis of operation was set on obtaining as high luminosity as possible. A pair of superconducting quadrupole magnets (QCSs) were installed at each collision point. The center-of-mass energy was fixed at 58 GeV to obtain the maximum luminosity. As a result, a peak luminosity of 1.02 pb^{-1}/day was achieved on 23 November 1991. The total integrated luminosity from November 1986 to May 1995 was about 400 pb^{-1}.

[1] VErsatile National Laboratory and Universities Spectrometer

[2] Transposable Ring Intersecting STorage Accelerator in Nippon

[3] From April 1, 1997, High Energy Accelerator Research Organization (KEK) was newly established. The new organization is restructured of three research institutes, National Laboratory for High Energy Physics (KEK), Institutes of Nuclear Study (INS), Univ. of Tokyo and Meson Science Laboratory, Faculty of Science, Univ. of Tokyo.

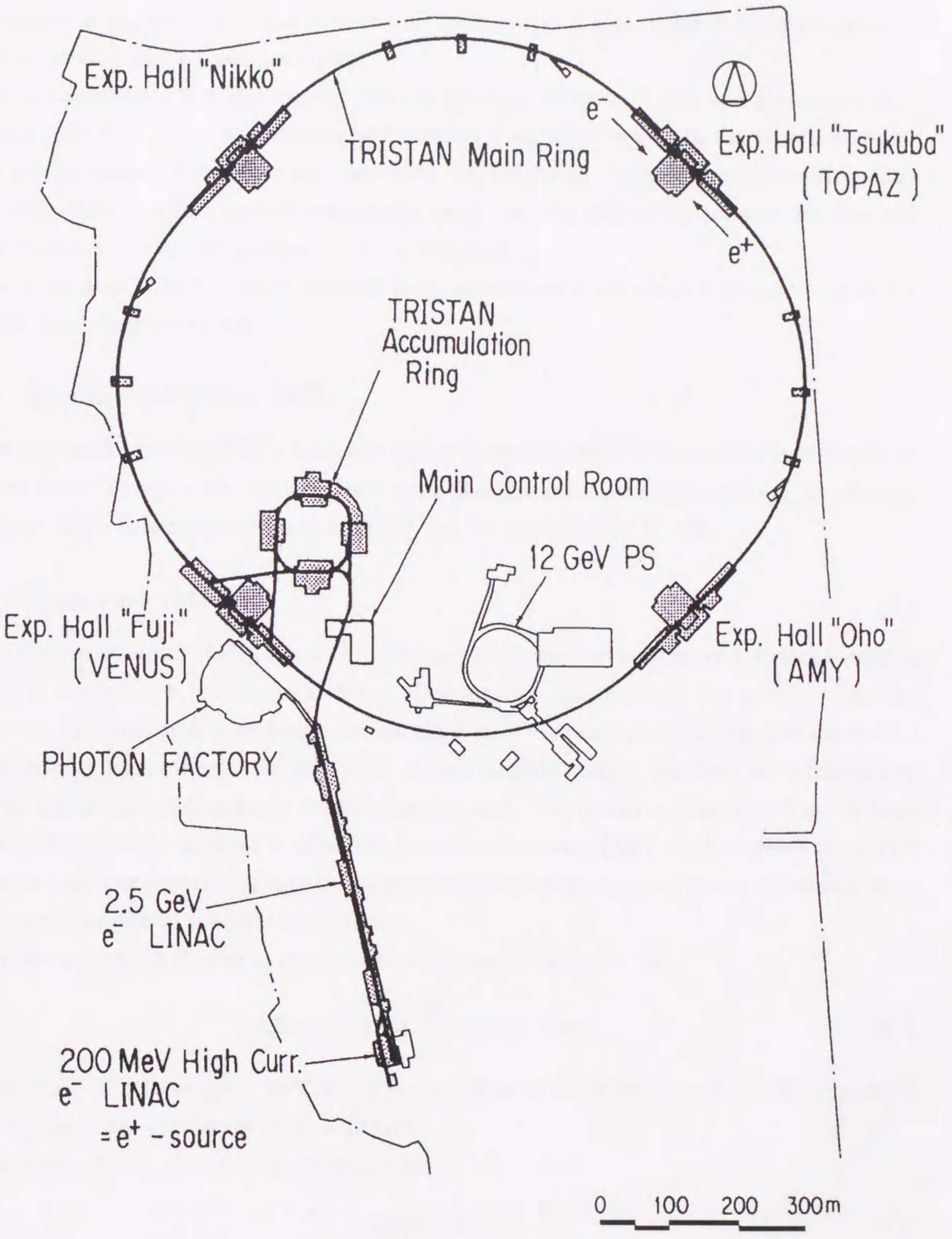

Figure 2.1: Layout of TRISTAN.

2.1.1 Injectors (LINAC)

Injectors consist of two parts; a positron generator and a main linear accelerator (LINAC). Furthermore, a positron generator consists of three parts; a high current pre-accelerator, a conversion section and a post-accelerator.

The pre-accelerator is a high current electron linear accelerator of 10A and accelerates electrons up to 200 MeV. Then the electron beam strikes a tantalum target. In the target, electrons induce electro-magnetic showers; *i.e.* positrons are generated through electron-positron pair production. Positrons in a certain momentum range are selected with a solenoid magnet and then accelerated by the post-accelerator up to 250 MeV.

The main linac, LINAC, which is 400m long, accelerates electrons and positrons up to 2.5 GeV and then transfers to AR.

2.1.2 Accumulation ring (AR)

The accumulation ring (AR) is a booster whose circumference is 377m and stores electrons or positrons from LINAC to the beam current more than 10 mA. After accumulation, an electron or positron beam is accelerated up to 8.0 GeV and then transferred to MR.

2.1.3 Main ring (MR)

The main accelerator (MR), has a circumference of 3018m and consists of 4 straight sections of 193m in length each, and 4 arc sections. Two electron bunches and two positron bunches circulate in opposite directions (electrons circulate clockwise and positrons counter-clockwise) and collide with each other at the mid-point of each straight section. So there are 4 interaction points at which the colliding beam detectors are located. The beams collide every 5 μs. A large portion of the straight sections is allocated for radio frequency (RF) cavities which accelerate the beams from the injection energy to the required collision energy and then compensate for a large energy loss due to synchrotron radiation.

The energy loss (ΔE) due to synchrotron radiation is expressed as

$$\Delta E \simeq 0.0885 \times \frac{E^4}{\rho} \quad (\mathrm{MeV/turn}), \tag{2.1}$$

where E is the beam energy in GeV and ρ is the radius of curvature in meter. The amount of radiation loss is 254 MeV/turn at $E = 29$ GeV.

The beam energy spread σ_E is expressed as

$$\frac{\sigma_E}{E} = 0.857 \times 10^{-3} \times \frac{E}{\rho} \tag{2.2}$$

which amounts to 49 MeV at $E = 29$ GeV. The energy spread varies according to the frequency shift (Δf_{RF}) applied to the accelerator by the RF cavities. Δf_{RF} is stable around 3 kHz during the runs of the present experiment.

The beam has approximately Gaussian shapes with the effective root mean square width of about 300 μm in the horizontal direction, 10 μm in the vertical direction, and 2 cm in the beam direction at the intersection points in the TRISTAN Phase-II operation. A typical lifetime of the beam is $3 \sim 4$ hours during a physics run. The parameters of MR are listed in Table 2.1.

TRISTAN MR parameters	
Circumference	3018 m
Beam radius (ρ)	246.5 m
Injection beam energy	8.0 GeV
Max. beam energy	32.0 GeV
Revolution frequency (f_{rev})	99.3 MHz
Beam current per bunch	$\sim$ 4 mA
Number of bunches (N_b)	4 ($2e^- + 2e^+$)
Beam size at collision point ($\sigma_x^*/\sigma_y^*/\sigma_z^*$)	300 μm / 20 μm / 1cm
Max. luminosity	1.6×10^{31} cm^{-2} sec^{-1}
Max. integrated luminosity per day	1.02 pb^{-1}
Beam life	$3 \sim 4$ h

Table 2.1: Parameters of TRISTAN Main Ring.

The luminosity is one of the most important parameters in the colliding beam experiments. The event rate, $\mathrm{d}N/\mathrm{d}t$, for a reaction having a total cross-section σ, is related to the luminosity L of the machine by

$$\frac{\mathrm{d}N}{\mathrm{d}t} = \sigma \cdot L. \tag{2.3}$$

For an e^+e^- collider, L is often expressed as follows

$$L = \frac{n_{e^+} n_{e^-}}{4\pi\sigma_x^*\sigma_y^*} \cdot f_{rev} \tag{2.4}$$

$$= \frac{I_{e^+} I_{e^-}}{4\pi e^2 \sigma_x^* \sigma_y^* f_{rev}}. \tag{2.5}$$

The beam current (I_e) is expressed as follows,

$$I_e = e n_e f_{rev} \tag{2.6}$$

where n_e is the number of electrons (positrons). σ_x^* and σ_y^* are the spreads of the beam in x and y directions, respectively. In general, however, it is difficult to determine these parameters precisely. Thus the luminosity is usually determined by using the number of Bhabha scattering events. Since the cross section of Bhabha events is large and well known, the luminosity can be calculated from the number of observed Bhabha events with a small error.

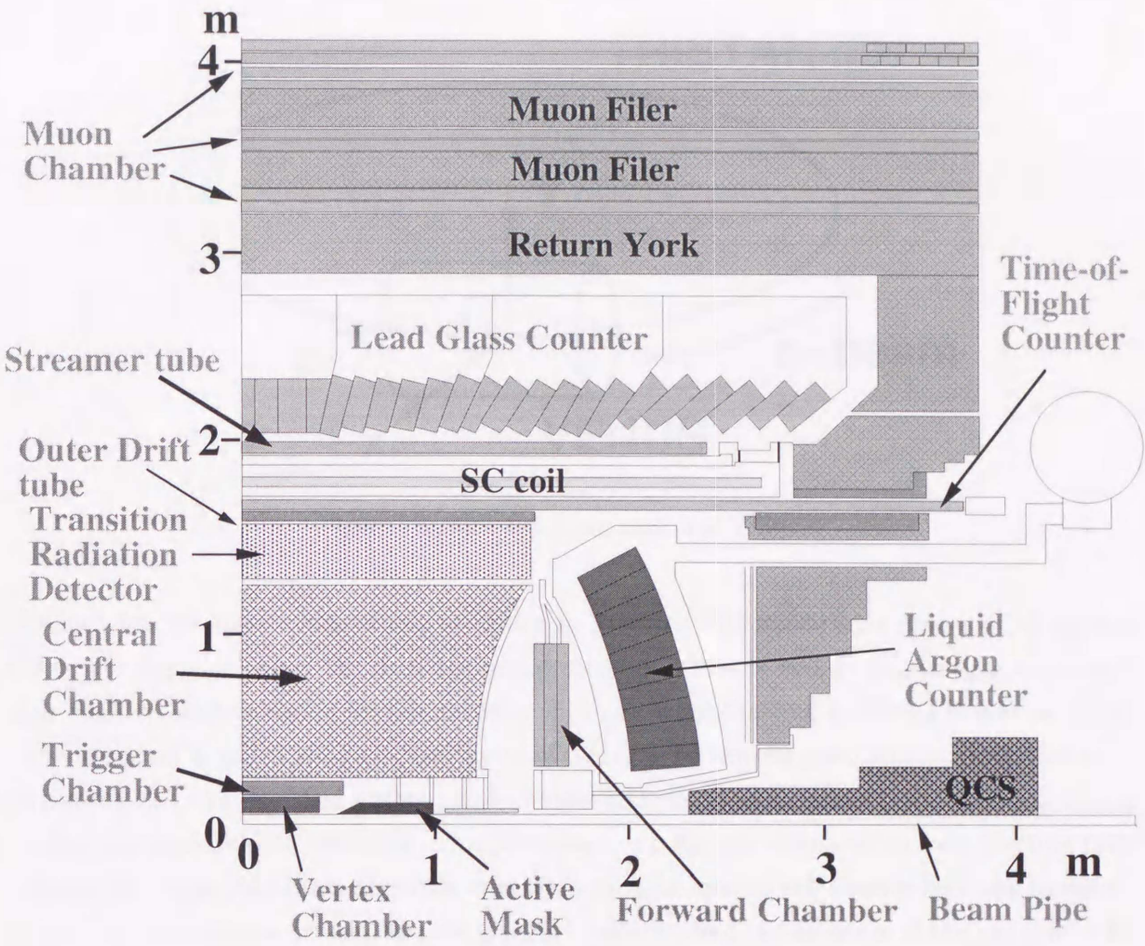

Figure 2.2: A schematic view of VENUS.

2.2 VENUS detector

The VENUS detector [37] is a general purpose magnetic spectrometer designed to study various reactions in e^+e^- annihilations. Figure 2.2 shows a schematic view of the VENUS detector.

The coordinate system of VENUS is shown in Fig. 2.3. The z-axis is defined as the e^- beam direction. The y-axis is defined as the vertical direction. θ and ϕ are defined as the polar and azimuth angles, respectively.

2.2.1 Vertex chamber

The vertex chamber (VTX) [38] is located at the innermost place in the VENUS detector. The purpose of VTX is to precisely determine the decay vertex of hadrons such as B meson in the x-y plane. It is a jet-type drift chamber which has the length of 60 cm and the inner and outer radii of 5.4 and 14.4 cm, respectively. The chamber consists of 12 drift sectors, each

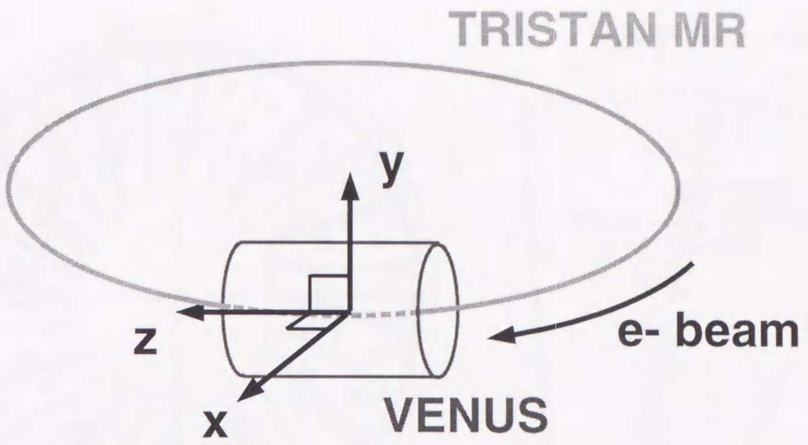

Figure 2.3: The coordinate system of VENUS.

of which has 16 sense anode wires, as shown in Fig 2.4. The anode wire planes of all sectors tilt by the angle of about 15° from the radial direction. This is mainly due to optimization of high quality sensitive region for the particles with any azimuthal angle. Tilting is also useful for resolving what is called left-right ambiguity of a track. To achieve good spatial resolution of $\sim$ 50 μm, we use what is called a slow gas, a mixture of 92% carbon-dioxide (CO_2) and 8% ethane (C_2H_6) at 3 atmospheric pressures. This provides us a large gas volume of uniform electron drift velocity ($\sim$ 7 mm/μs). Since the drift velocity is proportional to the electric field and inversely proportional to the gas density, the electric field, pressure and temperature of the gas should be controlled with stability better than 0.1 % in order to keep the drift velocity constant.

The beam pipe, which is made of beryllium, is a part of the VTX chamber. The material was chosen for its low density and strength against pressure. Its thickness is 0.11 cm and the outer radius and length are 4.9 and 24 cm, respectively. It is covered with 50 μm thick titanium sheets to absorb X rays from beam bremsstrahlung.

Another multi-wire drift chamber (Trigger Chamber (TC)) exists at outside of the VTX. The total material quantities in VTX and TC is about 2.7 g/cm^2 in column density and corresponds to $6.1X_0$ radiation length in the $\theta = 90°$ direction.

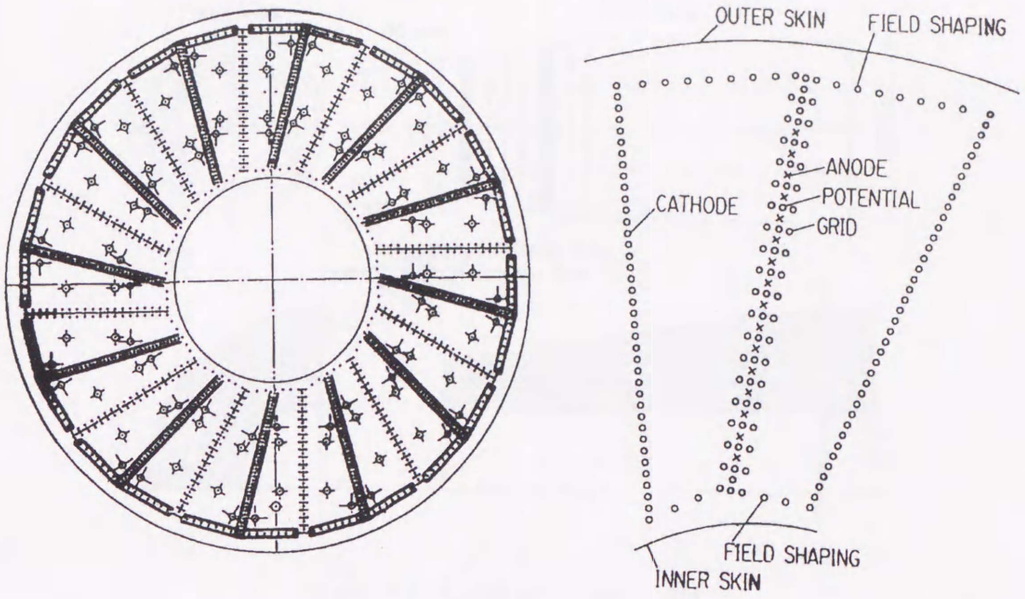

Figure 2.4: Wire configuration of the vertex chamber. (a) shows the whole pattern on the macor endplate of the chamber, and (b) the wire and skin configuration of one sector.

2.2.2 Active mask

The active mask (AM) is a pair of cylindrical sandwich calorimeters [39]. Its role is to measure the number of forward Bhabha events and absorb particles from events such as beam-gas or beam-beampipe interactions, so it is called "active mask". It consists of 0.1 cm thick lead sheets and plastic scintillation fiber sheets as shown in Fig. 2.5 and covers small polar angle regions of $2.6° \sim 8.6°$, $171.4° \sim 177.4°$.

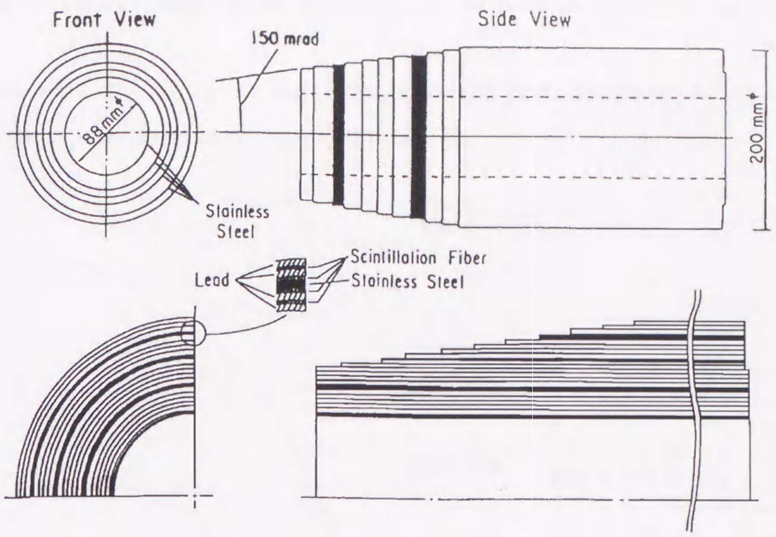

Figure 2.5: A schematic view of AM.

2.2.3 Central drift chamber

The central drift chamber (CDC) is a cylindrical multi-wire drift chamber [40] and is the main tracking device of the VENUS detector. The inner and outer radii of the gas volume are 25 cm and 126 cm, respectively. Its length is 300 cm. It is filled with HRS gas ($Ar:CO_2:CH_2$=89:10:1). This mixture was chosen because of its good properties for long-term operation for a large drift chamber. It is nonflammable, stable against aging and less expensive.

For the track reconstruction in the x-y projection (normal plane to the beam axis), 20 axial layers of drift cells are provided. Every two layers are rotated by half a cell width and combined into one double layer. The z coordinate is determined by using 9 stereo layers tilted by 3° with respect to the z axis. All layers are grouped to form 10 "superlayers" consisting of a pair of axial layers and one stereo layer, except for the innermost superlayer. Furthermore, half the superlayers have an offset of one quarter of a cell width with respect to the other superlayers. If we ignore this small offset, the arrangement of the cells has a 32-fold symmetry in azimuth. The symmetry allows us to design a simple and efficient track trigger logic. One rectangular drift cell of 1.7 cm high and typically 2 cm wide contains one sense wire at the center and surrounding 6 potential wires. The sense wires are gold-plated 30 μm-thick tungsten-rhenium (3%) alloy and stretched with the tension of 60 gW. The potential wires are gold-plated 140 μm-thick molybdenum with the tension of 300 gW. Molybdenum was chosen because of its large yield strength. It makes it easier to replace defective wires after completing the chamber. The maximum gravitational sag is 250 μm for the sense wires and 600 μm for the potential wires. The drift field is provided by applying a positive high voltage, typically 2.1 kV, to the sense wires. The potential wires are grounded. The electric field is almost radial near the sense wire

up to a distance of about 5 mm, while the effect of the potential wires is significant near the potential wires.

Figure 2.6 is a view of CDC in the x-y plane. Charged particles produced at a central region $|\cos\theta| \leq 0.75$ cross a sensitive region of all layers.

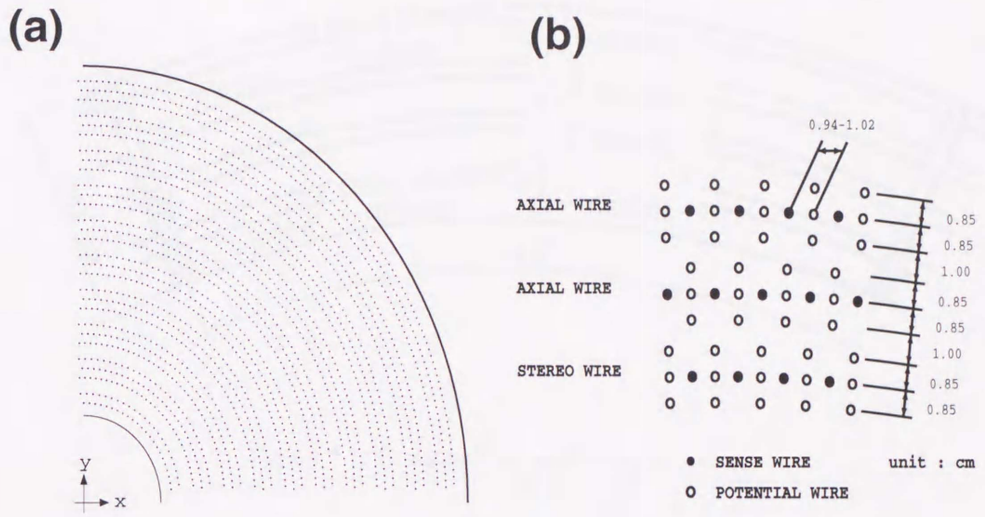

Figure 2.6: Design of the central drift chamber. (a) x-y view of one quadrant and (b) typical drift-cell geometry.

The endplates are 2 cm-thick aluminum plates having a curved shape. The shape was chosen to minimize the deformation due to the wire tension. The maximum deformation was measured to be about 0.05 cm, consistent with the calculation. The wire tension applied to the endplates, amounting to 9 ton in total, is supported by the outer cylinder made of 0.5 cm-thick CFRP (carbon-fiber reinforced plastic). The use of CFRP allows us to reduce the material thickness to approximately 1/2 compared with the case of aluminum. The VENUS CDC is the first large-size drift chamber that has employed CFRP as a major component of the mechanical structure. The inner cylinder, made of 0.1 cm-thick CFRP, serves only as a gas seal. The inside surfaces of the cylinders are lined with aluminum foil, in order to eliminate outgasses and provide a good electrical property.

2.2.4 Transition radiation detector

The transition radiation detector (TRD) is a large cylindrical detector, extending from 127 cm to 157.7 cm radially and 296 cm in the z direction [41]. It covers the angular region of $|\cos\theta| \leq 0.7$.

TRD consists of two components. One is a "radiator box" which contains polypropylene fibers and helium gas. The other is an X-ray chamber which has a thickness of 2 cm and is filled with a gas mixture ($Xe:CH_4$=90:10) to detect transition radiation. TRD is divided into eight

sectors in azimuth as shown in Fig. 2.7 and each sector has four layers of the radiator box and X-ray chamber. Thus 32 pairs of the radiator box and X-ray chamber comprise the detector. The total radiation thickness of TRD is 0.18 X_0 in the radial direction.

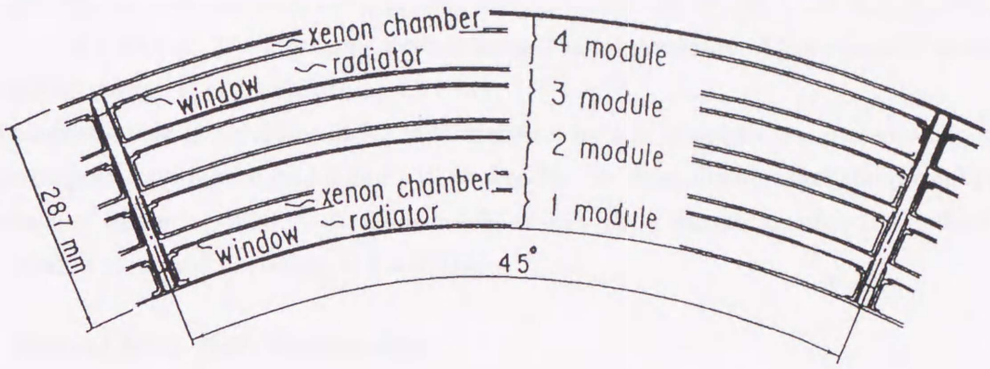

Figure 2.7: Cross section (end view) of TRD.

2.2.5 Time-of-flight counter

The time-of-flight counter system (TOF) consists of 96 plastic scintillator with dimensions of $4.2 \times 10.8 \times 466$ cm^3 [42] as shown in Fig. 2.8. These counters are placed inside of a solenoid coil at the radius of 166 cm and cover the range of $|\cos\theta| \leq 0.81$. There are 0.3 cm gaps between two adjacent counters. These gaps cause the inefficiency of about 3%. Each end of the scintillator is viewed by a photo-multiplier tube (PMT) through a 145 cm long acrylic light guide. The time resolution is estimated to be about 200 psec by using Bhabha and $\mu^+\mu^-$ events.

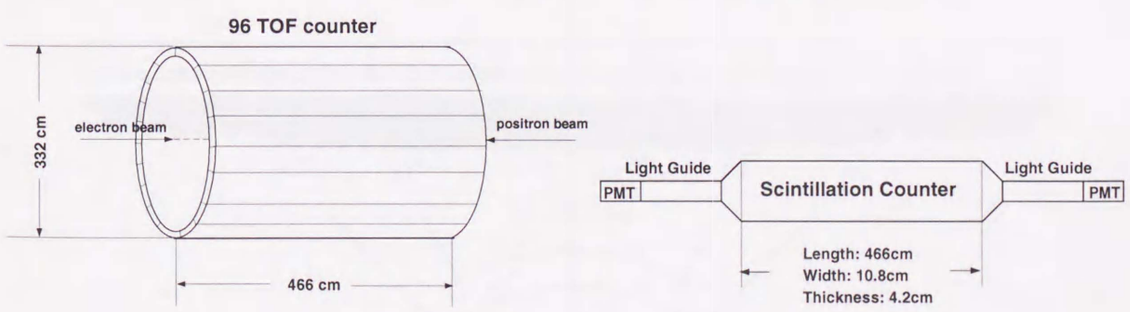

Figure 2.8: Schematic figure of the TOF system.

2.2.6 Magnet system

The magnet system consists of a superconducting solenoid, a flux return yoke, a helium refrigerator and a high current power supply [43]. The superconducting solenoidal coil has its

dimensions of 177 cm in radius and 527 cm in length. It provides a uniform magnetic field of 0.75 Tesla in the beam direction. Its superconducting material is Nb Ti/Cu. The excitation current is 3980 A at 0.75 Tesla. The material thickness in the radial direction is made exceedingly thin, 0.52 X_0.

The iron return yoke supports the magnetic force of about 230 ton with the maximum elastic deformation of 0.04 cm. The cryogenic system keeps the temperature of the solenoid below 4.5 K. The stored energy is estimated to be 11.7 MJ.

The magnetic field in a volume of 3.2 m in diameter by 4 m in length was measured by using a nuclear magnetic resonance probe and hall probes for the three dimensional components with the accuracy of the order of 10^{-4}. A uniform field of 0.75 Tesla was obtained in the entire CDC region within a standard deviation of 0.3 % [44].

2.2.7 Barrel lead-glass calorimeter

The barrel electromagnetic calorimeter (LG) is placed between the superconducting coil and the iron yoke with a radius of 197-230 cm and length of 615 cm in the beam direction (z-axis) [45]. It covers the polar angles from 37° to 143° ($|\cos\theta| \leq 0.799$) and whole azimuthal angles. It is composed of 5160 DF6 lead glass counters: 120 segments in the ϕ-view and 43 segments in the z-θ view.

The lead-glass counters are pointed toward the interaction region with a semi-tower geometry as shown in the cross sectional view of Fig. 2.9. By this configuration, the multihit probability of particles is greatly reduced. Each lead-glass counter has a small tilt with respect to the interaction point in both z and ϕ so that photons from the interaction point cannot escape through 0.15 cm gaps between blocks.

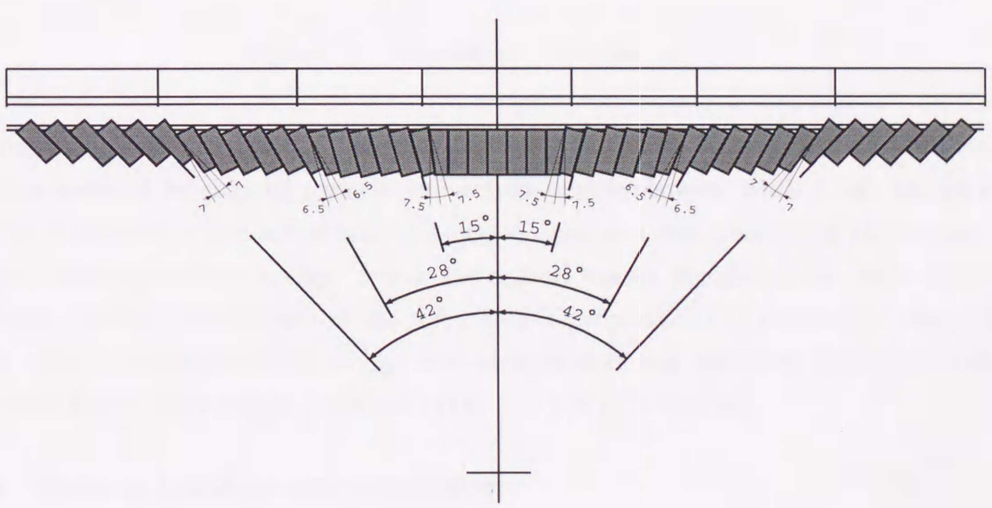

Figure 2.9: Cross-sectional view of the lead-glass calorimeter.

An LG module is made of DF6 whose main components are PbO (70.9 %) and SiO_2 (27.3 %), and has properties such as the radiation length of 1.69 cm, the critical energy of 12.6 MeV and the refractive index of 1.805. A typical LG module size is 12 × 11.6 cm^2 in cross section and 30 cm in length, corresponding to 18 radiation lengths. The schematic cut view of an LG module is shown in Fig 2.10. A 3-inch PMT surrounded by a μ-metal magnetic shield is attached to each LG module together with a plastic light guide of 5 cm in length. At the central part of the LG calorimeter, the box and grid-type PMTs are used, while at the both end parts where the leakage field is 20 to 30 Gauss, mesh-type PMTs are used. High voltage ranging from −1.5 to −2.0 kV is applied for PMTs during data taking. In order to trace gain fluctuations of the PMTs, a monitoring system of a Xe flash tube with an optical fiber bundle is used.

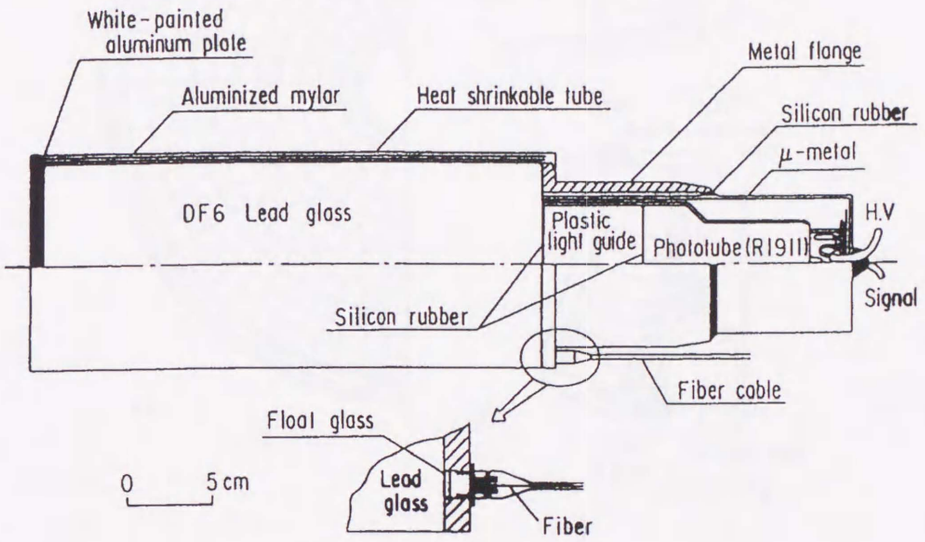

Figure 2.10: Assembly of a lead-glass module.

Energies are measured with Čherenkov lights ($\sim 10^3$ photoelectrons for a 1 GeV electron) which are radiated by charged particles in electromagnetic showers. Such a high energy shower develops by successive bremsstrahlung and electron-positron pair creation by photon until their energies reach the critical energy. Below the critical energy, ionization by collision processes dominates. So the total amount of the light yield is proportional to the energy deposit in LG blocks. The relation between the energy and the light yield was calibrated by using the electron beam from the internal target beam line (IT4) at TRISTAN-AR [46].

2.2.8 Endcap liquid argon calorimeter

The liquid argon calorimeter (LA) is a sampling calorimeter for measuring electromagnetic shower energies produced by electrons and photons in the forward and backward regions [47]. A pair of liquid argon calorimeters are installed between CDC and the endcaps of the return yoke.

Each one covers an angular range of $0.79 \leq |\cos\theta| \leq 0.99$ as shown in Fig. 2.11. Each calorimeter consists of 480 tower structure modules of 20.3 radiation lengths as shown in Fig 2.11. Each tower module is made out of 71 calcium-lead plates with a thickness of 1.5 mm and the gap between lead plates of 3.0 mm.

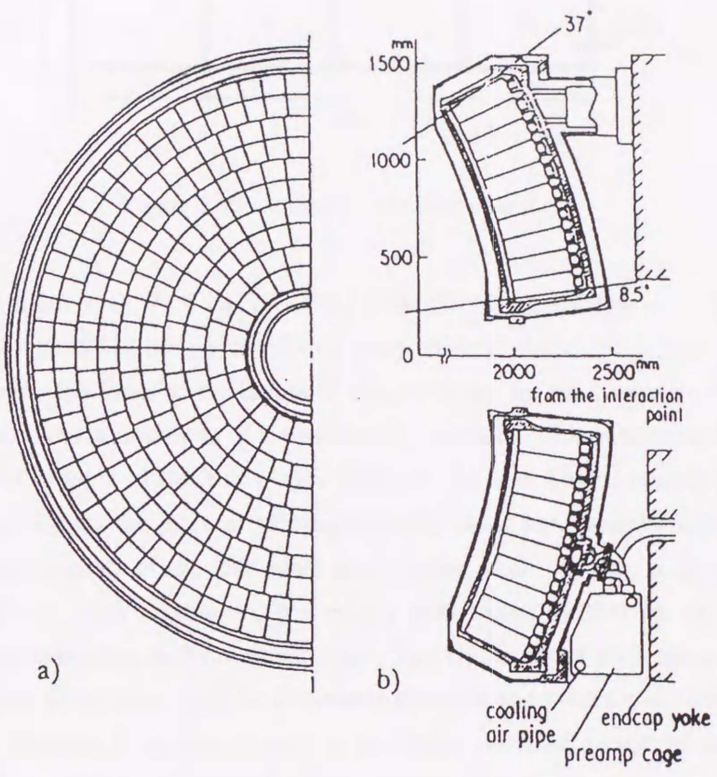

Figure 2.11: Schematic view of LA. (a) Front view of the calorimeter module arrangement and (b) side view of the liquid argon calorimeter.

2.2.9 Muon chamber system

The muon chamber system (MU) covers the large outermost area of VENUS to detect muons [48]. It consists of two main parts: the barrel part and the forward-backward part. The barrel part consists of three layered arrays in r-ϕ view, and one layer arrays in z-view, of extruded aluminum modules, each with 8 cells of drift tubes; whereas the forward-backward part consists of two layered arrays of the modules. A module consists of two layers of four cells staggered by a half cell as shown in Fig. 2.12.

Each cell has the cross-section of 5×7 cm^2 with the wall thickness of 0.25 cm on average. Lengths of the modules are 760 cm for the barrel part, and vary from 245 cm to 505 cm depending on the location for the forward-backward part. A sense wire of 70 μm in diameter made of gold-plated tungsten with 3 % rhenium is stretched at the center of each cell with a tension of 400

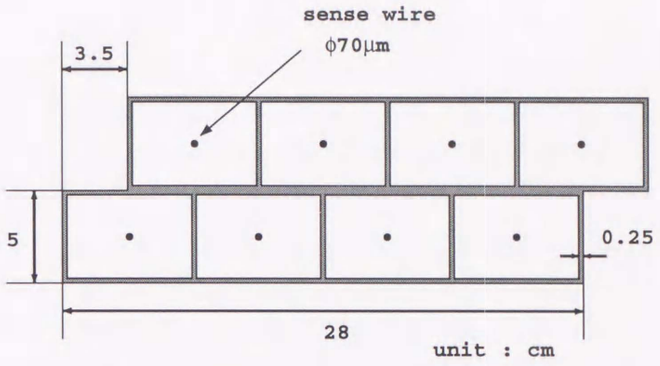

Figure 2.12: A module of muon chamber.

gW. The tubes are filled with P-10 gas (Ar:CH_4 = 90:10). High voltage of 2.7 kV is applied to each sense wire and the tubes are operated in a proportional mode.

In the barrel part, the inner three layers of the modules, interleaved with 20 cm thick iron filters, measure the x and y positions of a penetrating particle. The outermost layer of module, which is located just outside of the third layer without any iron filters, measures the z-position of the track. In this region, the main absorbing material along the particle path generated from the interaction point consists of the lead glass calorimeter, their support rings made of 17.5 cm thick iron and 10.0 cm thick aluminum, the return yoke made of 30.0 cm thick iron and two muon filters, each comprising 20.0 cm thick iron. The thickness of each muon filter is chosen to be about 1 nuclear absorption length. Distances between the return yoke and the first muon filter and between 2 muon filters are chosen to minimize possible decays of surviving $\pi^{\pm}$ and $K^{\pm}$. Muons should penetrate at least 5.3 absorption lengths of materials up to the outside of the VENUS detector.

2.3 Event trigger system

The trigger system is composed of two levels; a first-level trigger designed to work between beam crossings and a second-level trigger which is a slower software track trigger.

2.3.1 First-level trigger

The trigger decision must be made within a collision interval of 5 μsec, so the first-level trigger system consists of hardware logics only. The first-level trigger is issued when the beam-crossing signal and the signal issued by a trigger generation circuit coincide. Inputs to the trigger decision module are track patterns reconstructed by CDC, hit information of TOF, and analog-sum signals from the calorimeters as shown in Fig. 2.13.

Track pattern recognition with a track-finder module is shown in Fig. 2.13. The axial-layer cells of CDC are grouped to 64 trigger-cells divided in azimuth in each superlayer.

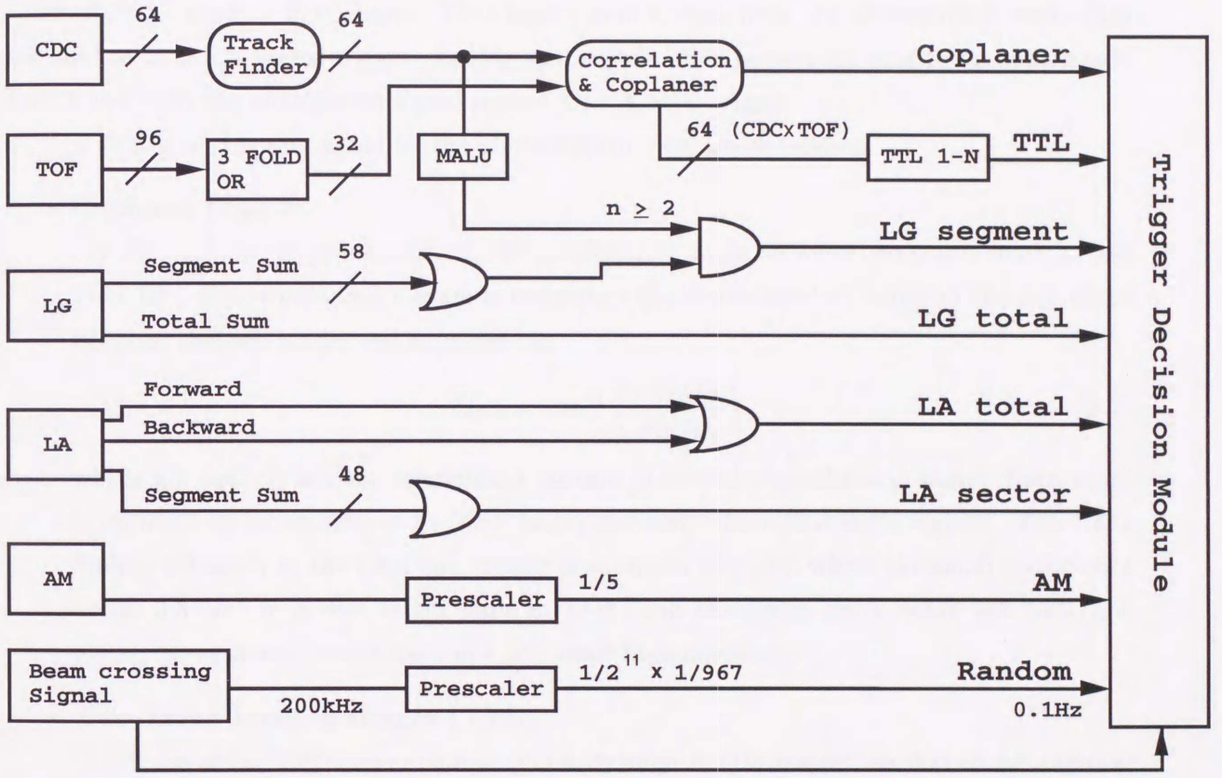

Figure 2.13: Block diagram of the trigger system.

The track-finder module recognizes tracks by comparing the trigger-cell hit pattern from the inner 7 superlayers with a pre-loaded look-up table. The pattern of the look-up table is so defined that the track finders should have nearly the full efficiency for tracks which have transverse momenta p_t above 0.6 GeV/c with respect to the z axis [49].

To form LG event trigger, LG is divided into 58 segments *i.e.* 7 segments in the z-direction and 8 or 10 segments in the ϕ direction. The analog-sum signal of each segment is used for LG segment trigger. Also all 58 segment-sum signals are sent to an analog-sum circuit and then these analog-sum signal is used for LG total trigger. Similarly, each of the LA calorimeters is divided into 12 sectors in azimuth and each sector is further divided into inner ($0.91 \geq |\cos\theta| \geq 0.99$) and outer ($0.79 \geq |\cos\theta| \geq 0.91$) parts. Thus analog-sum signals from the 48 sectors in both sides are used to form LA sector trigger. Analog-sum signals of 48 sectors are sent to an analog-sum circuit and then the analog-sum signal is used for LA total trigger.

The first-level triggers based on the above information are as follows:

- **Coplanar trigger**

  For the coplanar trigger condition, the acoplanarity angle between two tracks must be less than 10°. The acoplanarity angle is defined as the supplementary angle in the x-y plane between the two tracks and expressed as

  $$\theta_{\rm acop} = \cos^{-1}\left(\frac{-\vec{p_{t1}}\vec{p_{t2}}}{|\vec{p_{t1}}||\vec{p_{t2}}|}\right), \tag{2.7}$$

  where $\vec{p_{t1}}$ and $\vec{p_{t2}}$ are the momentum vectors projected onto the x-y plane. Each track is required to be associated by TOF hit(s) at nearly azimuthal-angle regions. The track finding efficiency in the Coplanar trigger is shown in Fig 2.14, where the small inefficiency above 0.6 GeV/c is due to the gaps in TOF, and the rising curve below 0.6 GeV/c is mainly determined by the logic of CDC track finding system.

- **Two-Track-Limited trigger (TTL)**

  Condition of the TTL trigger (the acoplanarity angle cut) is looser than that of the coplanar trigger and is extended to 25°.

- **LG segment sum trigger**

  At least 2 tracks are recognized by "track finder" without requiring the TOF association and at least one of LG segments has an energy deposit larger than 0.7 GeV.

- **LG total sum trigger**

  A total energy deposit in LG is larger than 3 GeV.

- **LA sector sum trigger**

  At least one of LA sectors has an energy deposit larger than 2 GeV.

- **LA total sum trigger**

  At least one side of LA has a total energy deposit larger than 4 GeV.

- **Active mask trigger**

  Total energy deposit is larger than 10 GeV in back-to-back configuration. The back-to-back configuration means that the signals are induced at both symmetric positions of a pair of active masks, with respect to the collision point.

- **Random trigger**

  Random trigger is made by the beam-crossing signal. Beam-crossing is scaled down by a factor of 2×10^6. This trigger occurs every 10 sec.

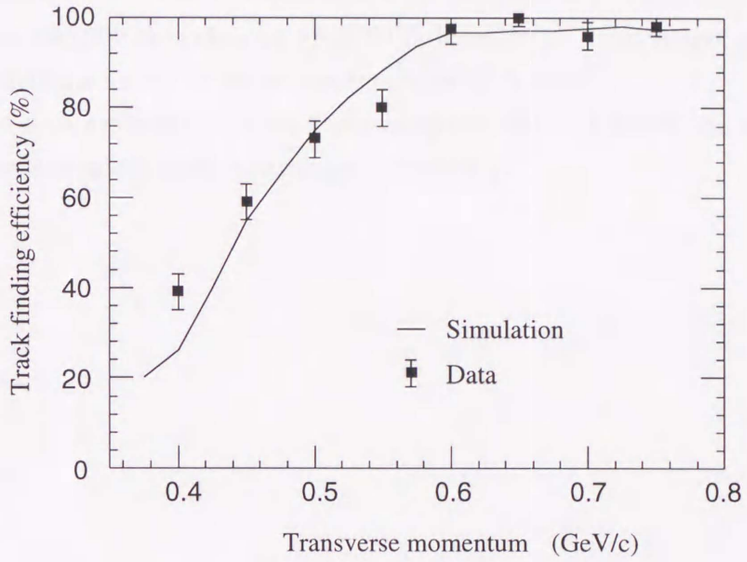

Figure 2.14: The track-finding efficiency in the Coplanar trigger logic (after the association of TOF). The closed circles indicate the results obtained from the experimental data, and the solid line presents the result of Monte Carlo simulation.

2.3.2 Second-level trigger

A second-level trigger uses slower software [50]. At the first-level, we find tracks in CDC by making use of the track finder. The information is sent to another electronic circuit which makes a ϕ correlation by combining the information from TOF counters. Flexibility and high granularity in the first level trigger require a large number of wires and a complex circuit, and thus the logic in the ϕ correlation is limited by hardware restriction. Indeed, the TTL triggered events contain large backgrounds which originate from interactions of beam particles with the beam pipe. When an event is triggered only by TTL trigger, the second-level trigger is applied to the event. A micro-processor 68K20FPI carries out refined track finding by combining CDC and TOF hit information in the ϕ regions where tracks have been found at the first-level trigger. The second-level trigger can improve the vertex resolution, and thus reduce background events.

The total trigger rate is typically $5 \sim 7$ Hz and dead time is 5 % though it depends strongly on the beam condition.

2.4 Data acquisition system

The data acquisition system (DA) [51] has a tree-like structure as shown in Fig. 2.15. For the front-end electronics, several data buses such as CAMAC[4], TKO[5], and FASTBUS[6] are used. These buses handle about 30,000 electronic readout channels in total. All digitized data from the front-end electronics of the detector components are transferred to FASTBUS memory buffers and collected by a 68K20FPI module on FASTBUS whenever an event trigger occurs. And then all data in 68K20FPI are read by an on-line computer VAX6330.

The collected data are sent to a main frame computer FACOM M1800 via optical fibers and then stored in an automatic loading cartridge tape library.

[4] CAMAC is an international standard of modularized electronics as defined by the ESONE Committee of the JRC, Ispra.

[5] TKO is a system of front-end electronics developed at KEK

[6] The standard modular high-speed data acquisition and control system defined by ANSI/IEEE std 960-1986

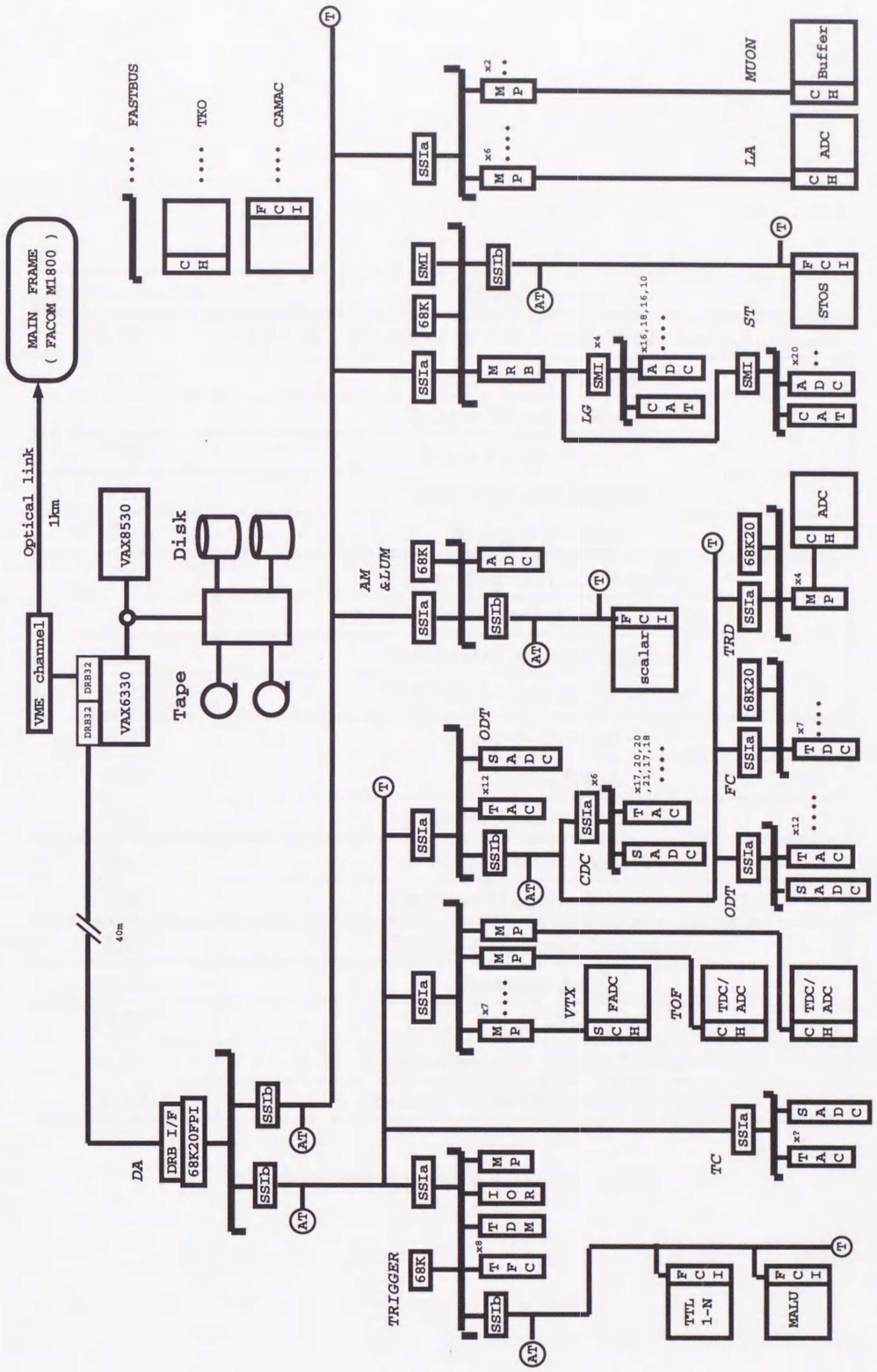

Figure 2.15: Data acquisition system of VENUS. The notations are listed in the Table 2.2.

Representation	Module name
68K20FPI	FASTBUS Processor Interface with 68020 micro-processor
DRB	general propose bus of DEC
TDR	Trigger Decision Module
TFC	Track Finder for CDC
IOR	Input/Output Register
MUL	Majority Module
SSI	Simplex Segment Interconnect
AT	Active Terminator of cable segment
T	Terminator of cable segment
FCI	FASTBUS-CAMAC Interface
MP	Memory Partner
CH	Controller Head
SCH	Super Control Head
MRB	Multi-Record Buffer
SMI	Segment Manager Interface
TAC	Time-to-Amplitude Converter
SADC	Scanning ADC
FADC	Flush ADC
CAT	Calibration and Trigger Module
STOS	Streamer Tube Operating System

Table 2.2: Lists of modules in the DA system.

Chapter 3

Event reconstruction

Data taken by the DA system are composed of digitized quantities from ADC, TDC etc. So they are called "raw data" and need to be reconstructed to tracks and clusters before physics analyses. Reconstructed events are classified into several categories, *e.g.* hadronic events, low multiplicity events and Bhabha events, depending on physics processes. In this chapter, the method of event reconstruction and data reduction is presented.

3.1 Track reconstruction in CDC

The measurement of momentum and charge of a charged particle is performed by reconstructing its trajectory in CDC. The track reconstruction in CDC is carried out by using the pattern recognition program named PERPR [52].

Since a magnetic field of 0.75 tesla is applied along the z-axis, the charged particle spirals in the 3 dimensional space, and thus its trajectory makes a circle in the x-y plane. The projected momentum in the x-y plane, p_t (GeV/c), can be obtained from the relation

$$p_t = 0.3 \cdot B \cdot \rho \tag{3.1}$$

where B is the magnetic flux density in tesla, and ρ is the radius of curvature in m. In the PERPR program, track reconstruction in the x-y plane is done by using axial wire information at first. If we succeed the above reconstruction, we try to reconstruct a track in three dimensions by using slant wire information. The basic procedure of the track reconstruction in PERPR is described below.

Reconstruction in the x-y plane

1. An "initial road" is searched at the outermost two layers of CDC. If hits are found in both layers, the 'road' of the track is defined. Thus, four possible combinations of a track due to left-right ambiguity are taken into account as shown in Fig. 3.1.

2. Then candidate hits along the 'road' are searched. The left-right ambiguity is solved by fitting with axial wire positions. To find a most likely track, the least χ^2 fit is performed

by eliminating hits of poor quality. If χ^2 exceeds 5.0, the track is abandoned.

3. The curvature of the track is calculated from the above formula and some relevant quantities such as charge and p_t are calculated.

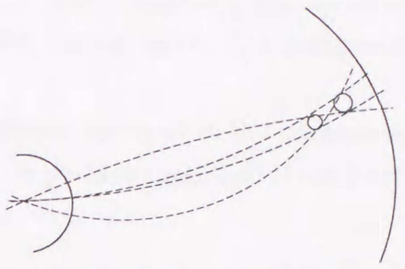

(a) Define initial road at the outermost two layers.

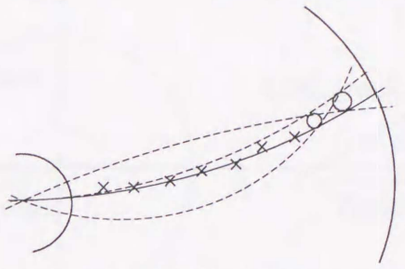

(b) Search hit cells along the road.

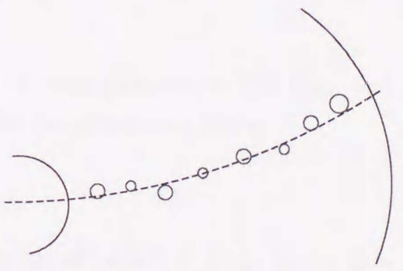

(c) Obtain the most probable trajectory.

Figure 3.1: Track reconstruction procedure: (a) to determine the initial road, (b) to search for hit cells along the road and then make a trajectory fit, and (c) to obtain the most probable trajectory.

Reconstruction in the z-s plane

Slant-layer hits are used in association with axial-layer hits to determine a three-dimensional trajectory. Since slant wires are inclined by 3.5 degrees with respect to axial wires, the z coordinate of the track can be given by

$$z = \frac{l}{2} - \frac{d}{\tan\alpha}, \tag{3.2}$$

where d is the distance between the axial track and the stereo hit, α is the slant angle (3.5°) and l is the wire length of the slant wire projected onto the beam axis.

The overall trajectory can be expressed in a linear form as

$$z = \frac{\mathrm{d}z}{\mathrm{d}s}s + Z_{\mathrm{min}} \tag{3.3}$$

where Z_{min} is the distance at the closest approach in the x-y plane, s is the length of the arc element measured from the closest approach and $\mathrm{d}z/\mathrm{d}s$ is the gradient. The track finding algorithm is similar to that for the x-y plane. The configuration of a CDC track is illustrated in Fig. 3.2.

Here the distance of the closest approach to the interaction point in the x-y plane is defined as R_{min}. We define R_{min} to be positive (negative) if the interaction point lies inside (outside) the circle of a track.

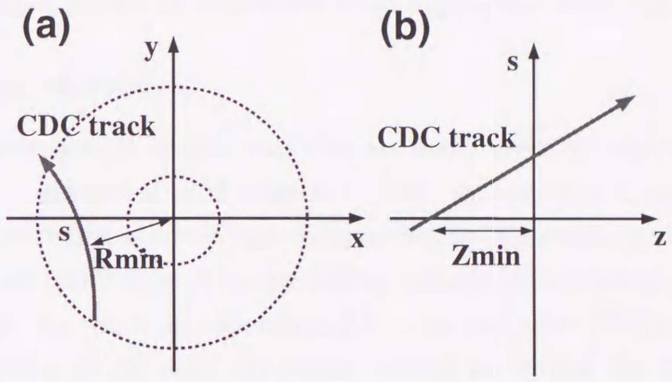

Figure 3.2: Definition of track parameters: (a) R_{min} and (b) Z_{min}. Both figures show in the case of negative values.

Tracking performance

For charged tracks in the range of $|\cos\theta| < 0.75$, where they are able to pass through all the axial and slant layers of CDC, tracking performance has been evaluated using Bhabha scattering events. The vertex resolutions for high-p_t tracks have been found to be

$$\sigma_{\mathrm{vertex}}(xy) \approx 460 \quad \mu\mathrm{m} \tag{3.4}$$

$$\sigma_{\mathrm{vertex}}(z) \approx 0.67 \quad \mathrm{cm}. \tag{3.5}$$

In the same way, the angular resolutions in the azimuthal and polar angles have been estimated to be

$$\sigma_\theta = 8\sin^2\theta \quad \mathrm{mrad} \tag{3.6}$$

$$\sigma_\phi = 1.3 \quad \mathrm{mrad}. \tag{3.7}$$

The measurement of the polar angle is much less accurate than that for the azimuthal angle.

The momentum resolution is found to be

$$\frac{\sigma_p}{p} = \sqrt{(0.013)^2 + (0.008 \times p_t)^2} \tag{3.8}$$

with p and p_t in GeV/c in a magnetic field of 0.75 Tesla using cosmic ray and Bhabha data samples. The first term in Eq. (3.8) is the contribution from multiple coulomb scattering by materials in the tracking volume, *i.e.* the chamber gas and the wires. The second term is due to measurement errors in the drift distance. The reconstruction efficiency for the high-p_t charged tracks in the range of $|\cos\theta| \geq 0.75$ has been studied by collinear Bhabha events and found to be better than 99.9 % in the x-y plane.

3.2 LG clustering

Since an electromagnetic shower generally spreads over several LG blocks, the shower energy and its incident position should be determined by an appropriate clustering method.

3.2.1 Clustering Method

The intrinsic limitations in spatial resolution are firstly given by detector granularity, and secondly given by lateral spread of the electromagnetic shower. The lateral spread is mainly caused by multiple scattering of low-energy electrons that no longer radiate any photons and drift away from the shower center axis. A proper scaling variable for the lateral shower distribution is the *Moliere radius* R_M which corresponds to 2.8 cm for lead-glass (DF6).

Accordingly, several blocks share the shower energy permitting the measurement of the shower center position. The clustering and measurement of the shower center are performed as follows:

1. Starting from a module which contains the highest energy, neighboring modules are examined whether they belong to the same cluster or not. Thus, a "connected region" is formed by searching all neighboring modules adjacent in the ϕ or θ direction.

2. The shower energy is calculated by summing up the energies in the same cluster.

3. The incident position of the showering particle is determined by the energy weighted average of the position of LG blocks in a cluster as follows:

$$x_{\text{cluster}} = \frac{\sum E^{\alpha} x}{\sum E^{\alpha}}, \tag{3.9}$$

where x is the central ϕ- or θ-position of a block and $\alpha = 0.34$ which was optimized by a shower simulation calculation using EGS4 [53].

3.2.2 Performance of LG cluster reconstruction

The energy resolution for an electron evaluated using $e^+e^- \rightarrow e^+e^-$, $e^+e^-\gamma$ and $e^+e^-e^+e^-$ events is given as

$$\frac{\sigma_E}{E} = 0.025 + \frac{0.07}{\sqrt{E}}, \tag{3.10}$$

where E is in GeV. The first term accounts for the effects such as instrumental noise, shower leakage and inter-calibration error, whereas the second term comes from the statistical fluctuation of the number of photoelectrons.

The angular resolution of the calorimeter can be studied by comparing the measured shower center positions with CDC tracks extrapolated to LG module surfaces for large angle Bhabha scattering. The angular resolution has been measured to be

$$\begin{aligned} \sigma_\theta^{\mathrm{LG}} &= 4.0\mathrm{mrad}, \\ \sigma_\phi^{\mathrm{LG}} &= 5.2\mathrm{mrad}. \end{aligned} \tag{3.11}$$

3.3 LA clustering

3.3.1 Clustering method

The cluster finding algorithm for LA is similar to that for LG except that only adjacent towers are included in the search and not for towers in the diagonal direction. The center of the cluster is measured by a shower-profile method. It is known that the lateral shower spread $E(x)$ of the electromagnetic shower can be expressed by the following double exponential form [54]:

$$E(x) \cong E_1 exp(-\frac{|x|}{\lambda_1}) + E_2 exp(-\frac{|x|}{\lambda_2}), \tag{3.12}$$

where x is the lateral distance from the shower center, and λ_1 and λ_2 represent the shower extension. The first term is the central component which describes the multiple coulomb scattering of the electrons and positrons in the material. The second term is the peripheral component which arises via isotropic propagation of photons. In principle, the shower center can be obtained by solving the above equation but this is generally difficult. To make the problem easier, only one exponential term has been considered. The slope parameter λ has been taken as a function of lateral energy so that

$$\lambda = g(y), \tag{3.13}$$

with

$$y = ln\frac{1}{2}(\frac{E_i}{E_{i+1}} + 1), \tag{3.14}$$

where E_i represents the energy deposit in the i-th tower. The function $g(y)$ has been parameterized for high-energy electromagnetic showers by using EGS4 [53].

3.3.2 Performance of LA cluster reconstruction

The energy resolution of LA has been studied using radiative Bhabha scattering events, and found to be

$$\frac{\sigma_E}{\sigma} = 0.016 + \frac{0.102}{\sqrt{E}}, \tag{3.15}$$

where E is in GeV. Similarly to the LG case, the first and second terms are due to intrinsic noise and statistical fluctuation, respectively. The normalization factor for the energy calibration is given by measuring energies of Bhabha events. The angular resolution of the calorimeter has been studied by the same method as that used for LG. It is obtained to be

$$\sigma_\theta^{\mathrm{LA}} = 2.9 \quad \mathrm{mrad}, \tag{3.16}$$

$$\sigma_\phi^{\mathrm{LA}} = \frac{2.6}{\sin\theta} \quad \mathrm{mrad}, \tag{3.17}$$

where the errors are determined by fitting the result.

Chapter 4

Monte Carlo Simulation

In order to estimate the detection efficiency and to compare the data with theoretical predictions, a Monte Carlo (MC) simulation is applied. The MC simulation has two steps:

- the event generation and
- the simulation of decays and interactions of generated particles in the VENUS detector materials.

4.1 Event generation

We used the event generator program for the two-photon process at an e^+e^- collider, TREPS [55]. This program generats the simulated events at a specified fixed $\gamma\gamma$ center-of-mass energy using an equivalent photon approximation (EPA) [56] in which the virtuality of photons was taken into account as described in Sec. 8.1 in detail. The kinematics in the event was precisely calculated so that the final state particles give a conserved 4-momentum and the proposed value exactly within the accuracy of the computation. It was applicable to various processes by specifying a combination of final-state particles and angular distributions among them. The accuracy of the calculation was tested by comparisons with other programs [57,58]. The three-dimensional momentum distributions of the two-photon system were in very good agreement with those expected from a full diagram calculation for the process $e^+e^- \to e^+e^-\mu^+\mu^-$ [58].

The process of K^0_S decay into $\pi\bar{\pi}$ was simulated by using LUEXEC program in JETSET 7.4 [59]. LUEXEC simulated the whole fragmentation and decay chains. In this program the decays of hadrons containing u, d and s quarks into two or three particles were simulated by assuming that the momentum distributions were given by phase space. The branching ratios and lifetimes were given by PDG [60]. In the case of K^0_S, the branching ratio used was 0.686 for $\pi^+\pi^-$ and 0.314 for $\pi^0\pi^0$ and the $c\tau$ was 2.675 cm.

4.2 Detector simulation

In order to simulate decays and interactions of the particles mainly with a long lifetime and to simulate the response of the VENUS detector, we used a detector simulator called VMONT. Several reactions simulated by VMONT were as follows:

- Decays of hadrons ($\pi^{\pm}$, $K^{\pm}$ etc.) and leptons ($\mu^{\pm}$ and $\tau^{\pm}$) were simulated. Positions of decay vertices and time-of-flights were also able to be calculated even for particles with short lifetimes, such as K^0_S, Λ and D mesons as well as those with long lifetimes.
- Multiple Coulomb scattering, energy losses and nuclear interactions were simulated.
- For calorimeters, electromagnetic cascade showers in the detectors were simulated by using the actual geometry and materials coded in VMONT. Electromagnetic showers in the calorimeters, which originated from electrons and/or photons were simulated by EGS4 [53]. Based on the information obtained from EGS4, the responses of calorimeters were calculated. The calorimeter response for hadrons and muons was also calculated on the basis of the beam test data.
- The responses of chambers were simulated by taking into account the relation between the drift time and the drift length. The resolution of each chamber was also taken into account. The simulation of detector responses used the tuned response of each chamber.

Among the interactions of particles in the detector materials, nuclear interactions were expected to be much more complicated than other interactions. We adopted a simplified model for these interactions, and optimized it by using information from experimental data. The interactions in the materials at small radii were studied by investigating various properties, such as the vertex distribution, of low momentum tracks in multihadron events. Further information, mainly concerning the large angle scattering and absorption in the materials at larger radii, was obtained from the studies of the LG response.

Chapter 5

Event Selection

In this chapter we describe the procedure in which we selected two-photon events from events triggered by the *coplanar* or TTL mode. The selection criteria for two-photon collision events were optimized in order to minimize any background contamination and maximize the detection efficiency. Two-photon processes are characterized by small visible energies and good transverse momentum balance. Because we were interested in production from collisions of nearly real photons, we selected so-called no-tag events, in which the recoiled e^+ and e^- escaped from the detector into small angles.

5.1 Preselection

Events of $p\bar{p}$-pair or K^0_S-pair production in two-photon collision events were selected from the preselection sample. This preselection sample consisted mainly of events with low charged-particle multiplicity. The preselection was based on only CDC information. The selection criteria were as follows:

1. The number of tracks reconstructed in CDC was between 2 and 20. The reconstructed tracks might contain those tracks which were not three-dimensionally reconstructible.

2. Among these tracks, at least 2 tracks satisfied the following conditions:

   - $N_{\rm axial} \geq 10$, $N_{\rm stereo} \geq 4$,
   - $|R_{\rm min}| \leq 2.0$ cm,
   - $|Z_{\rm min}| \leq 15.0$ cm and
   - $p_t \geq 0.2$ GeV/c.

3. Among the tracks selected by condition 2, at least one track satisfied the condition, $Q/p \leq 0.5$ (GeV/c)$^{-1}$, where Q is the electric charge of the track ($= \pm 1$).

Condition 3 requires the existence of at least one negative-charge or high-momentum ($p_t \geq 2$ GeV/c) track. This requirement efficiently reduced the contamination from beam-gas and beam-beam pipe interactions.

In this preselection we applied a truncated version of the track reconstruction program in order to save the CPU time. The selection criteria were looser enough for the real collision events.

5.2 Selection of $e^+e^- \to (e^+e^-)p\bar{p}$ events

After the standard track reconstruction was applied, we selected $e^+e^- \to e^+e^-\gamma\gamma \to (e^+e^-)p\bar{p}$ events from the preselection sample.

5.2.1 Selection of two track events

The selection criteria for two track events were as follows:

1. $N_{\rm good} = 2$.
   $N_{\rm good}$ was defined as the number of good tracks which satisfied the following requirements:
   - $N_{\rm axial} \geq 8$, $N_{\rm stereo} \geq 4$,
   - $|R_{\rm min}| < 1.0$ cm,
   - $|Z_{\rm min}| < 10.0$ cm,
   - $|\cos\theta| < 0.8$,
   - $p_t > 0.2$ GeV/c and
   - TOF hit connection.
2. Net charge of good tracks = 0.
3. $p_t > 0.45$ GeV/c for both good tracks.
   This requirement was set to ensure substantial efficiency of the event trigger.
4. $|\Delta t_{\rm TOF}| \leq 5$ ns.
   $|\Delta t_{\rm TOF}|$ is the time difference between the two tracks measured by TOF as shown in Fig. 5.1. In this condition, cosmic-ray events were effectively rejected, because cosmic rays had a typical time difference of 10 ns.

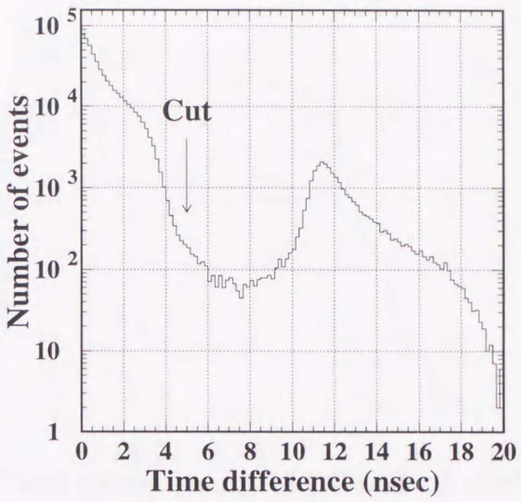

Figure 5.1: The time difference between the two tracks measured by TOF.

5.2.2 Rejection of background events

In order to reduce backgrounds such as single-photon annihilation events and non-exclusive events, we applied the following requirements:

1. $E_{\rm total} \leq 5.0$ GeV.
   $E_{\rm total}$ was defined as the total cluster energy in LG and LA. This cut was effective to reduce hadronic single-photon annihilation process events. Figure 5.2 shows the total cluster energy in LG and LA for two track events.

2. $N_{\rm other} = 0$.
   $N_{\rm other}$ was defined as the number of other tracks which came from the neighborhood of the collision point and satisfied the following properties,

   - $N_{\rm axial} \geq 8$, $N_{\rm stereo} \geq 4$,
   - $|R_{\rm min}| < 2.0$ cm and
   - $|Z_{\rm min}| < 20.0$ cm.

3. $|\sum \vec{p}_t| \leq 0.2$ GeV/c.
   $|\sum \vec{p}_t|$ was defined as the vector sum of p_t of the two good tracks. This cut was applied to reject non-exclusive $p\bar{p}$ events and to restrict the virtuality of colliding photons.

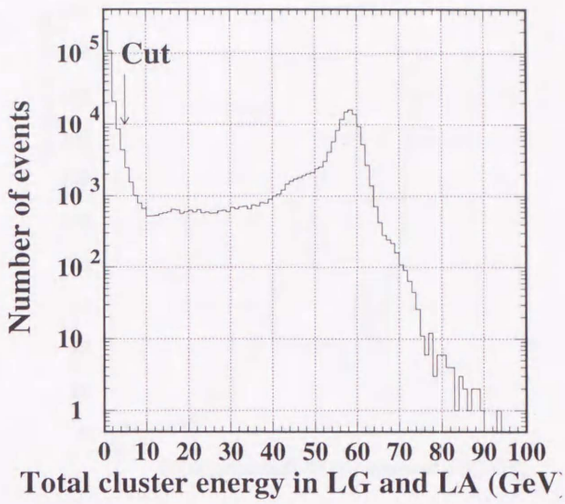

Figure 5.2: The total cluster energy in LG and LA for two track events.

5.2.3 Particle identification

Two tracks were identified as a proton and an antiproton by using CDC and TOF information. In addition, both tracks were required to satisfy the following conditions:

1. $p \leq 1.5$ GeV/c.
   This limit was to preserve a good K/p separation by the flight-time measurement.

2. $|\mathrm{TOF_{expected}} - \mathrm{TOF_{measured}}| \leq 3\sigma_{\mathrm{TOF}}$.
   $\mathrm{TOF_{measured}}$ and $\mathrm{TOF_{expected}}$ were the measured flight-time and that expected from the momentum and the path length, respectively. The proton mass was assumed for the tracks. σ_{TOF} was a standard deviation evaluated from the quadratic sum of the errors of the quantities used,
   $$\sigma_{\mathrm{TOF}} = \sqrt{\sigma^2_{\mathrm{TOFinitrinsic}} + \sigma^2_{\mathrm{CDC}}}. \tag{5.1}$$
   A typical value was 250 ps for a hadron track.

3. $|\mathrm{Mass_{proton}} - \mathrm{Mass_{TOF}}| \leq 100$ MeV/c^2.
   $|\mathrm{Mass_{TOF}}|$ was defined as the estimated mass from the TOF measurement. By this cut, the contamination from pions and kaons in high momentum regions was reduced.

Figure 5.3 shows the distribution of $|\mathrm{TOF_{expected}} - \mathrm{TOF_{measured}}|/\sigma_{\mathrm{TOF}}$ for the sample after the requirement for momenta lower than 1.5 GeV/c.

Figure 5.4 shows the correlation between the estimated masses of the two tracks, for the sample after the requirement for momenta lower than 1.5 GeV/c. A cluster of $p\bar{p}$ events is clearly separated from other combinations of particles such as $\pi^+\pi^-$, K^+K^-, $p\pi$ and so forth.

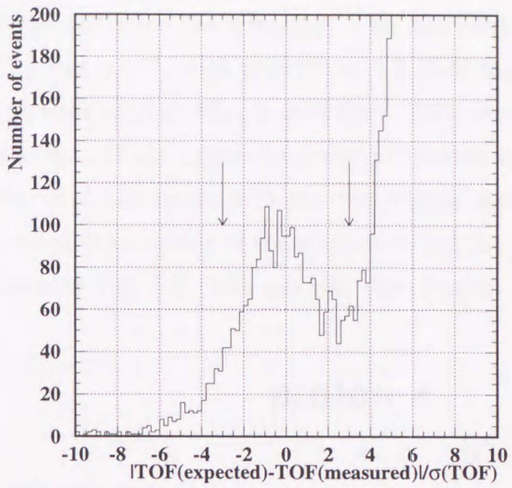

Figure 5.3: $|\mathrm{TOF}_{\mathrm{expected}} - \mathrm{TOF}_{\mathrm{measured}}|/\sigma_{\mathrm{TOF}}$ distribution. The arrows show the cut values $\pm$ 3 for the proton and antiproton identification.

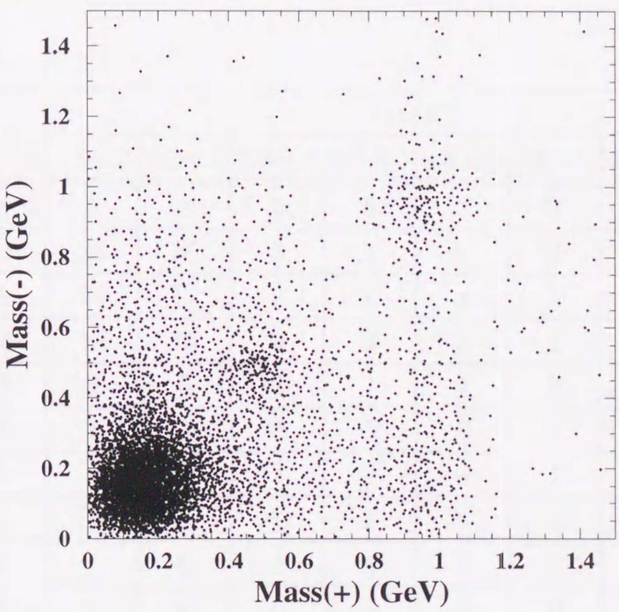

Figure 5.4: Scatter plot of the masses calculated from the TOF for the positively (abscissa) and negatively (ordinate) charged particles in the event samples before the identification.

5.2.4 Candidate events

A total of 311 events remained after the selection. The candidate events were divided into two-dimensional bins of $W_{\gamma\gamma}$ and $\cos\theta^*$, with a width of 0.1 GeV for $W_{\gamma\gamma} < 2.75$ GeV and 0.1 for $|\cos\theta^*|$. Wider $W_{\gamma\gamma}$ bins were used at $W_{\gamma\gamma} > 2.75$ GeV. The two-photon c.m. energy, $W_{\gamma\gamma}$, was calculated from the momenta of the proton and the antiproton after corrections for energy losses in the materials. We used the angle between the proton momentum and the electron beam direction in the photon-photon center-of-mass frame to be the scattering angle θ^* with a good approximation as shown in Fig. 5.5. The angular distribution of the candidate events is tabulated in Table 5.1

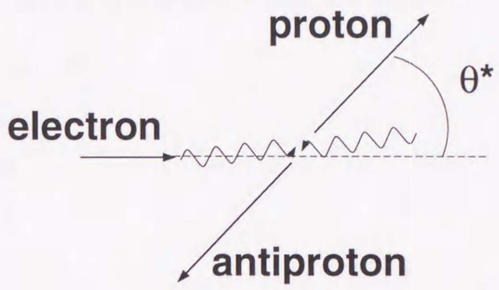

Figure 5.5: The definition of the scattering angle θ^*.

$W_{\gamma\gamma}$ (GeV)	$\lvert\cos\theta^*\rvert$									
	0.0-0.1	0.1-0.2	0.2-0.3	0.3-0.4	0.4-0.5	0.5-0.6	0.6-0.7	0.7-0.8	0.8-0.9	0.9-1.0
2.1	2	0	2	0	0	0	0	0	0	0
2.2	33	23	15	3	1	2	0	0	0	0
2.3	29	26	17	9	7	2	1	0	0	0
2.4	13	19	15	9	2	3	1	0	0	0
2.5	11	8	5	2	1	2	0	0	0	0
2.6	6	1	3	5	5	5	1	0	0	0
2.7	0	1	0	3	2	0	1	0	0	0
2.85	0	1	0	1	2	4	1	1	0	0
3.05	0	1	0	0	1	0	2	0	0	0
3.30	0	0	0	0	1	0	0	0	0	0

Table 5.1: Number of candidate events for $\gamma\gamma \to p\bar{p}$.

5.3 Selection of $e^+e^- \to (e^+e^-)K^0_S K^0_S$ events

After the standard track reconstruction was applied, we selected $e^+e^- \to e^+e^-\gamma\gamma \to (e^+e^-)K^0_S K^0_S$ events from the preselection sample. The K^0_S was identified with its decay into $\pi^+\pi^-$. We selected events which included 4 charged particles in the final state (candidates of $\pi^+\pi^-\pi^+\pi^-$).

5.3.1 Selection of four track events

The selection criteria of 4 track events were as follows:

1. $N_{\rm good} = 4$.
   $N_{\rm good}$ was defined as the number of good tracks which satisfied the following requirements,
   - $N_{\rm axial} \geq 8$, $N_{\rm stereo} \geq 4$,
   - $|R_{\rm min}| < 2.0$ cm,
   - $|Z_{\rm min}| < 10.0$ cm,
   - $|\cos\theta| < 0.8$ and
   - $p_t > 0.1$ GeV/c.

   In order to get low-$W_{\gamma\gamma}$ events, we set the lower limit of the transverse momentum at 0.1 GeV/c.
2. Net charge of good tracks = 0.
3. $\mathrm{Mass_{TOF}} < 400$ MeV/c^2.
   $\mathrm{Mass_{TOF}}$ was defined as the estimated mass from the TOF measurement as shown in Fig. 5.6. This requirement was applied only when a good track was connected to a TOF hit.

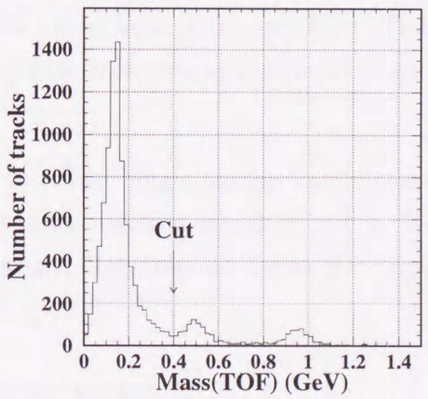

Figure 5.6: Mass distribution estimated from the TOF measurement for good tracks which were connected to a TOF hit.

5.3.2 Rejection of background events

Two of major sources of background, single photon annihilation events and non-exclusive production of $K^0_S K^0_S$-pairs, contaminated to the event samples. In order to reduce these events, we applied the following requirements for the sample of 4-track events:

1. $E_{\rm total} \leq 3.0$ GeV.
   $E_{\rm total}$ was defined as the total cluster energy in LG and LA.

2. $N_{\rm other} = 0$.
   $N_{\rm other}$ was defined as the number of other tracks which came from the collision point and satisfied the following requirements,

   - 3-dimensional track reconstruction,
   - $|R_{\rm min}| < 2.0$ cm and
   - $|Z_{\rm min}| < 20.0$ cm.

3. $N_{\rm neutral\ cluster} = 0$.
   $N_{\rm neutral\ cluster}$ was defined as the number of the neutral clusters, where the neutral cluster means a cluster in LG without a connected good track. The neutral cluster must satisfy the following requirements:

$$E_{\rm cluster} > 200{\rm MeV} \quad \text{and}$$
$$|\cos\theta_{\rm LG,track}| < 0.9, \tag{5.2}$$

   where $E_{\rm cluster}$ was the deposited cluster energy and $\theta_{\rm LG,track}$ was the angle between the LG cluster center position and the position on the LG surface to which the good track was extrapolated.

4. $|\sum \vec{p}_t| < 0.2$ GeV/c.
   $|\sum \vec{p}_t|$ was defined as the vector sum of the two K^0_S's. The K^0_S momentum was calculated from the sum of the two track momenta at the vertex position as described in the following subsection.

Requirement 1 was effective to reduce single photon annihilation process events. Non-exclusive events were effectively rejected by requirements 2, 3 and 4. Requirement 3 rejected $e^+e^- \to e^+e^-X + n\gamma$ $(n = 1, 2, ...)$ events. Requirement 4 was also applied to restrict the virtuality of colliding photons.

5.3.3 Search for K^0_S decay vertex

To determine the $\pi^+\pi^-$ combinations from 4 charged-pions and the K^0_S decay length, a searching routine of $K^0_S \to \pi^+\pi^-$ vertices (secondary vertex) was applied to the 4-track event

sample. The $K^0_S \to \pi^+\pi^-$ vertex was determined by the minimum χ^2 method. The χ^2 is defined as

$$\chi^2 = \left(\frac{\mathrm{d}r}{\sigma_r}\right)^2 + \left(\frac{\mathrm{d}z}{\sigma_z}\right)^2, \tag{5.3}$$

where $\mathrm{d}r$ is the closest approach to the secondary vertex in the r-ϕ plane and the $\mathrm{d}z$ is z coordinate there as shown in Fig. 5.7. σ_r and σ_z are standard deviations for $\mathrm{d}r$ and $\mathrm{d}z$, respectively. Figure 5.8 shows the invariant mass dependence of the standard deviations for $\mathrm{d}r$ and $\mathrm{d}z$, which were evaluated by $e^+e^- \to e^+e^- K^0_S K^0_S$ Monte Carlo events. Although these standard deviations depend on the properties of the tracks and determined mainly by multiple scattering in CDC, we used the constant values for all the event samples, $\sigma_r = 0.33$ cm and $\sigma_z = 1.28$ cm, expected values at $W_{\gamma\gamma} = 1.5$ GeV. The position-determination uncertainty caused by the constant standard deviations was negligible in the present analysis.

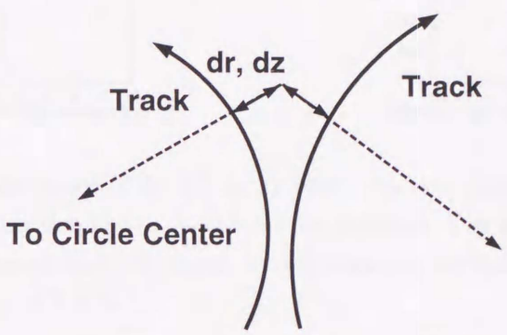

Figure 5.7: Schematic view of $\mathrm{d}r$ and $\mathrm{d}z$.

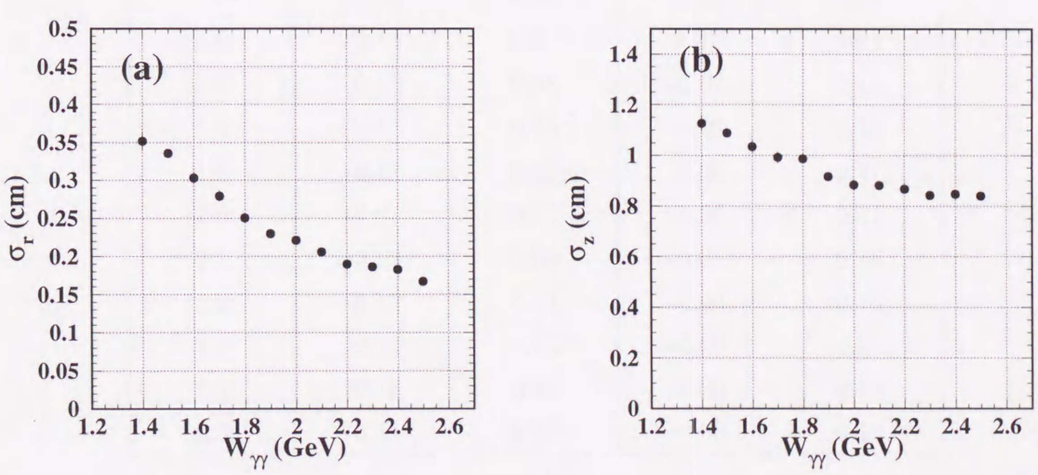

Figure 5.8: The two-photon invariant mass ($W_{\gamma\gamma}$) dependence of (a) σ_r and (b) σ_z. These values were estimated by $e^+e^- \to e^+e^- K^0_S K^0_S$ MC events.

Figure 5.9 shows the position deviation of the K^0_S decay vertex for (a) the K^0_S direction and (b) the perpendicular direction evaluated by the MC simulation at $W_{\gamma\gamma} = 1.5$ GeV. Fitting these distributions with Gaussian curves, we found a secondary vertex resolution for the several $W_{\gamma\gamma}$ values in Table 5.2. The correct K^0_S direction and decay vertex position are given from the MC information at the generation stage. By using the minimum χ^2 method we achieved a secondary vertex resolution of about 0.65 cm along the K^0_S direction.

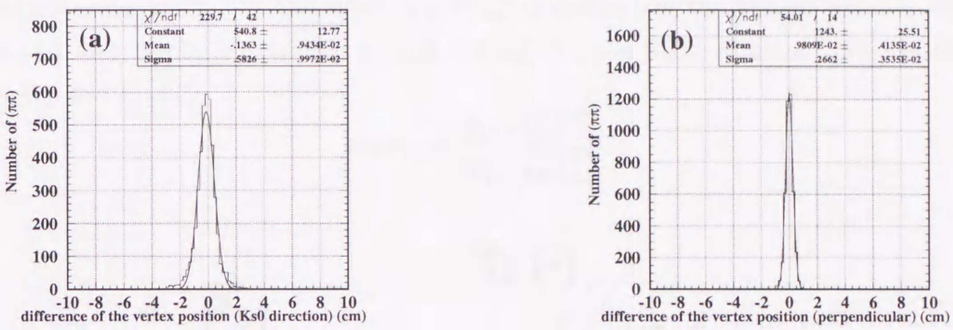

Figure 5.9: The difference of the K^0_S decay vertex position distribution for (a) the K^0_S direction and (b) perpendicular direction. The curves show the fits by Gaussian distributions, having standard deviations of (a) 5.8 mm and (b) 2.7 mm.

	K^0_S direction		perpendicular direction	
$W_{\gamma\gamma}$ (GeV)	Mean (cm)	Sigma (cm)	Mean (cm)	Sigma (cm)
1.5	-0.14	0.58	-0.01	0.25
1.6	-0.15	0.61	0.01	0.21
1.7	-0.11	0.58	-0.02	0.20
1.8	-0.11	0.65	-0.03	0.18
1.9	-0.11	0.61	-0.00	0.17
2.0	-0.07	0.63	-0.00	0.17
2.1	-0.13	0.63	-0.00	0.16
2.2	-0.13	0.64	-0.00	0.15
2.3	-0.11	0.65	-0.00	0.14
2.4	-0.12	0.66	-0.00	0.13
2.5	-0.11	0.65	-0.00	0.12

Table 5.2: K^0_S decay vertex resolution. These values are results from the fit with a Gaussian curve of the difference distribution for the K^0_S decay vertex evaluated by Monte Carlo events.

Among the two possible combinations of oppositely charged pion pairs $((\pi^+_1\pi^-_2)(\pi^+_3\pi^-_4)$ or $(\pi^+_1\pi^-_4)(\pi^+_3\pi^-_2))$, the correct combination was selected by using the flight direction of each K^0_S candidate.

The flight direction was defined as the angle between the composite momentum direction and the line between the vertices in the r-ϕ plane as shown in Fig. 5.10. The composite momentum was calculated from the sum of the two track momenta at each vertex. Figure 5.10 gives an example to illustrate the flight direction: when $\vec{p}_{12}$ is defined as the momentum sum of the track$_1(+)$ and track$_2(-)$ and when V_{12} (V_{34}) is defined as the vertex position composed of track$_1(+)$ and track$_2(-)$ (track$_3(+)$ and track$_4(-)$), the flight direction (θ_{12}) is the angle between $\vec{p}_{12}$ and $\overrightarrow{V_{34}V_{12}}$:

$$\cos\theta_{12} = \frac{\vec{p}_{12} \cdot \overrightarrow{V_{34}V_{12}}}{|\vec{p}_{12}||\overrightarrow{V_{34}V_{12}}|}. \tag{5.4}$$

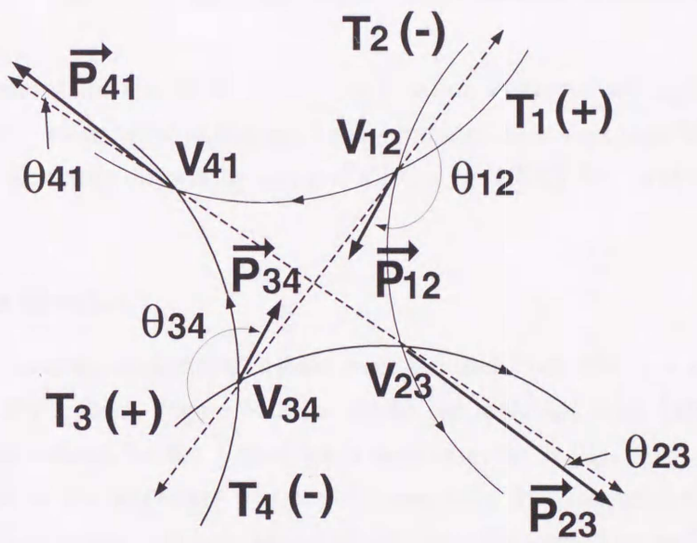

Figure 5.10: Schematic view of the flight direction. In this figure, $T_i(+/-)$ represents the track i and V_{ij} and $\vec{p}_{ij}$ represent the vertex position and the sum of the two track momenta composed by tracks i and j, respectively. θ_{ij} represents the angle between the $\vec{p}_{ij}$ and the line connecting the two vertices.

The scatter plot of two flight directions ($\cos\theta$) in the each combination is shown in Fig 5.11. Figure 5.11 (a) shows all combinations for the 4-track data sample (θ_{12}-θ_{34} and θ_{41}-θ_{23} in Fig. 5.10) and Fig. 5.11 (b) shows the flight direction of the correct combination (θ_{41}-θ_{23} in Fig. 5.10) for the $e^+e^- \to e^+e^-K^0_S K^0_S$ Monte Carlo events at $W_{\gamma\gamma} = 1.5$ GeV separated from those of wrong combinations.

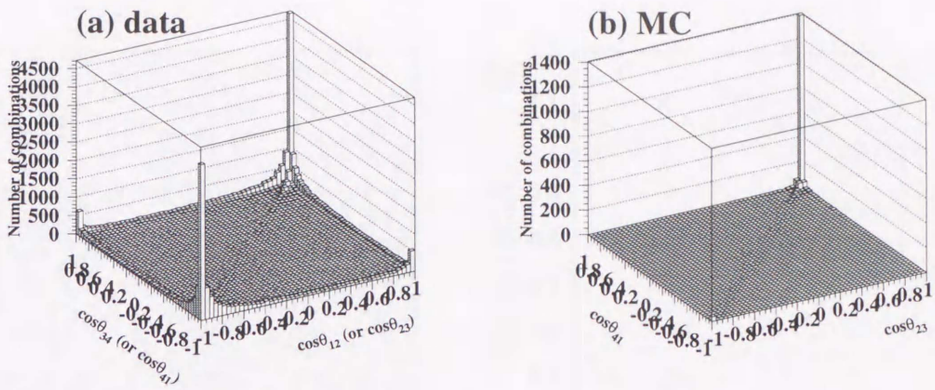

Figure 5.11: The scatter plot of the flight direction: (a) all combinations for the 4-track data sample and (b) correct combination of the MC data.

The correct combination was chosen as the combination with smallest angle (θ_{41} in Fig. 5.10). In this method the combinatorial background was estimated to be less than 0.1 % for the events passed through all selection criteria by using $e^+e^- \to e^+e^-K^0_SK^0_S$ MC events, even in the low-$W_{\gamma\gamma}$ region.

5.3.4 K^0_S identification

Most of the remaining background events were induced from $e^+e^- \to e^+e^-\rho^0\rho^0$ in which ρ^0s decayed into $\pi^+\pi^-$ pairs. Figure 5.12 (a) shows the invariant mass ($M_{\pi^+\pi^-}$) distribution of the correct combinations for the 4 good track data sample. $M_{\pi^+\pi^-}$ was calculated from the two track momenta at the secondary vertex point assuming the pion mass for both tracks. To eliminate this contamination, we took advantage of the finite mean free path ($c\tau$ = 2.7 cm) of the K^0_S. The two secondary vertices were required to satisfy the condition

- (decay length)$_{2-\mathrm{dim.}} > 0.4$ cm,

where the decay length was defined as the distance between the beam interaction point and the secondary vertex in the r-ϕ plane.

The beam interaction point (two-photon interaction point) were measured by using Bhabha scattering data sample. The estimated mean interaction point is plotted in Fig. 5.13 as a function of the experimental run number taken by the VENUS detector. There are some variations of both x- and y-coordinate of the interaction points. The detailed study for the CDC data indicates that these fluctuations were caused by the changes of beam condition [62]. After the decay length cut was applied, the scatter plot of the $M_{\pi^+\pi^-}$ is shown in Fig. 5.12 (b). K^0_S-pairs were clearly separated from $\rho^0\rho^0$ pairs.

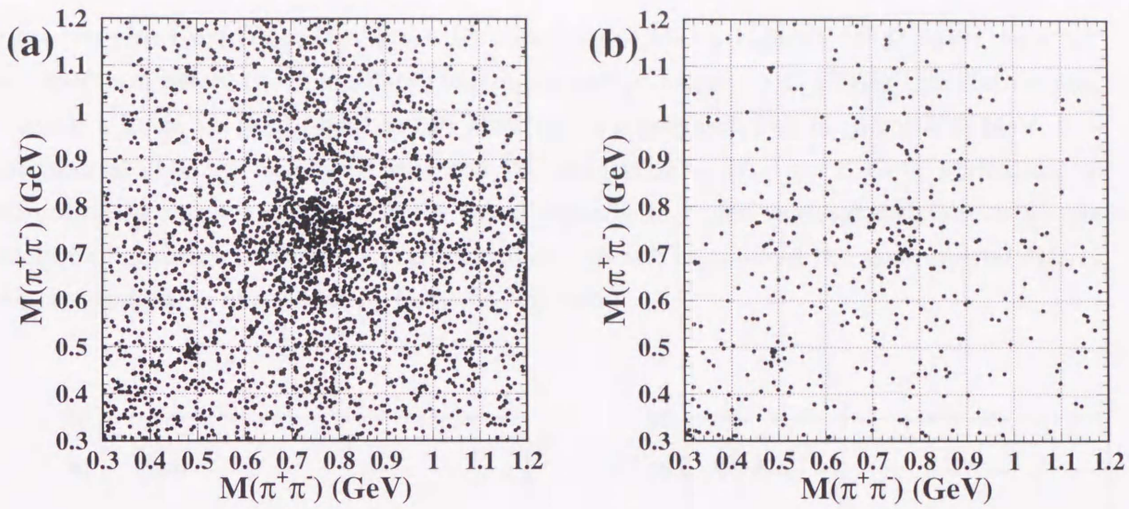

Figure 5.12: Scatter plot of the invariant mass calculated from the two track momenta at the secondary vertex point assuming the pion mass for both tracks: (a) for the 4 track data sample and (b) after the decay length cut.

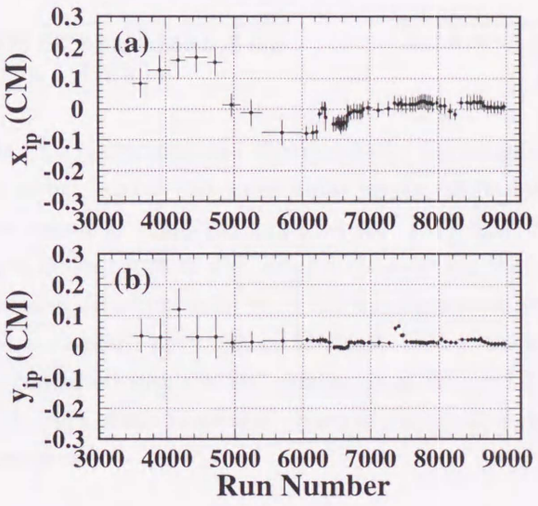

Figure 5.13: The mean interaction point as function of the experimental run number measured by using Bhabha event sample: (a) the x-coordinate and (b) the y-coordinate of the interaction points. The error bar shows the standard deviation.

Finally we required that candidate events for two-photon produced $K^0_S K^0_S$ pairs must satisfy the condition

- $|M_{K^0_S} - M_{\pi^+\pi^-}| < 20$ MeV/c^2

for the two pion pairs. Here $M_{K^0_S}$ is the K^0_S mass (497.67 MeV). Figure 5.14 (a) shows the $\pi^+\pi^-$ mass spectrum before the 4 mm decay length cut and pt-balance cut. Fitting this distribution, we found a mean value of (490.1 $\pm$ 1.0) MeV and a mass resolution of (6.9 $\pm$ 1.3) MeV. The experimental data was compared with the MC simulation at $W_{\gamma\gamma}$ = 1.5 GeV, normalized to the sum of the number of events in the signal region with added constant distribution for the background as shown in Fig. 5.14 (b). The simulation well reproduced the experimental data in both the peak value and deviation from the K^0_S mass.

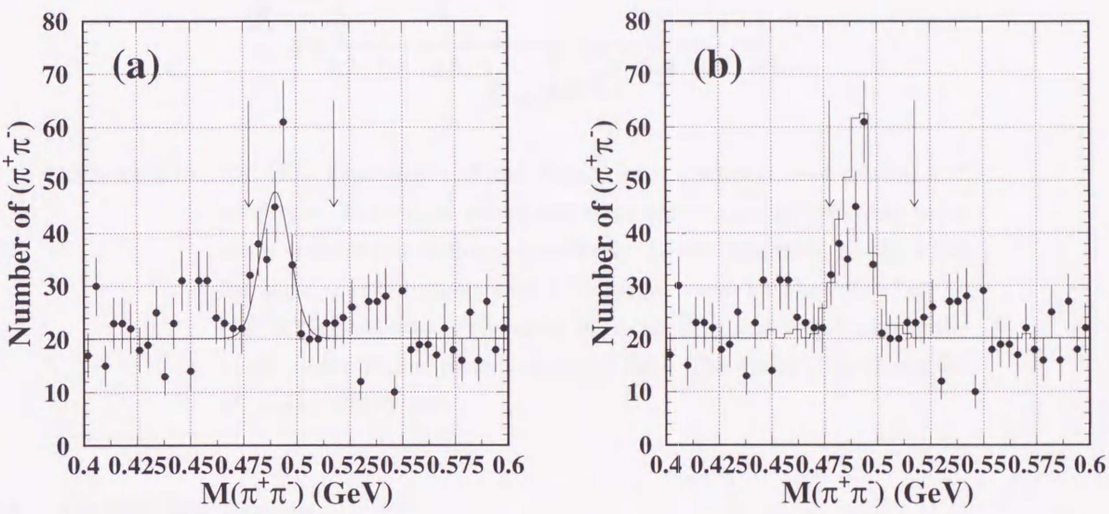

Figure 5.14: The $\pi^+\pi^-$ invariant mass distribution for the experimental data before the pt-balance cut and 4 mm decay length cut (points with error bar). The arrows indicate the signal region ($M_{K^0_S} \pm 20$ MeV). In (a), the curve is the result of a fit using a constant for the background and a Gaussian distribution for the peak, having a mean value of 490.1 MeV and a standard deviation of 6.9 MeV. In (b), the experimental data are compared with the MC simulation at $W_{\gamma\gamma}$ = 1.5 GeV, normalized to the sum of the number of events in the signal region and a constant (histogram).

Figure 5.15 shows the $W_{\gamma\gamma}$ dependence of the $M_{\pi^+\pi^-}$ mean value and resolution. It was estimated by the fit of the $M_{\pi^+\pi^-}$ distributions with a Gaussian curve for the MC data without the $M_{\pi^+\pi^-}$ cut. The mean values were lower than the K^0_S mass by about 4-7 MeV and increased slightly with increasing $W_{\gamma\gamma}$, because of the effects of energy losses in the detector materials. $M_{\pi^+\pi^-}$ resolutions were almost constant and were about 7-8 MeV as indicated in the figure.

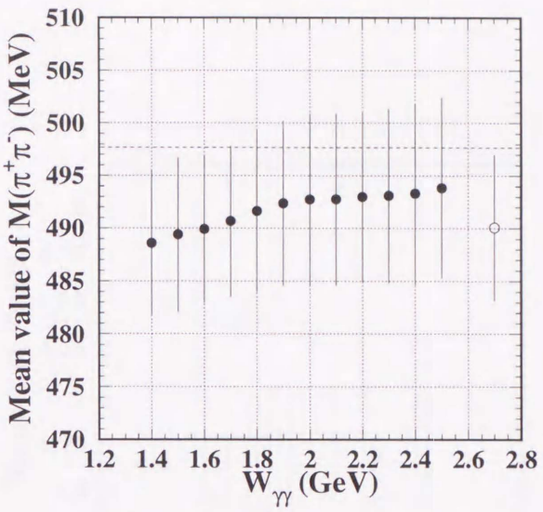

Figure 5.15: The $W_{\gamma\gamma}$ dependence of the $M_{\pi^+\pi^-}$ mean value (closed circles) and resolution. The center values and error bars represent the mean value and a standard deviation, respectively. It was estimated by the fit of the $M_{\pi^+\pi^-}$ distributions with a Gaussian curve for the MC $e^+e^- \to e^+e^-K^0_SK^0_S$ reaction. The open circle at $W_{\gamma\gamma} = 2.7$ GeV shows the results of the fit for the experimental data. The dashed line shows the K^0_S mass (497.67 MeV).

5.3.5 Candidate events

With these selection criteria, 11 events remained in the final data sample. The $K^0_SK^0_S$ invariant mass ($W_{K^0_SK^0_S}$) spectrum is shown in Fig. 5.16. $W_{K^0_SK^0_S}$ was calculated from the mass (497.67 MeV) and momenta of the K^0_S where the K^0_S momentum was calculated from the sum of two track momenta at the vertices. In the $f'_2(1525)$ mass region 3 events were found and 8 events were in the higher mass region (that of $f_J(1710), X(1800), f_J(2210)$). The angular distribution of the candidate events is tabulated in Table 5.3.

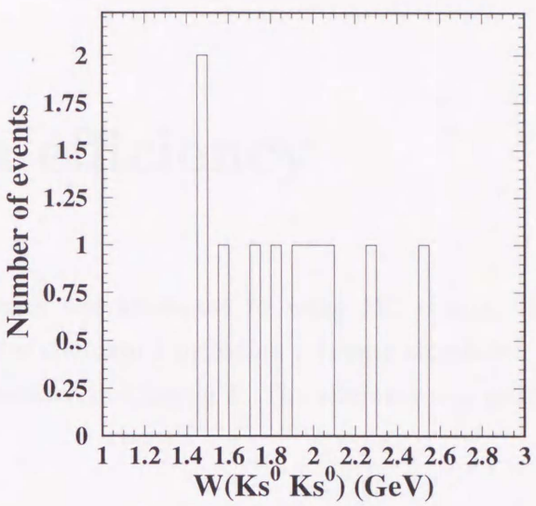

Figure 5.16: $K^0_S K^0_S$ invariant mass spectrum for the candidate events.

W	0.0-0.1	0.1-0.2	0.2-0.3	0.3-0.4	0.4-0.5	0.5-0.6	0.6-0.7	0.7-0.8	0.8-0.9	0.9-1.0
1.4-1.6	0	0	2	0	0	1	0	0	0	0
1.6-1.8	0	0	0	1	0	0	0	0	0	0
1.8-2.0	0	1	1	1	0	0	0	0	0	0
2.0-2.2	0	0	0	1	0	0	1	0	0	0
2.2-2.4	0	0	0	0	1	0	0	0	0	0
2.4-2.6	0	1	0	0	0	0	0	0	0	0

Table 5.3: The angular distribution of the $\gamma\gamma \to K^0_S K^0_S$ candidate events.

Chapter 6

Detection efficiency

The detection efficiency was estimated by using MC events. The generated events were passed through a detector simulation including a trigger simulation and the same selection as that in the real data described in Chapter 5. The efficiency was estimated in each $W_{\gamma\gamma}$-$|\cos\theta^*|$ bin.

6.1 $e^+e^- \to e^+e^-p\bar{p}$

To obtain the detection efficiency for the reaction $e^+e^- \to e^+e^-p\bar{p}$, we generated 10,000 MC events for each $W_{\gamma\gamma}$ bin in the range from 2.2 to 3.3 GeV with a width of 0.1 GeV and a uniform $|\cos\theta^*|$ distribution.

The detection efficiency obtained from the simulation is plotted in Fig. 6.1. The maximum detection efficiency estimated is about 10% at $W_{\gamma\gamma}$ around 2.6 GeV in the angular region of $|\cos\theta^*| \leq 0.3$. The efficiency gradually decreases in larger $|\cos\theta^*|$ bins, due to the limited angular acceptance at each $W_{\gamma\gamma}$ bin. The fall-off at smaller $W_{\gamma\gamma}$ is mainly brought by the track-finding efficiency in the event trigger. The efficiency at large energies, $W_{\gamma\gamma} > 2.7$ GeV, is limited by the particle identification efficiency. The estimated efficiency is about 2.5% in the largest $W_{\gamma\gamma}$ bin, $3.25 < W_{\gamma\gamma} < 3.35$ GeV, at $|\cos\theta^*| < 0.3$. The large-angle nuclear scattering and the absorption of antiprotons are also significant. About 30% of the events were estimated to be lost by these interactions.

The systematic error of the efficiency was estimated from ambiguities in the dominant source of the inefficiency. The uncertainty in the TF efficiency, which was estimated by comparing the response of TF to low-energy multi-track events with the simulation, corresponds to an efficiency error of 5% at $W_{\gamma\gamma}$ =2.2 GeV. Among the uncertainties in the nuclear interaction simulation, the largest is due to the uncertainty in antiproton absorption. The corresponding efficiency error was estimated by comparing the simulation results with those from another hadronic interaction simulation program, FLUKA [61], to be 7% in all bins. The uncertainty from the particle identification was studied by varying the identification criteria. The corresponding error

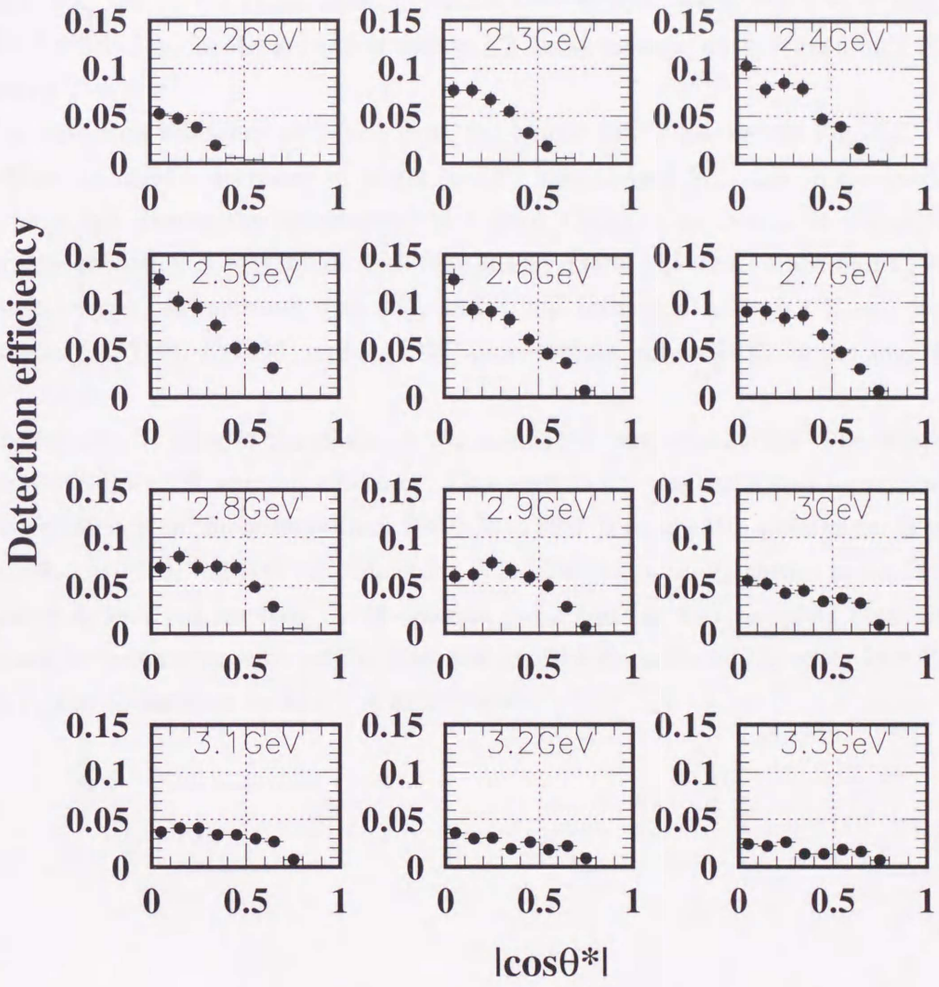

Figure 6.1: Angular dependence of the detector efficiency for the reaction $e^+e^- \to e^+e^-p\bar{p}$ at each $W_{\gamma\gamma}$ bin. Only statistical errors are included.

in the detection efficiency was found to be 10% at $W_{\gamma\gamma} = 2.7$ GeV, and to increase up to 14% at 3.05 GeV.

6.2 $e^+e^- \to e^+e^-K^0_SK^0_S$

To estimate the detection efficiency for the reaction, $e^+e^- \to e^+e^-K^0_SK^0_S$, we generated 500,000 MC events for each $W_{\gamma\gamma}$ bin in the range from 1.5 to 2.0 GeV and 100,000 MC events for each $W_{\gamma\gamma}$ bin in the range from 2.1 to 2.5 GeV with a width of 0.1 GeV and a uniform $|\cos\theta^*|$ distribution. In the generated events K^0_S decay mode is not included only $K^0_S \to \pi^+\pi^-$ but also $K^0_S \to \pi^0\pi^0$.

The detection efficiency obtained from the simulation is plotted in Fig. 6.2. The detection efficiency rapidly decreases in larger $|\cos\theta^*|$ bins at each $W_{\gamma\gamma}$ due to the limited angular acceptance and due to the requirement of 4 good tracks in an event. In the $f'_2(1525)$ mass region, the efficiency is very small (less than 0.1%) due to the small track-finding efficiency in the event trigger. It increases with $W_{\gamma\gamma}$ and it was estimated to be 0.4 %, 0.7 % and 2.0 % around the $f_J(1710)$, $X(1800)$ and $f_J(2220)$ mass regions, respectively, in the angular region of $|\cos\theta^*| < 0.3$.

The systematic error of the efficiency was estimated from ambiguities. The trigger efficiency depended on the CDC wire-hit efficiency. This uncertainty was estimated by varying the CDC wire-hit efficiency on the average from 100.0 % to 99.3 % in the MC simulation. It was 10 % $\sim$ 4 % at $W_{\gamma\gamma} = 1.4 \sim 2.5$ GeV, in this order. The systematic uncertainties in the interaction of the materials inserted between the interaction point and the first sampling point of CDC was estimated by comparing with results from the another simulation [61], to be 21.3 % at $W_{\gamma\gamma} =$ 1.5 GeV, and to increase up to 8.1 % at 2.5 GeV.

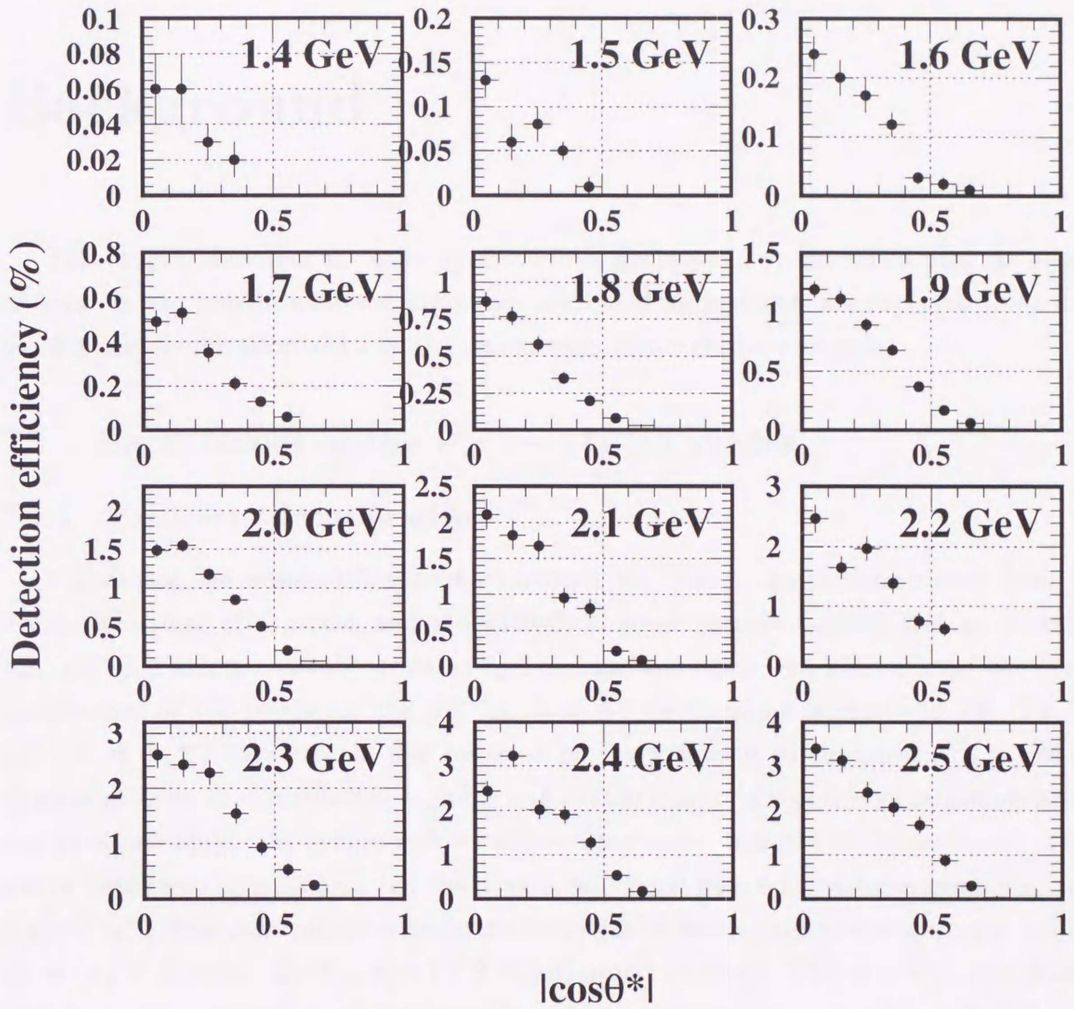

Figure 6.2: Angular dependence of the detector efficiency for the reaction $e^+e^- \to e^+e^-K^0_SK^0_S$ at each $W_{\gamma\gamma}$ bin. Only statistical errors are included.

Chapter 7

Background

This chapter describes the contamination from background events which pass the selection criteria. In the present analyses, the major sources of backgrounds are expected to be due to particle misidentification and contaminations from non-exclusive processes.

7.1 Background of the $e^+e^- \to e^+e^-p\bar{p}$ events

7.1.1 Particle misidentification

Concerning the misidentification background, the largest contribution comes from those events consisting of a proton and a negatively charged particle misidentified as an antiproton (pX^-). Those are mainly produced by beam-gas and beam-wall interactions. The z-vertex distribution of the tracks for the $pX^-(X = \pi, K)$ data sample is shown in Fig. 7.1. The $pX^-(X = \pi, K)$ data sample was collected by the following requirements: (i) a positively charged particle was identified as a proton and (ii) the mass of a negatively charged particle was less than 600 MeV. The events with wrong z-vertex values indicate unphysical events (beam-gas or beam-wall interactions) and the peak is associated with non-exclusive reactions, such as $p(\bar{p})(\pi^+)\pi^-$. The contamination from the beam-gas or beam-pipe interactions was estimated to be (3±3) % in all the $W_{\gamma\gamma}$ bins ((9.3 ± 9.3) events in total). This was estimated from the z-vertex distribution of $p\bar{p}$ candidates. The number of events selected with a tight $|Z_{\rm min}|$ cuts from the $e^+e^- \to e^+e^-p\bar{p}$ candidates is shown as a function of the $|Z_{\rm min}|$ cut in Fig. 7.2. The small increase with increasing $Z_{\rm min}$ cut is due to beam-gas background events.

Events from meson-pair production, $\gamma\gamma \to \pi^+\pi^-$ and $\gamma\gamma \to K^+K^-$, can contaminate the true events if both tracks are misidentified. The contamination was estimated to be (2 ± 2) % ((0.18 ± 0.18) events in total) in the high energy region, $W_{\gamma\gamma} > 2.9$ GeV, by extrapolating the measured mass distribution of identified meson pair events to the proton mass region. Figure 7.3 shows the measured mass distribution in which the measured mass difference of the two tracks is less than 0.2 GeV/c^2. The background from the $\pi^+\pi^-$ and K^+K^- production events is fitted by exponential curves to obtain the expectation value.

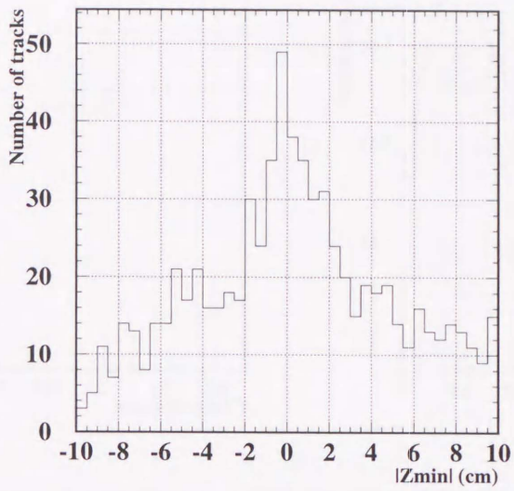

Figure 7.1: $Z_{\min}$ distribution for the $p^+X^-(X = \pi, K)$ data sample. The mass of a negatively charged particle (X^-) is required to be less than 600 MeV.

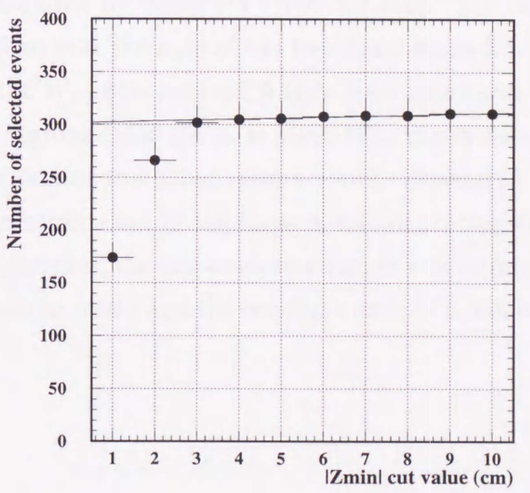

Figure 7.2: Number of events selected by the various $|Z_{\min}|$ cut. The solid line is the result of a fit using a one-order polynomial in the range of 5.0 cm $< |Z_{\min}| <$10.0 cm.

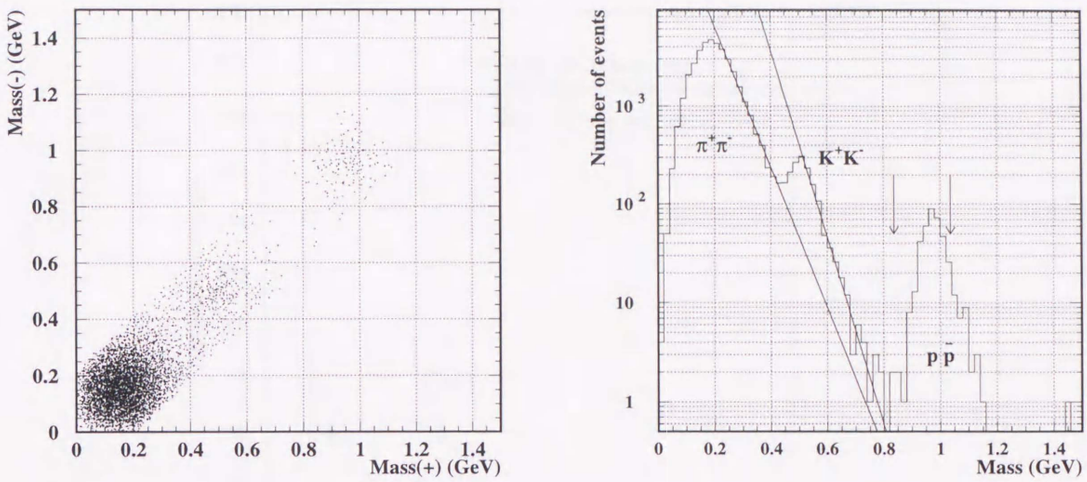

Figure 7.3: The mass distribution in which the mass difference is less than 0.2 GeV/c^2.

7.1.2 Events from non-exclusive processes

The contamination of events from non-exclusive processes, $\gamma\gamma \to p\bar{p} + X$'s in which X's were undetected, was estimated in each $W_{\gamma\gamma}$ bin, by comparing the p_t-imbalance distribution of the real data with the simulation data of the $\gamma\gamma \to p\bar{p}$ and $\gamma\gamma \to p\bar{p} + X$'s reactions. The reaction, $\gamma\gamma \to p\bar{p} + X$'s, was simulated by using PYTHIA 5.7 [59]. The normalization of these MC processes was determined so that the sum of the two simulations fits the observed p_t-imbalance distribution. In the fit, the $W_{\gamma\gamma}$ bins above 2.6 GeV were combined because the statistics was poor and because the background did not have steep $W_{\gamma\gamma}$ dependence in this region.

Figure 7.4 shows the sum of the fitted results which, illustrated with the solid histogram, well reproduces the observation, even in the large p_t-imbalance region above the cut. From the fit obtained, the contamination of the non-exclusive events was estimated to be $(8 \pm 3)\%$ on the average ((24.9 ± 9.3) events in total) and the results in each $W_{\gamma\gamma}$ bin is summarized in Table 7.1.

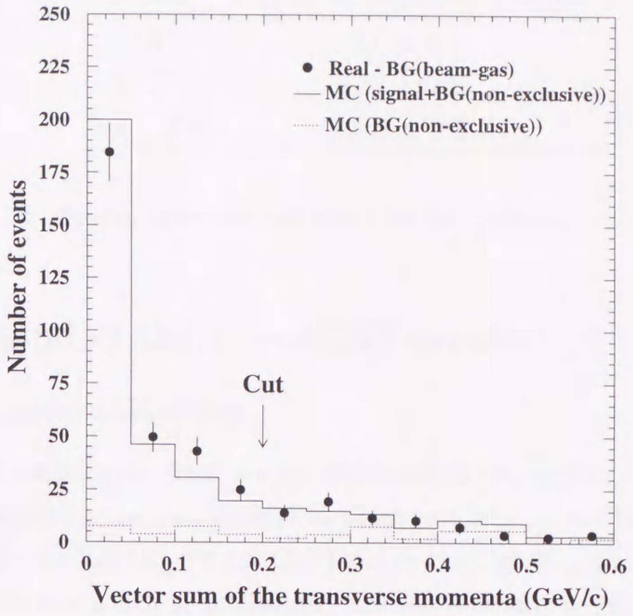

Figure 7.4: $|\sum \vec{pt}|$ distribution of the candidate events after subtraction of the backgrounds from beam-gas/wall events. The dots with error bars are the experimental data, and the solid histogram is the sum of the MC data of $\gamma\gamma \to p\bar{p}$ and $\gamma\gamma \to p\bar{p}X$'s normalized by fitting the experimental data. The dashed histgram is the estimated contribution from $\gamma\gamma \to p\bar{p}X$'s

$W_{\gamma\gamma}$ (GeV)	Background (%)
2.2	4.9 ± 2.3
2.3	5.8 ± 4.0
2.4	4.8 ± 4.4
2.5	29.2 ± 10.3
2.6-3.3	36.5 ± 12.5
Average	7.8 ± 3.0

Table 7.1: The contamination of the non-exclusive processes.

7.1.3 Summary

The estimated background events are summarized in Table 7.2. Note that the contamination from non-exclusive events in which either proton or antiproton was misidentified is also included in the last estimation, although their contribution is negligibly small.

Source	Number of background events
p^+X^-	9.3 ± 9.3
X^+X^-	0.18 ± 0.18
$p\bar{p} + X$'s	24.9 ± 9.3

Table 7.2: Number of background events for the reaction $e^+e^- \to e^+e^-p\bar{p}$.

7.2 Background of the $\gamma\gamma \to K^0_S K^0_S$ events

7.2.1 Particle misidentification

The background contribution from one K^0_S misidentification, such as $e^+e^- \to e^+e^-K^0_S K^\pm\pi^\mp$, was estimated by studying the data sample in which one $M_{\pi^+\pi^-}$ was taken within $\pm$ 20 MeV from the K^0_S mass in the low-$W_{\gamma\gamma}$ (< 1.8 GeV) and in the high-$W_{\gamma\gamma}$ (> 1.8 GeV) regions. The other $M_{\pi^+\pi^-}$ distribution which is not identify the K^0_S is shown in Fig. 7.5. The background was fitted by a constant in the mass region of $0.56 < M_{\pi^+\pi^-} < 1.0$ GeV. This contamination was estimated to be (1.7 ± 0.4) events in total from the result of the best fit.

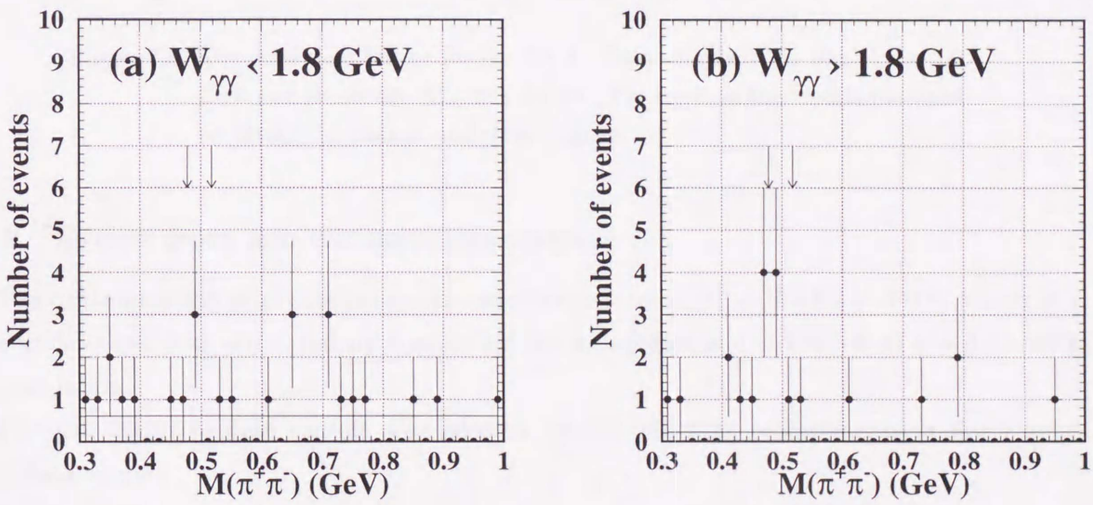

Figure 7.5: $M(X^0)$ distribution for the $K^0_S X^0$ data sample (a) in the $W_{\gamma\gamma} < 1.8$ GeV and (b) in the $W_{\gamma\gamma} > 1.8$ GeV. The solid line is the result obtained by fitting the data with a constant in the background mass region.

The background due to misidentified K^0_S pairs, such as $\gamma\gamma \to \rho^0\rho^0 \to 4\pi$, and mis-matched $\pi^+\pi^-$ pairs, was estimated by using the event sample in which a $\pi^+\pi^-$ invariant mass difference was less than 40 MeV/c^2. The distributions of $M_{\pi^+\pi^-}$ for these events are shown in Fig. 7.6

in the low-$W_{\gamma\gamma}$ region (< 1.8 GeV) and in the high-$W_{\gamma\gamma}$ region (> 1.8 GeV). The background was fitted by an exponential curve in the mass region of $0.32 < M(\pi^+\pi^-) < 0.44$ GeV/c^2 and by a Bright-Wigner distribution in the ρ^0 meson region ($0.56 < M(\pi^+\pi^-) < 1.00$ GeV/c^2) in the low-$W_{\gamma\gamma}$ region. In the high-$W_{\gamma\gamma}$ region the background was fitted by a constant in the mass region of $0.32\ M(\pi^+\pi^-) < 0.44$ GeV/c^2. From the result of fitting, the contamination was estimated to be (1.1 ± 0.4) events in total.

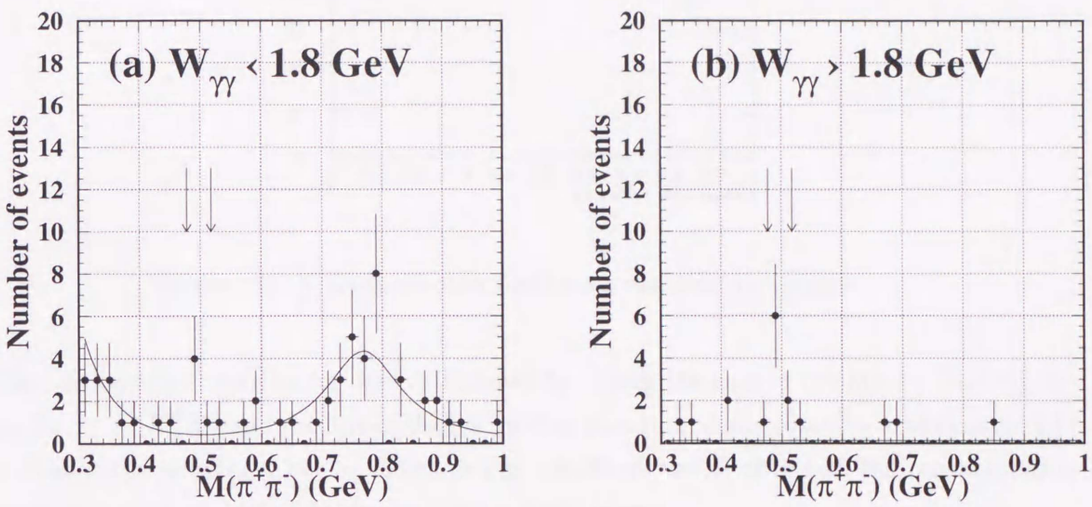

Figure 7.6: The mass distribution for the X^+X^- data sample (a) in the $W_{\gamma\gamma} < 1.8$ GeV and (b) in the $W_{\gamma\gamma} > 1.8$ GeV. The curve is the results obtained by fitting the background mass regions.

7.2.2 Events from non-exclusive processes

The contamination of events from non-exclusive processes, $\gamma\gamma \to K^0_S K^0_S + X$'s in which X's were undetected, was estimated by comparing the p_t-imbalance distribution of the data with the simulation.

The non-exclusive data sample was selected by the following requirements in the 4 good track data sample:

1. $E_{\rm total} \leq 3.0$ GeV and
2. $N_{\rm other} \geq 1$,

where $E_{\rm total}$ and $N_{\rm other}$ were the total cluster energy and the number of other tracks, respectively, as described in subsection 5.3.2. Figure 7.7 shows the p_t vector sum distribution for the non-exclusive process data sample. The p_t vector sum was calculated from the momenta of the 4 good tracks at the secondary vertex point. As shown in this figure, a background contribution does not have peak at zero as expected.

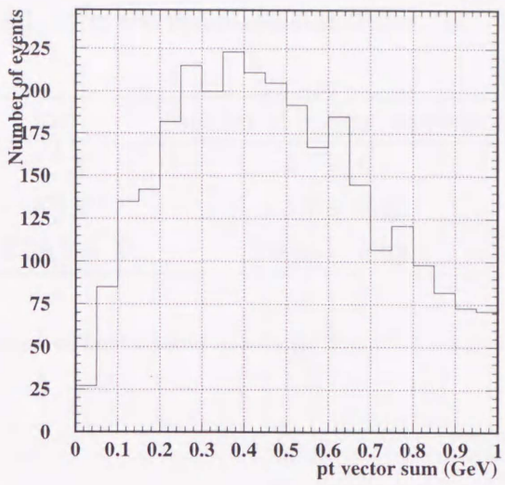

Figure 7.7: $|\sum \vec{p_t}|$ distribution for the non-exclusive data sample.

This background contribution was determined by fitting the sum of the Monte Carlo distribution for $\gamma\gamma \to K_S^0 K_S^0$ and the non-exclusive process data sample distribution to the candidates data without the p_t balance cut as shown in Fig. 7.8. From the fit obtained, the contamination of this background was estimated to be (0.04 ± 0.03) events.

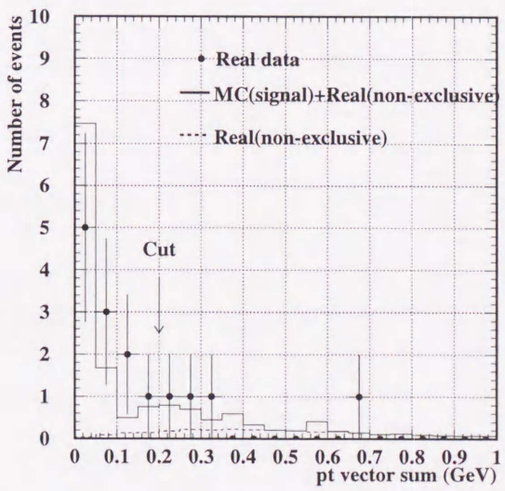

Figure 7.8: $|\sum \vec{p_t}|$ distribution of the candidate events. The dots with error bars are the experimental data. The solid histgram is the sum of the MC data for the $\gamma\gamma \to K_S^0 K_S^0$ reaction and the non-exclusive data sample. The dashed histgram is the estimated contribution from $\gamma\gamma \to K_S^0 K_S^0 X's$.

7.2.3 Summary

The background contamination was summarized in Table 7.3.

Source	Number of background events
X^+X^-	1.1 ± 0.4
$K^0_S X^0$	1.7 ± 0.4
$K^0_S K^0_S + X$	0.04 ± 0.03

Table 7.3: Number of background events for the $e^+e^- \to e^+e^- K^0_S K^0_S$ events.

Chapter 8

Results

In this chapter, we present the measured cross sections of the reactions, $\gamma\gamma \to p\bar{p}$ and $\gamma\gamma \to K^0\bar{K}^0$. The cross section for the two-photon production was evaluated by using the analysis results described in Chapters 5, 6 and 7 and the two-photon luminosity function. The first section describes the two-photon luminosity function. The second section is devoted to the measurement of the cross section. The obtained cross section is compared with those obtained by other groups and with various models.

8.1 Two-photon luminosity function

The obtained event distribution was converted to the cross section for the two-photon collision process ($\sigma_{\gamma\gamma\to X}$), by using the so-called two-photon luminosity function, $L_{\gamma\gamma}(W_{\gamma\gamma})$,

$$\sigma_{e^+e^-\to e^+e^-X} = L_{\gamma\gamma}(W_{\gamma\gamma}) \cdot \sigma(W_{\gamma\gamma})_{\gamma\gamma\to X} \cdot \mathrm{d}W_{\gamma\gamma}. \tag{8.1}$$

The luminosity function is defined as

$$L_{\gamma\gamma}(\tilde{s}) = \int f_{\gamma/e}(y, Q^2_{\max}) \cdot f_{\gamma/e}(z, Q^2_{\max}) \cdot \frac{\partial(y,z)}{\partial(\tilde{r},\tilde{s})} \mathrm{d}\tilde{r}, \tag{8.2}$$

where $f_{\gamma/e}(z, Q^2_{\max})$ is the total number of photons radiated from the beam electron/positron in a certain mass interval of the photon, $Q^2 < Q^2_{\max}$. The scaling variables y and z are defined as

$$y = \frac{E_{\gamma,1}}{E_{\mathrm{beam}}}, \quad z = \frac{E_{\gamma,2}}{E_{\mathrm{beam}}} \tag{8.3}$$

and $\tilde{s}$ is the scaled CMS energy squared and $\tilde{r}$ is the ratio, given by

$$\tilde{s} = \frac{W^2}{4E^2_{\mathrm{beam}}} = y \cdot z, \quad \tilde{r} = \frac{y}{z}. \tag{8.4}$$

The dependence of $f_{\gamma/e}$ on the scaling variables of the photon energy, z, and its mass squared, Q^2, is completely described by the QED calculation. In the present analysis, we took the approximation formula in the interested region of small scattering angles (*i.e.* small masses of photons) based on the equivalent photon approximation (EPA) formula [56]. And we included

the form factor effect, $f(Q^2)$, in the luminosity function for suppression of the virtual-photon contribution, in which the ρ-meson mass was used as the mass scale. Thus,

$$f_{\gamma/e}(z, Q^2_{\max}) = \frac{\alpha}{\pi}\frac{1}{z}\left[\frac{1}{2}\{1+(1-z)^2\}\int\frac{f(Q^2)}{Q^2}\mathrm{d}Q^2 - (1-z)\right]. \tag{8.5}$$

The uncertainty in the luminosity function, due to the approximation of the EPA formula, was estimated by comparing the present function with those derived from other formulas, and also with that from the exact QED calculation of the two-photon processes [55]. The uncertainty was found to be a few percent at maximum and can be neglected safely.

It should be noted that the ambiguity in the form factor effect of the photon virtuality was not appreciable in the present measurements. We observed only a few percent change in the cross section result when we removed the ρ-meson mass in the form factor for the test. The change in the form factor effected the luminosity function substantially. However, it also changed the efficiency, and the net effects in the cross section were canceled. This is because the p_t-balance cut applied in the event selection tightly restricts the contribution of highly-virtual photons.

8.2 Cross section

The angular dependence of the cross section, $\mathrm{d}\sigma/\mathrm{d}|\cos\theta^*|$, was evaluated by using

$$\frac{\mathrm{d}\sigma}{\mathrm{d}|\cos\theta^*|}(W_{\gamma\gamma}) = \frac{N_{\text{observed}} - N_{\text{background}}}{\eta(W_{\gamma\gamma}, \cos\theta^*)\cdot L_{\gamma\gamma}(W_{\gamma\gamma})\cdot\int\mathcal{L}\mathrm{d}t\cdot\Delta W_{\gamma\gamma}\cdot\Delta|\cos\theta^*|}, \tag{8.6}$$

where N_{observed} and $N_{\text{background}}$ were the numbers of candidate and background events, respectively. η was the detection efficiency which was estimated from a MC simulation, $L_{\gamma\gamma}$ was the two-photon luminosity function and $\int\mathcal{L}\mathrm{d}t$ was the integrated luminosity. The integrated luminosity was determined from a measurement of Bhabha scattering at the barrel region.

The measured differential cross section was summed over the whole angular coverage in order to examine the $W_{\gamma\gamma}$ dependence,

$$\sigma(W_{\gamma\gamma})_{\gamma\gamma\to X} = \Delta|\cos\theta^*|\cdot\sum_{\cos\theta^*}\frac{\mathrm{d}\sigma}{\mathrm{d}|\cos\theta^*|}(W_{\gamma\gamma}). \tag{8.7}$$

8.2.1 $\gamma\gamma \to p\bar{p}$

The cross section for $\gamma\gamma \to p\bar{p}$ as a function of $W_{\gamma\gamma}$ in the range $|\cos\theta^*| < 0.6$, $\sigma(W_{\gamma\gamma})_{|\cos\theta^*|<0.6\ \gamma\gamma\to p\bar{p}}$, is tabulated in Table 8.1 and plotted in Fig. 8.1. The previous measurements [9–11] are also shown in the figure, together with theoretical predictions [12, 17, 63]. Though the present result is somewhat larger than those of the previous measurements by CLEO [11] and ARGUS [10] at low energies, it is in good agreement with the CLEO measurement in the high energy region, $W_{\gamma\gamma} > 2.6$ GeV, with comparable statistics. The preference of the diquark model is obvious from this result, at least in the high energy region.

In addition, a new theoretical prediction by Terazawa [63] which is expected to be valid near threshold, is shown in Fig. 8.1. The prediction reasonably reproduces the high-statistics measurement by CLEO at very low energies. This fact may give us another knowledge on this process.

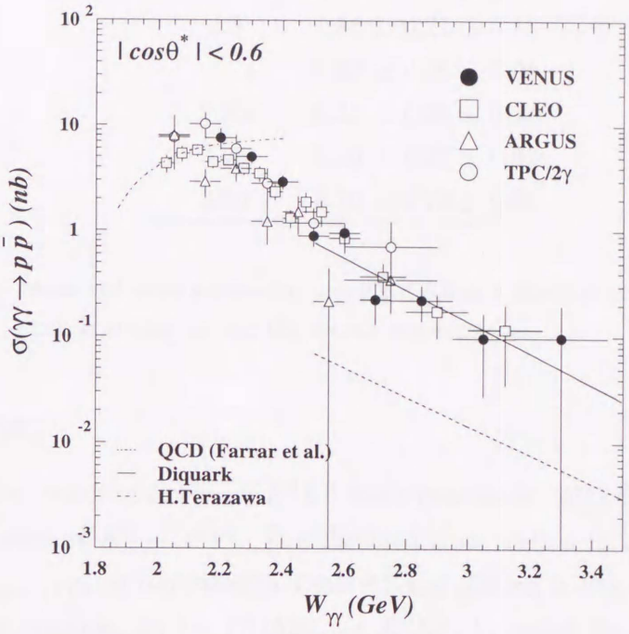

Figure 8.1: Measured cross section for $\gamma\gamma \to p\bar{p}$. The present results (dots with error bars) are plotted together with those from the previous experiments [9–11]. The results from three theoretical calculations drawn by a dashed curve [12], a solid curve [17] and a dashed-dot curve [63] are also shown. The experimental and theoretical results are for the range of $|\cos\theta^*| < 0.6$. The error bars are statistical only.

$W_{\gamma\gamma}$(GeV)	$\sigma(\gamma\gamma \to p\bar{p})$ (nb)
2.2	$7.56 \pm 1.71 \pm 0.70$
2.3	$5.01 \pm 0.65 \pm 0.43$
2.4	$2.90 \pm 0.41 \pm 0.26$
2.5	$0.89 \pm 0.17 \pm 0.12$
2.6	$0.96 \pm 0.21 \pm 0.15$
2.7	$0.23 \pm 0.09 \pm 0.04$
2.85	$0.22 \pm 0.08 \pm 0.04$
3.05	$0.10 \pm 0.07 \pm 0.02$
3.30	$0.10 \pm 0.10 \pm 0.02$

Table 8.1: Measured cross section for $|\cos\theta^*| < 0.6$ as a function of $W_{\gamma\gamma}$. The first error is statistical and the second is systematic.

8.2.2 $\gamma\gamma \to K^0_S K^0_S$

The cross section obtained for $\gamma\gamma \to K^0\bar{K}^0$ was corrected for $K^0_L K^0_L$ production and unseen K^0_S decay modes, such as $K^0_S \to \pi^0\pi^0$. The obtained cross section in the range $|\cos\theta^*| < 0.5$, $\sigma(W_{\gamma\gamma})_{|\cos\theta^*|<0.5\ \gamma\gamma\to K^0\bar{K}^0}$, is tabulated in Table 8.2 and plotted in Fig. 8.2 (a). The theoretical calculation for the reaction, $\gamma\gamma \to f'_2(1525) \to K^0\bar{K}^0$, by using the Breite-Wigner formula is also shown in the figure. This calculation is based on the two-photon decay width value, $\Gamma_{\gamma\gamma}(f'_2) = 0.086$ keV from the world average [18]. In the $f'_2(1525)$ mass region, although the present result seems to be somewhat larger than the previous measurements and the theoretical calculation, it is in reasonable agreement within statistical errors.

To compare the previous measurements in the higher invariant mass region ($W_{\gamma\gamma} > 1.7$ GeV), in which we are interested in this analysis, we plotted the cross section in the logarithmic scale in Fig. 8.2 (b) together with the previous measurements. Since the cross section measured by the TASSO and CELLO groups were used for an angular distribution corresponding to $J = 2$ and helicity 2 in the acceptance calculation, we corrected their cross sections in our angular range, $|\cos\theta^*| < 0.5$, for comparison. It is in good agreement with the previous measurements in this region and no evidence for the new resonance proposed by the L3 group ($X(1800)$) and production of the glueball candidate states $f_J(1710)$ and $f_J(2220)$ is observed.

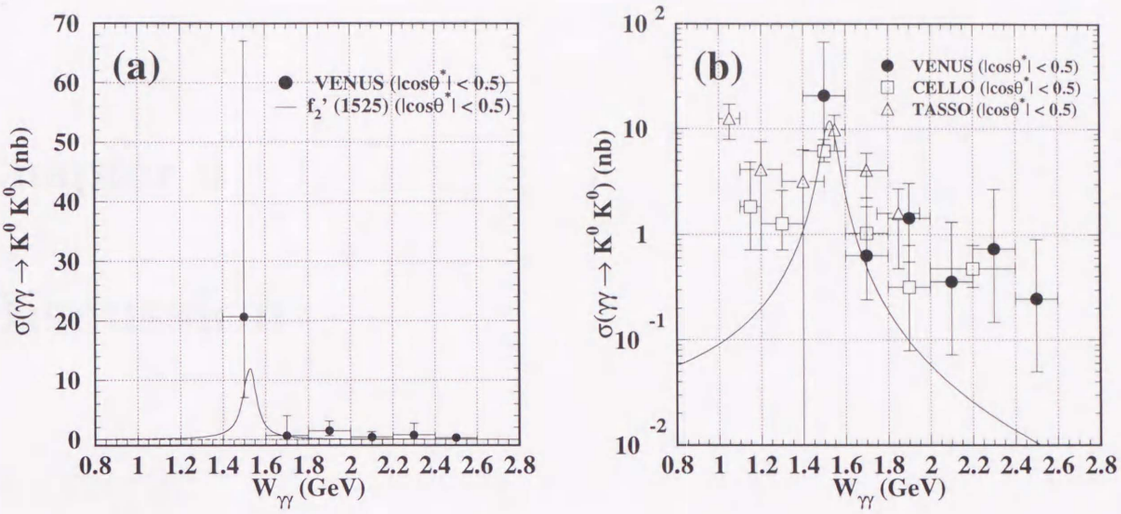

Figure 8.2: The measured cross section for $\gamma\gamma \to K^0\bar{K}^0$: (a) the VENUS result and (b) together with those from the previous experiments [24, 26] in the logarithmic scale. The solid line shows the theoretical expectation for the $f_2'(1525)$ resonance. The error bars are statistical only. In the Fig. (b) the results of the previous experiments are corrected for comparison (see text).

$W_{\gamma\gamma}$(GeV)	$\sigma(\gamma\gamma \to K^0\bar{K}^0)$ (nb)
1.5 ± 0.1	$20.6\ ^{+25.8}_{-7.0} \pm 7.31$
1.7 ± 0.1	$0.63\ ^{+2.76}_{-0.24} \pm 0.22$
1.9 ± 0.1	$1.44\ ^{+0.17}_{-0.55} \pm 0.26$
2.1 ± 0.1	$0.36\ ^{+0.59}_{-0.07} \pm 0.07$
2.3 ± 0.1	$0.73\ ^{+1.22}_{-0.15} \pm 0.11$
2.5 ± 0.1	$0.25\ ^{+0.41}_{-0.05} \pm 0.03$

Table 8.2: Measured cross section for $|\cos\theta^*| < 0.5$ as a function of $W_{\gamma\gamma}$. The first error is statistical and the second is systematic.

Chapter 9

Discussion

9.1 $\gamma\gamma \to p\bar{p}$

In order to proceed further investigation, the differential cross section was summed separately in the low energy region, $2.15 < W_{\gamma\gamma} < 2.55$ GeV, and in the high energy region, $2.55 < W_{\gamma\gamma} < 3.05$ GeV. The obtained differential cross sections are compared in Fig. 9.1. We can see a distinctive difference between the two distributions; the cross section exhibits an enhancement at large angles in the low energy region, whereas it seems to be forward-peaking at high energies. The angular dependence in the high energy region is consistent with the prediction of the diquark model, as has been observed by the CLEO group [11]. However, looking at the result closely, the forward-peaking behavior of the diquark model seems to be insufficient to fully reproduce the measurement. The same tendency can be seen in the CLEO result, as well. This may suggest a need of other theoretical models. In any case, this fact indicates that there is a transition of the production mechanism around $W_{\gamma\gamma} = 2.55$ GeV. The result suggests that a proton pair is mainly produced by the interaction of photons with a diquark in the high $W_{\gamma\gamma}$ region. This description fails to explain the angular distribution at low $W_{\gamma\gamma}$ regions, where a proton seems to be produced as a whole particle having a structure with small orbital angular momenta.

The distinction of the two mechanisms can be enhanced by using the difference in the angular dependence. The differential cross section was summed in a large-angle region, $|\cos\theta^*| < 0.3$, and in a region, $0.3 < |\cos\theta^*| < 0.6$, separately. The obtained cross sections are compared in Fig. 9.2. We can see that the large-angle cross section shows a steep fall-off at high energies, whereas the fall-off of the small-angle cross section is moderate. The difference is distinctive, and the latter overwhelms the former above $W_{\gamma\gamma} = 2.6$ GeV.

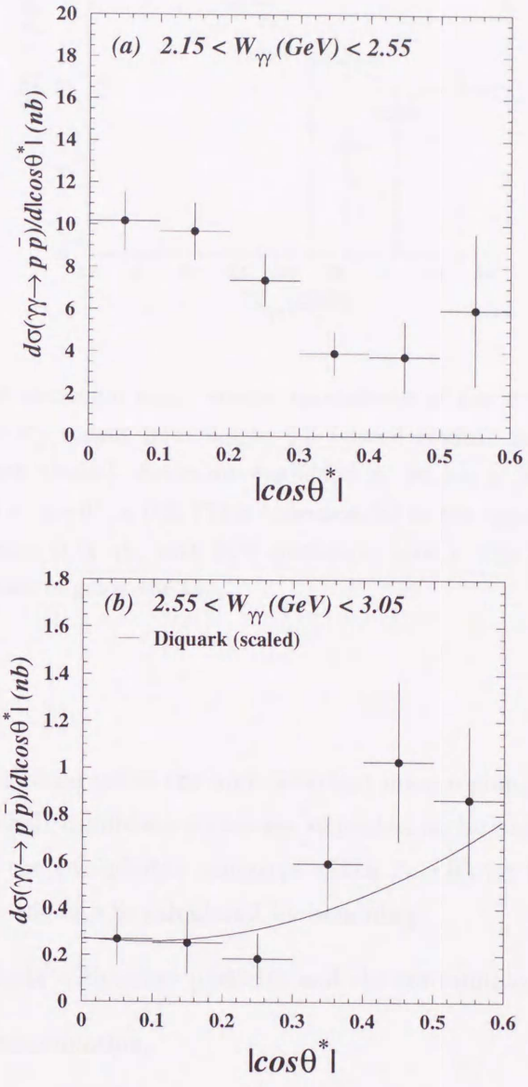

Figure 9.1: Measured differential cross section for $\gamma\gamma \to p\bar{p}$: (a)$2.15 < W_{\gamma\gamma} < 2.55$ GeV and (b)$2.55 < W_{\gamma\gamma} < 3.05$ GeV. In (b), the calculation of a diquark model whose the normalization is scaled to agree with the measurement is also drawn. Errors are statistical only.

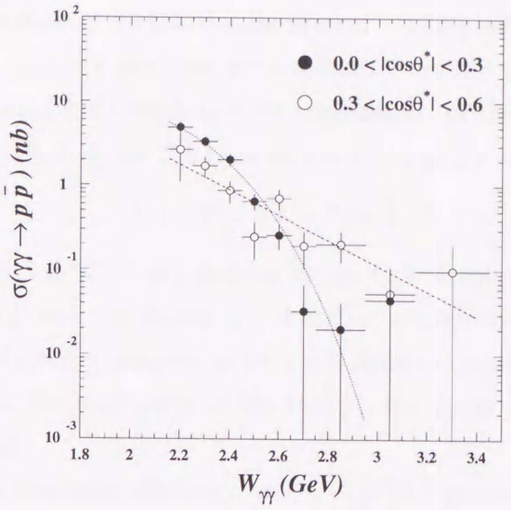

Figure 9.2: The measured c.m. energy dependence of the cross section for the $|\cos\theta^*|$ ranges from 0.0 to 0.3 (closed circles) and from 0.3 to 0.6 (open circles). No event was found in the bin of $W_{\gamma\gamma} = 3.3$ GeV for $0.0 < |\cos\theta^*| < 0.3$. (This corresponded to the upper limit of the cross section 0.14 nb, with 90% confidence level.) The lines are manually drawn to guide the eye.

9.2 $\gamma\gamma \to K^0_S K^0_S$

No excess of events is observed in the high invariant mass region, $W_{\gamma\gamma} > 1.6$ GeV, where the new resonance and glueball candidate states are expected to be observed. We therefore quote here the upper limit of the two-photon radiative width $\Gamma_{\gamma\gamma}(R)$ for the $X(1800)$, $f_J(1710)$ and $f_J(2220)$. The radiative width was calculated by assuming

- no interference effects with other particles and the contamination,
- no background contamination,
- the mass and total decay width of PDG data [60] and
- $J = 2$ and helicity 2.

In principle the amplitudes for both helicity $\lambda = 0$ (T_0) and $\lambda = 2$ (T_2) can contribute to tensor meson resonance production by real photons. The angular distribution of a tensor meson in a helicity λ state decaying to two (pseudo)scalar mesons is $\sim |Y^\lambda_2(\cos\theta)|^2$:

$$\lambda = 2 \qquad |Y^2_2(\cos\theta)|^2 \sim \sin^4\theta \tag{9.1}$$

$$\lambda = 0 \qquad |Y^0_2(\cos\theta)|^2 \sim (\cos^2\theta - 1/3)^2, \tag{9.2}$$

where the decay angle θ is the polar angle of one of the decay particles with respect to the $\gamma\gamma$ direction in the two-photon center-of-mass system. It is predicted that the tensor meson production by two real photons proceeds predominantly via a $\gamma\gamma$ helicity $\lambda = 2$. The $\lambda = 2$ dominance is obtained just from Clebsh-Gordan coefficients. In the case of the lowest multipole for two-photon system, one finds for the ratio of the $\lambda = 0$ and $\lambda = 2$ intensities

$$I(\lambda = 0) : I(\lambda = 2) = 1 : 6. \tag{9.3}$$

The helicity 2 dominance has also been derived in purely hadronic models, *e.g.*, using finite energy sum rules or tensor meson dominance [5]. Since the experimental finding for the amplitude ratio T_0/T_2 are so close to zero [] and since the $\lambda = 2$ dominance is supported by a large variety of theoretical arguments, the evaluation of the two-photon decay width under the assumption of $T_0 = 0$ seems to be safe.

Figure 9.3 shows the detection efficiency for $\gamma\gamma \to K^0_S K^0_S$ assuming the angular distribution for the helicity 2. This was derived from the MC events which were generated assuming a flat angular distribution:

$$\eta_{\lambda=2}(W_{\gamma\gamma}) = \frac{\sum_{\cos\theta^*}(N_{\text{selected}}(W_{\gamma\gamma}, \cos\theta^*) \cdot \sin^4\theta^*)}{\sum_{\cos\theta^*}(N_{\text{generated}}(W_{\gamma\gamma}, \cos\theta^*) \cdot \sin^4\theta^*)}, \tag{9.4}$$

where $N_{\text{generated}}$ is the number of generated MC events for the reaction, $e^+e^- \to e^+e^- K^0_S K^0_S$, using the flat angular distribution and N_{selected} is the number of selected events. Fitting this distribution with a second-order polynomial, the detection efficiency as a function $W_{\gamma\gamma}$ is obtained to be

$$\eta_{\lambda=2}(W_{\gamma\gamma}) = 0.00807 W^2_{\gamma\gamma} - 0.02055 W_{\gamma\gamma} + 0.01304. \tag{9.5}$$

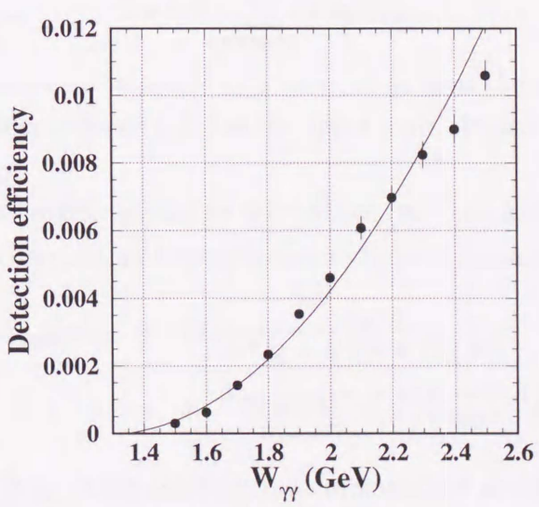

Figure 9.3: The detection efficiency for the $e^+e^- \to e^+e^- K^0_S K^0_S$ assuming the angular distribution for the helicity 2. The curve is the result of a fit using a second-order polynomial.

The upper limit of the two-photon decay width times the branching ratio for $\gamma\gamma \to K\bar{K}$ is calculated by using a Breit-Wigner formula (1.29):

$$\sigma_{\gamma\gamma\to R\to K\bar{K}}(W_{\gamma\gamma})_{\rm upper} = 40\pi \frac{\Gamma_{\rm tot}}{(W^2_{\gamma\gamma} - M^2_R)^2 + \Gamma^2_{\rm tot} M^2_R} \left[\Gamma_{\gamma\gamma}(R) \cdot {\rm Br}(R \to K\bar{K})\right]_{\rm upper}, \quad (9.6)$$

where $J = 2$ is assumed. Since only the reaction of

$$e^+e^- \to e^+e^-\gamma\gamma \to e^+e^- R \to e^+e^- K^0_S K^0_S \to e^+e^-\pi^+\pi^-\pi^+\pi^- \quad (9.7)$$

can be measured from our data, using the relation of the branching ratio from isospin conservation,

$$\begin{aligned} {\rm Br}(R \to K\bar{K}) &= 2 \cdot {\rm Br}(R \to K^0\bar{K}^0) \\ &= 2 \cdot 2 \cdot {\rm Br}(R \to K^0_S K^0_S), \end{aligned} \quad (9.8)$$

we determine the upper limit of the cross section for the reaction $\gamma\gamma \to K\bar{K}$:

$$\begin{aligned} \sigma_{\gamma\gamma\to R\to K\bar{K}}(W_{\gamma\gamma})_{\rm upper} &= \left[\sigma_{\gamma\gamma\to R} \cdot {\rm Br}(R \to K\bar{K})\right]_{\rm upper} \\ &= 4\left[\sigma_{\gamma\gamma\to R} \cdot {\rm Br}(R \to K^0_S K^0_S)\right]_{\rm upper} \\ &= 4 \cdot \frac{N_{\rm observed,upper}(ee \to eeR \to eeK^0_S K^0_S \to ee4\pi^\pm)}{\eta_{\lambda=2}(W_{\gamma\gamma}) \cdot L_{\gamma\gamma}(W_{\gamma\gamma}) \cdot \int \mathcal{L}{\rm d}t \cdot {\rm d}W}, \end{aligned} \quad (9.9)$$

where $N_{\rm observed,upper}$ is the upper limit of the number of observed events for reaction (9.7) in the $W_{\gamma\gamma}$ region near the resonance mass. $\eta_{\lambda=2}(W_{\gamma\gamma})$ includes the factor coming from the branching ration of K^0_S decay $[{\rm Br}(K^0_S \to \pi^+\pi^-)]^2$. We calculate $N_{\rm observed,upper}$ by using the following relation

$$1 - \alpha = \sum_{n=n_0+1}^{\infty} f(n; N_{\rm upper}), \quad (9.10)$$

where $f(n;\mu)$ is a Poisson distribution with a mean of μ, n_0 is the number of observed events and $(1-\alpha)$ is the confidence level (C.L.) of the upper limit. Poisson upper limits are given in Table 9.1.

When the number of expected events for the reaction (9.7) assuming ${\rm Br}(R \to K\bar{K}) \cdot \Gamma_{\gamma\gamma}(R) =$ 1 keV is $N_{\rm expected}$, the cross section corresponding to this condition is given by

$$\sigma_{\gamma\gamma\to K\bar{K}}(W_{\gamma\gamma})_{\rm expected} = 40\pi \frac{\Gamma_{\rm tot}}{(W^2_{\gamma\gamma} - M^2_R)^2 + \Gamma^2_{\rm tot} M^2_R} \quad (9.11)$$

$$= 4 \cdot \frac{N_{\rm expected}(ee \to eeR \to eeK^0_S K^0_S \to ee4\pi^\pm)}{\eta_{\lambda=2}(W_{\gamma\gamma}) \cdot L_{\gamma\gamma}(W_{\gamma\gamma}) \cdot \int \mathcal{L}{\rm d}t \cdot {\rm d}W}. \quad (9.12)$$

Using equations (9.6), (9.9), (9.11) and (9.12), we evaluate the upper limit by

$$\begin{aligned} \left[\Gamma_{\gamma\gamma}(R) \cdot {\rm Br}(R \to K\bar{K})\right]_{\rm upper} &= \frac{N_{\rm observed,upper}}{N_{\rm expected}} \\ &= \frac{N_{\rm observed,upper}(ee \to eeR \to eeK^0_S K^0_S \to ee4\pi^\pm)}{\frac{1}{4} \cdot \int \mathcal{L}{\rm d}t \cdot \int \left[\sigma_{\rm expected} \cdot \eta_{\lambda=2} \cdot L_{\gamma\gamma}\right] {\rm d}W}. \end{aligned} \quad (9.13)$$

n_0	$N_{\rm upper}$	n_0	$N_{\rm upper}$
0	3.00	6	11.84
1	4.74	7	13.15
2	6.30	8	14.44
3	7.75	9	15.71
4	9.15	10	16.96
5	10.51	11	18.21

Table 9.1: Poisson upper limits $N_{\rm upper}$ for n_0 observed events at 95% confidence level ($\alpha = 5$ %).

$X(1800)$

Although an enhancement around 1800 MeV was reported by the L3 group we observed no evidence in this region. Unfortunately, since no detailed information was given about this resonance, we calculate the two-photon radiative width by assuming $M = 1800$ MeV and $\Gamma_{\rm tot} = 50$ MeV. We observed 1 event which corresponds to 35.67 expected events for $\mathrm{Br}(R \to K\bar{K}) \cdot \Gamma_{\gamma\gamma}(R) = 1$ keV in the mass region of $1750 < W_{\gamma\gamma} < 1850$ MeV. The resulting upper limit is:

$$\Gamma_{\gamma\gamma}(X(1800)) \cdot \mathrm{Br}(X(1800) \to K\bar{K}) < 0.13 \text{ keV} \quad (95\% \text{ C.L.}). \tag{9.14}$$

Glueball candidate states

We now discuss the glueball candidate states $f_J(1710)$ and $f_J(2220)$. The $f_J(1710)$ has been observed in radiative J/ψ decays. The most frequent decay mode is $K\bar{K}$. We observe 3 events which corresponds to 28.44 expected events for $\mathrm{Br}(R \to K\bar{K}) \cdot \Gamma_{\gamma\gamma}(R) = 1$ keV in the $f_J(1710)$ mass region ($1522 < W_{\gamma\gamma} < 1872$ MeV). The resulting upper limit is:

$$\Gamma_{\gamma\gamma}(f_J(1710)) \cdot \mathrm{Br}(f_J(1710) \to K\bar{K}) < 0.27 \text{ keV} \quad (95\% \text{ C.L.}) \tag{9.15}$$

where the mass and total decay width used are 1697 MeV and 175 MeV, respectively.

The $f_J(2220)$ state has been seen in the $K\bar{K}$ systems produced in the radiative decay of J/ψ. Although the status of $f_J(2220)$ is not confirmed yet, we quote here the upper limit for the two photon coupling of a possible 2^{++} state with $M = 2225$ MeV and $\Gamma = 38$ MeV. We observe 1 event which corresponds to 53.84 expected events for $\mathrm{Br}(R \to K\bar{K}) \cdot \Gamma_{\gamma\gamma}(R) = 1$ keV in the $f_J(2220)$ mass region ($2187 < W_{\gamma\gamma} < 2263$ MeV). The resulting limit is:

$$\Gamma_{\gamma\gamma}(f_J(2220)) \cdot \mathrm{Br}(f_J(2220) \to K\bar{K}) < 0.088 \text{ keV} \quad (95\% \text{ C.L.}). \tag{9.16}$$

The obtained upper limits are compared with other experimental results as shown in Fig. 9.4. The present upper limit for $f_J(1710)$ seems to be less significant statistically compared with these of CELLO and PLUTO groups, whereas the present result for $f_J(2220)$ is statistically

comparable with those of all the groups. Recently, CLEO reported the result for $f_J(2220)$ from much higher luminosity measurements [64]. The result of $\Gamma_{\gamma\gamma}(f_J(2220)) \cdot \mathrm{Br}(f_J(2220))$ upper limit is 1.4 eV (95 % C.L.) under the assumption that the ratio of the two-photon decay widths for the helicity 0 and helicity 2 is 6:1 and $J = 2$.

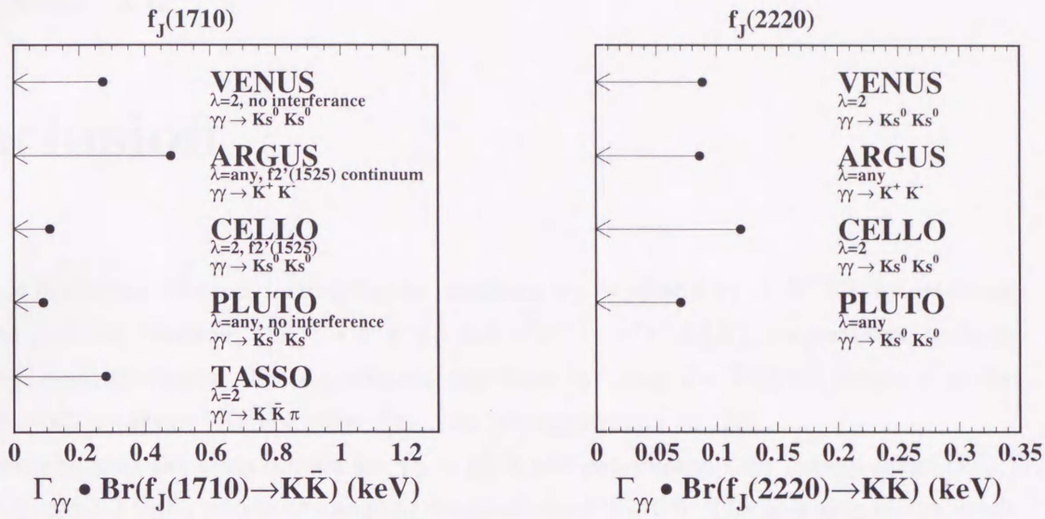

Figure 9.4: Comparison of the upper limit of $\Gamma_{\gamma\gamma} \cdot \mathrm{Br}(R \to K\bar{K})$.

Chapter 10

Conclusion

We have measured the cross section for the reactions, $\gamma\gamma \to p\bar{p}$ and $\gamma\gamma \to K^0\bar{K}^0$, by detecting two-photon collision reaction, $e^+e^- \to e^+e^-p\bar{p}$ and $e^+e^- \to e^+e^-K^0_SK^0_S$, respectively, without tagging the recoil electrons. The experiment was done by using the VENUS detector at the TRISTAN e^+e^- collider of KEK at the e^+e^- c.m. energy around 58 GeV.

We have obtained the cross section for $\gamma\gamma \to p\bar{p}$ in the two-photon c.m. energy range ($W_{\gamma\gamma}$) between 2.2 and 3.3 GeV, within the angular range of $|\cos\theta^*| < 0.6$. The precision of the result is comparable with the high-statistics measurement by CLEO group [11] in the high energy region, $W_{\gamma\gamma} > 2.6$ GeV. The obtained cross section is consistent with those from the previous measurements. The enhancement at small angles in the high energy region, $W_{\gamma\gamma} > 2.6$ GeV, which was shown in the CLEO measurement, has been clearly observed. The preference of the diquark model [17] at high energies has been confirmed by the present results. Although it is not conclusive due to poor statistics, there may be a hint that the predicted enhancement at small angles is not large enough to reproduce the measured results. More data are needed to proceed further discussion.

The cross section for $\gamma\gamma \to K^0\bar{K}^0$ was measured in the $W_{\gamma\gamma}$ range between 1.5 and 2.5 GeV within the angular range of $|\cos\theta^*| < 0.5$. In the high-$W_{\gamma\gamma}$ region (> 1.6 GeV), the obtained cross section is consistent with those from the previous measurements. No enhancement is seen for the resonance around 1800 MeV reported by L3 collaboration [27]. With assumptions on helicity state 2, no interference effects and the total decay width of 50 MeV, we obtained the upper limit $\Gamma_{\gamma\gamma}(X(1800)) \cdot \mathrm{Br}(X(1800) \to K\bar{K}) < 0.13$ keV at 95 % confidence level (C.L.). We also observe no evidence for the production of the glueball candidate states $f_J(1710)$ and $f_J(2220)$ and obtained the upper limits $\Gamma_{\gamma\gamma}(f_J(1710)) \cdot \mathrm{Br}(f_J(1710) \to K\bar{K}) < 0.27$ keV at 95 % C.L. and $\Gamma_{\gamma\gamma}(f_J(2220)) \cdot \mathrm{Br}(f_J(2220) \to K\bar{K}) < 0.088$ keV at 95 % C.L. Although this limit is relatively small compared with the previous measurements, more data are necessary to establish $f_J(1710)$ and $f_J(2220)$ as glueball candidate states.

Bibliography

[1] S. J. Brodsky, T. Kinoshita and H. Terazawa, Phys. Rev. **D4**, (1971) 1532.

[2] J. J. Sakurai and D. Schildknecht, Phys. Lett. **40B**, (1972) 121;
B. Margolis, Phys. Rev. **D17**, (1978) 1310;
I. F. Ginzburg and V. G. Serbo, Phys. Lett. **109B**, (1982) 231.

[3] H. Terazawa, J. Phys. Soc. Jpn. **47**, (1979) 355;
K. Kajanitie and R. Raitio, Nucl. Phys. **B159**, (1979) 528;
M. Dress and R. M. Godbole, Nucl. Phys. **B339**, (1990) 355;
M. Dress, M. Krämer, J. Zunft and P. M. Zerwas, Phys. Lett. **B306**, (1993) 371.

[4] V. M. Budnev, I. F. Ginzburg, G. V. Meledin and V. G. Serbo, Phys. Report **15C**, (1975) 181.

[5] M. Poppe, Intern. J. Mod. Phys. **A3**, (1986) 545.

[6] C. N. Yang, Phys. Rev. **77**, (1950) 242.

[7] TASSO Collab., M. Althoff *et al.*, Phys. Lett. **130B**, (1983) 449.

[8] JADE Collab., W. Bartel *et al.*, Phys. Lett. **174B**, (1986) 350.

[9] TPC/2γ Collab., A. Aihara *et al.*, Phys. Rev. **D36**, (1987) 3506.

[10] ARGUS Collab., H. Albrecht *et al.*, Z. Phys. **C42**, (1989) 543.

[11] CLEO Collab., M. Artuso *et al.*, Phys. Rev. **D50**, (1994) 5484.

[12] R. Farrar *et al.*, Nucl. Phys. **B259**, (1985) 702; **B263**, (1986) 746(E).

[13] D. Millers and J. F. Gunion, Phys. Rev. D **34**, (1986) 2657.

[14] T. Hyer, Phys. Rev. D **47**, (1993) 3875.

[15] G. P. Leparge and S. J. Brodsky, Phys. Rev. D **22**, (1980) 2157.

[16] V. L. Chernyak and I. R. Zhitnitsky, Nucl. Phys. **B246**, (1984) 52.

[17] M.Anselmino *et al.*, Int. J. Mod. Phys. **A4**, (1989) 5213;
P.Kroll *et al.*, Int. J. Mod. Phys. **A6**, (1991) 4107;
P. Kroll *et al.*, Phys. Lett. B **316**, (1993) 546.

[18] R. M. Barnett *et al.*, Phys. Rev. **D54**, (1996) 1.

[19] VENUS Collab., F. Yabuki *et al.*, J. Phys. Soc. Japan. Vol. 64, No2, (1995) 435.

[20] CELLO Collab., H. J. Behrend *et al.*, Z. Phys. **C56**, (1992) 381.

[21] ARGUS Collab., H. Albrecht *et al.*, Z. Phys. **C74**, (1997) 469.

[22] MD-1 Collab., Baru *et al.*, Z. Phys. **C48**, (1990) 581.

[23] H. J. Lipkin, Nucl. Phys. **B7**, (1968) 321;
D. Faiman *et al.*, Phys. Lett. **B59** (1975) 269.

[24] TASSO Collab., M. Althoff *et al.*, Phys. Lett. **121B**, (1983) 216;
TASSO Collab., M. Althoff *et al.*, Z. Phys. **C29**, (1985) 189.

[25] PLUTO Collab., Ch. Berger *et al.*, Z. Phys. **C37**, (1988) 329.

[26] CELLO Collab., H. J. Behrend *et al.*, Z. Phys. **C43**, (1989) 91.

[27] L3 Collab., M. Acciarri *et al.*, Phys. Lett. **B363**, (1995) 118.

[28] TPC/Two-Gamma Collab., H. Aihara *et al.*, Phys. Rev. Lett. **57**, (1986) 404.

[29] ARGUS Collab., H. Albrecht *et al.*, Z. Phys. **C48** (1990) 183.

[30] F. Close, Rep. Prog. Phys. **51**, (1988) 833.

[31] C. Edwards *et al.*, Phys. Rev. Lett. **48**, (1982) 458;
J. E. Augustin *et al.*, Phys. Rev. Lett. **60**, (1988) 2238;
R. M. Baltrusaitis *et al.*, Phys. Rev. **D35**, (1987) 2077.

[32] T. A. Armstrong *et al.*, Phys. Lett. **167B**, (1986) 133;
Phys. Lett. B **227**, (1989) 186; Phys. Lett. **B307**, (1993) 399;
A. Bertin *et al.*, Phys. Lett. **B361**, (1995) 187;
Crystal Barrel Collab., C. Amsler *et al.*, Phys. Lett. **B358**, (1995) 389.

[33] A. Etkin *et al.*, Phys. Rev. **D25**, (1982) 1786;
B. Bolonkin *et al.*, Nucl. Phys. **B309**, (1988) 426.

[34] D. Weingarten, Nucl. Phys. **B34**, (1994) 29.

[35] BES Collab., J. Bai *et al.*, Phys. Rev. Lett. **76**, (1996) 3502;
Kuangta Chao, Commun. Theor. Phys. **24** (1995) 373.

[36] E. H. Kada, P. Kessler and J. Parisi, Phys. Rev. **D39** (1989) 2657.

[37] VENUS Collab., K. Abe *et al.*, J. Phys. Soc. Jpn. **561**, (1987) 3763.

[38] Y. Yamada *et al.*, Nucl. Instr. and Meth. **A330** (1994) 64.

[39] F. Takasaki *et al.*, Nucl. Instr. and Meth. **A322** (1992) 211.

[40] R. Arai *et al.*, Nucl. Instr. and Meth. **A217**, (1983) 181.

[41] M. Sakuda *et al.*, Nucl. Instr. and Meth. **A311**, (1992) 57.

[42] Y. Hemmi *et al.*, Jpn. J. Appl. Phys. **26**, (1987) 982.

[43] M. Wake *et al.*, IEEE Trans. Mag. **21**, (1985) 494.

[44] R. Arai *et al.*, Nucl. Instr. and Meth. **A254**, (1987) 317.

[45] K. Ogawa *et al.*, Jpn. J.Appl. Phys. **23**, (1984) 897;
K. Ogawa *et al.*, Nucl. Instr. and Meth. **A243**, (1986) 58;
T. Sumiyoshi *et al.*, Nucl. Instr. and Meth. **A271**, (1988) 432.

[46] K. Ogawa *et al.*, Nucl. Instr. and Meth. **A238**, (1985) 328.

[47] Y. Fukushima *et al.*, IEEE Trans. Nucl. Sci. **NS-36**, (1989) 670.

[48] Y. Asano *et al.*, Nucl. Instr. and Meth. **A259**, (1987) 430;
Y. Ikegami *et al.*, IEEE. TRANS. **NS.36**, (1989) 183.

[49] T. Ohsugi *et al.*, Nucl. Instr. and Meth. **A269**, (1988) 522.

[50] Y. Arai and S. Uehara, Nucl. Instr. and Meth. **A301**, (1991) 497.

[51] Y. Arai and S. Uehara, Nucl. Instr. and Meth. **A269**, (1988) 522;
K. Amako *et al.*, Nucl. Instr. and Meth. **A272**, (1988) 687.

[52] Y. Nakagawa *et al.*, Jpn. J. Appl. Phys. **25** (1986) 1049;
T. Oyama *et al.*, Nucl. Instr. and Meth. **A305** (1991) 71.

[53] R. L. Fold and W. R. Nelson, SLAC-report-210, UC-32 (1978);
W. R. Nelson, H. Hirayama and D. W. O. Rogers, SLAC-report-265, December 1985.

[54] G. A. Akopdjanov *et al.*, Nucl. Instr. and Meth. **140** (1977) 441.

[55] S. Uehara, KEK Report 96-11 (July 1996), unpublished.

[56] Ch. Berger and W. Wagner, Phys. Rep. **146**, (1987) 1.

[57] H. Krasemann and J. A. M. Vermaseren, Nucl. Phys. **B184**, (1981) 269.

[58] F. A. Berends, P. H. Daverveldt and R. Kleiss, Nucl. Phys. **B253**, (1985) 441;
F. A. Berends, P. H. Daverveldt and R. Kleiss, Comp. Phys. Comm. **40**, (1986) 285.

[59] T. Sjöstrand, Cern-TH.7112/93 (1994).

[60] R. M. Barnett *et al.*, Phys. Rev. **D54**, (1996) 1;
URL: http://pdg.lbl.gov (1997 off-year partial update for the 1998 edition).

[61] P. A. Aarnio *et al.*, Fluka user's guide. Technical Report TIS-RP-190, CERN, 1987, 1990.

[62] S. Odaka, VENUS NOTE 262 (1991);
S. Odaka, VENUS NOTE 285 (1993).

[63] H. Terazawa, Institute for Nuclear Study, University of Tokyo, Report No. INS-Rep.-1122(1995).

[64] CLEO Collab., R. Godang *et al.*, Phys. Rev. Lett. **79**, (1997) 3829.

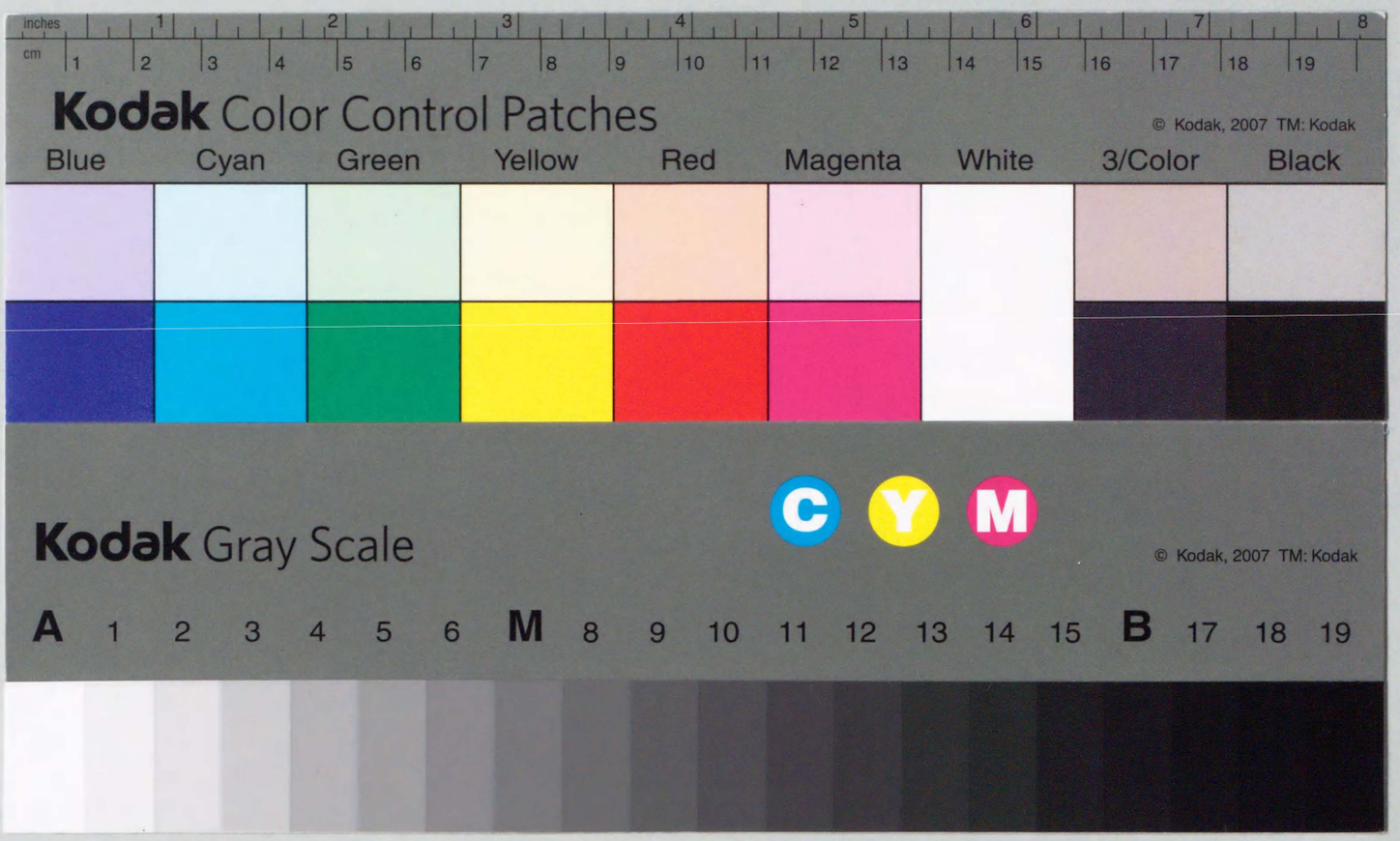
inches
cm
Kodak Color Control Patches
© Kodak, 2007 TM: Kodak
Blue
Cyan
Green
Yellow
Red
Magenta
White
3/Color
Black
Kodak Gray Scale
C
Y
M
© Kodak, 2007 TM: Kodak
A 1 2 3 4 5 6 M 8 9 10 11 12 13 14 15 B 17 18 19